

## Superconducting proximity and confinement in a two-dimensional electron gas

Kulesh, I.

**DOI**

[10.4233/uuid:41f57e3e-4163-4fdc-997f-f4f4b1e8fde1](https://doi.org/10.4233/uuid:41f57e3e-4163-4fdc-997f-f4f4b1e8fde1)

**Publication date**

2025

**Document Version**

Final published version

**Citation (APA)**

Kulesh, I. (2025). *Superconducting proximity and confinement in a two-dimensional electron gas*. [Dissertation (TU Delft), Delft University of Technology]. <https://doi.org/10.4233/uuid:41f57e3e-4163-4fdc-997f-f4f4b1e8fde1>

**Important note**

To cite this publication, please use the final published version (if applicable). Please check the document version above.

**Copyright**

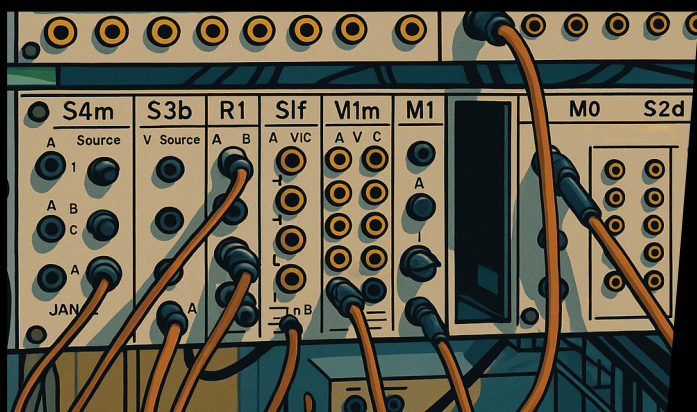
Other than for strictly personal use, it is not permitted to download, forward or distribute the text or part of it, without the consent of the author(s) and/or copyright holder(s), unless the work is under an open content license such as Creative Commons.

**Takedown policy**

Please contact us and provide details if you believe this document breaches copyrights. We will remove access to the work immediately and investigate your claim.



# SUPERCONDUCTING PROXIMITY and confinement in a 2DEG



Ivan Kulesh

**SUPERCONDUCTING PROXIMITY AND  
CONFINEMENT IN A TWO-DIMENSIONAL ELECTRON  
GAS**



# **SUPERCONDUCTING PROXIMITY AND CONFINEMENT IN A TWO-DIMENSIONAL ELECTRON GAS**

## **Dissertation**

for the purpose of obtaining the degree of doctor  
at Delft University of Technology,  
by the authority of the Rector Magnificus, prof. dr. ir. T.H.J.J. van der Hagen,  
chair of the Board for Doctorates,  
to be defended publicly on Thursday, 12 June 2025 at 10:00 o'clock

by

**Ivan Pavlovich KULESH**

Master of Science in Applied Physics  
Delft University of Technology, Netherlands

This dissertation has been approved by the promotor.

Composition of the doctoral committee:

Rector Magnificus,	chairperson
Prof. dr. ir. L.P. Kouwenhoven	Delft University of Technology, promotor
Dr. S. Goswami	Delft University of Technology, copromotor

*Independent members:*

Prof. dr. ir. L.M.K. Vandersypen	Delft University of Technology
Prof. dr. G. Katsaros	Institute of Science and Technology Austria
Dr. ir. M. Veldhorst	Delft University of Technology
Dr. A. Chatterjee	Delft University of Technology
Prof. dr. Y.M. Blanter	Delft University of Technology, reserve member



*Keywords:* Two-dimensional electron gas, Majorana zero modes, Andreev bound states, Kitaev chain, Quantum dots

*Printed by:* Print&Bind

*Front & Back:* SPC Delft, by Alina Kuliesh and Sofiia Biletska.

Copyright © 2025 by I.P. Kulesh

ISBN 978-94-6384-791-9

An electronic version of this dissertation is available at  
<http://repository.tudelft.nl/>.

# CONTENTS

<b>Summary</b>	<b>vii</b>
<b>Samenvatting</b>	<b>ix</b>
<b>1 Introduction</b>	<b>1</b>
<b>2 Theory</b>	<b>5</b>
2.1 Andreev bound states . . . . .	6
2.2 ECT and CAR . . . . .	10
2.3 Poor man's Majorana . . . . .	11
<b>3 Improvements in the fabrication and measurements methods</b>	<b>15</b>
3.1 Optimising gate design for quantum devices . . . . .	16
3.1.1 Double quantum dot interferometer design . . . . .	17
3.2 Bridging contacts using ALD etching . . . . .	19
3.3 Two-step wet Al etching for compact JJs. . . . .	20
3.3.1 Flux-tunable Josephson Effect in a Four-Terminal Junction . . . . .	20
3.4 Resonators for reflectometry measurements . . . . .	22
3.4.1 Optimising resonator parameters . . . . .	22
3.4.2 Rastering measurements with reflectometry . . . . .	23
3.5 Appendix: fab flow for the off-chip resonators . . . . .	25
3.6 Appendix: fab flow for InSbAs chips. . . . .	25
<b>4 Coupling quantum dots via a planar Josephson junction</b>	<b>29</b>
4.1 Introduction . . . . .	30
4.2 ABS spectroscopy . . . . .	31
4.3 ECT, CAR . . . . .	32
4.4 Spin blockade . . . . .	34
4.5 Tuning ECT and CAR amplitude . . . . .	35
4.6 Appendix: Using Quantum dot as a spectroscopy tool . . . . .	36
4.7 Appendix: Extracting ECT and CAR amplitudes . . . . .	37
4.8 Appendix: Additional data for the first generation device . . . . .	37
<b>5 Flux-tunable PMM</b>	<b>39</b>
5.1 Device Design & Characterization. . . . .	41
5.2 Tuning into PMM regime . . . . .	42
5.3 Exploring gate-phase parameter space . . . . .	45
5.4 Conclusions. . . . .	46
5.5 Supplementary . . . . .	46
5.5.1 Device fabrication . . . . .	46
5.5.2 Transport measurements and data processing . . . . .	46

5.5.3	Supplementary figures . . . . .	47
<b>6</b>	<b>Gate and charge sensing of PMM devices</b>	<b>53</b>
6.1	Introduction . . . . .	54
6.2	Gate sensing in semi-isolated system: comparison with conductance . . . . .	55
6.3	Gate sensing without normal leads: effects of parity . . . . .	57
6.4	Controlling the ABS energy with magnetic flux . . . . .	60
6.5	Charge sensing . . . . .	61
6.6	Appendix: Details of the simulations . . . . .	62
<b>7</b>	<b>Conclusions and outlook</b>	<b>65</b>
7.1	Results discussion. . . . .	65
7.2	Further development . . . . .	66
7.2.1	Rethinking fab and materials. . . . .	67
	<b>Bibliography</b>	<b>72</b>
	<b>Acknowledgments</b>	<b>85</b>
	<b>Curriculum Vitae</b>	<b>87</b>
	<b>List of Publications</b>	<b>89</b>

# SUMMARY

Gate-defined quantum dots (QDs) in a two-dimensional electron gas can serve as versatile building blocks in solid-state research. The richness of emergent phenomena in multi-dot systems is closely linked to the available dot-dot interactions. Induced superconductivity can lead to the formation of Andreev bound states (ABS), which, in turn, can mediate superconducting pairing between QDs. This interaction, combined with electron exchange, results in the formation of zero-energy delocalized states in the simplest possible Kitaev chain setup - two quantum dots. These states are predicted to exhibit properties of Majorana zero modes, including non-trivial fusion rules and exchange statistics. Verifying these properties would advance our understanding of hybrid mesoscopic systems, improve theoretical models, and refine experimental techniques. However, before such advanced experiments can be performed, we need to reliably create, tune, and characterize the simplest artificial Kitaev chains.

In this thesis, we focus on experiments involving two quantum dots coupled via an Andreev bound state, and we explore the quantum states arising in this system. The devices are fabricated on a two-dimensional electron gas using electron-beam lithography, wet and dry etching methods, and conventional thin-film deposition techniques. Due to the complexity of the device layout, a multi-layer approach is employed. To gain additional insight into device properties and to pave the way for fast, parity-preserving measurements, we employ radio-frequency (RF) measurement techniques alongside conventional DC conductance characterization.

In the first experiment presented in this thesis, we focus exclusively on tuning the interactions between two quantum dots, without considering the combined quantum state of the system. We demonstrate that it is possible to mediate and control Cooper pair splitting and elastic co-tunneling using a planar Josephson junction as a mediator.

Expanding on this idea, we adjust the geometry of the junction and demonstrate tunable coupling between quantum dots separated by  $1\mu\text{m}$ . We show that the system can be tuned to a poor man's Majorana sweet spot with both gate voltage and magnetic flux, which we confirm using DC and RF spectroscopic measurements.

In the final experiment, we study how a similar system behaves when isolated from the normal leads. To track the device state in the absence of tunnel probes, we use a less invasive, parity-preserving method of RF gate reflectometry. Interactions between the dots, as well as between the dots and Andreev bound states (ABS), are clearly resolved. Moreover, we show that this method is sensitive to the device parity, although it cannot yet be used to resolve it due to low sensitivity and a fast poisoning rate.

This thesis concludes with a discussion of the results. I also touch upon potential future experiments that expand on the developed designs and methods, as well as possible fabrication and material improvements.



# SAMENVATTING

Gate-gedefinieerde kwantumdots (QD's) in een tweedimensionaal elektrongas kunnen dienen als veelzijdige bouwstenen in het vastestoffysica onderzoek. De rijkdom aan opkomende verschijnselen in multi-dot systemen is nauw verbonden met de beschikbare interacties tussen de dots. Geïnduceerde supergeleiding kan leiden tot de vorming van Andreev gebonden toestanden (ABS), die op hun beurt supergeleidende paarvorming tussen QD's kunnen bemiddelen. Deze interactie, gecombineerd met elektronische uitwisseling, resulteert in de vorming van nul-energie gedegeerd toe-standen in de eenvoudigst mogelijke Kitaev-ketenopstelling: twee kwantumdots. Er wordt voorspeld dat deze toestanden eigenschappen vertonen van Majorana nul-modi, inclusief niet-triviale fusie regels en uitwisselingsstatistieken. Het verifiëren van deze eigenschappen zou ons begrip van hybride mesoscopische systemen bevorderen, theoretische modellen verbeteren en experimentele technieken verfijnen. Echter, voordat dergelijke geavanceerde experimenten kunnen worden uitgevoerd, moeten we op betrouwbare wijze de eenvoudigste kunstmatige Kitaev-ketens creëren, afstemmen en karakteriseren.

In dit proefschrift richten we ons op experimenten met twee kwantumdots gekoppeld via een Andreev gebonden toestand, en verkennen we de kwantumtoestanden die in dit systeem ontstaan. De apparaten worden vervaardigd op een tweedimensionaal elektrongas met behulp van elektronenbundel-lithografie, natte en droge etsmethoden en conventionele dunne-film deposities. Vanwege de complexiteit van het apparaatschema wordt een multi-laagbenadering toegepast. Om meer inzicht te krijgen in de apparaat-eigenschappen en de weg vrij te maken voor snelle, pariteit-behoudende metingen, maken we gebruik van radiofrequentie (RF) meettechnieken naast conventionele DC-geleidingskarakterisering.

In het eerste experiment dat in dit proefschrift wordt gepresenteerd, richten we ons uitsluitend op het afstemmen van de interacties tussen twee kwantumdots, zonder de gecombineerde kwantumtoestand van het systeem te beschouwen. We demonstreren dat het mogelijk is om Cooper-paar splitting en elastisch co-tunnelen te bemiddelen en te controleren met behulp van een platte Josephson-junctie als bemiddelaar.

Door dit idee uit te breiden, passen we de geometrie van de junctie aan en demonstreren we afstelbare koppeling tussen kwantumdots die gescheiden zijn door  $1\ \mu\text{m}$ . We laten zien dat het systeem kan worden afgestemd op een arme-man's Majorana sweet spot met zowel poortspanning als magnetische flux, wat we bevestigen met DC- en RF-spectroscopiemetingen.

In het laatste experiment bestuderen we hoe een vergelijkbaar systeem zich gedraagt wanneer het is geïsoleerd van de normale leads. Om de apparaattoestand bij afwezigheid van tunnelprobes te volgen, maken we gebruik van een minder invasieve, pariteit-behoudende methode van RF-poortreflectometrie. Interacties tussen de dots, evenals tussen de dots en Andreev gebonden toestanden (ABS), worden duidelijk opgelost. Bovendien tonen we aan dat deze methode gevoelig is voor de apparaatpariteit, hoewel

het nog niet mogelijk is om deze op te lossen vanwege de lage gevoeligheid en de snelle vergiftigingsgraad.

Dit proefschrift wordt afgesloten met een bespreking van de resultaten. Ik behandel ook mogelijke toekomstige experimenten die voortbouwen op de ontwikkelde ontwerpen en methoden, evenals mogelijke verbeteringen in fabricage en materiaal.

# 1

## INTRODUCTION

*In any work there is room for creativity*

Sergei Dovlatov

Recent advancements in chemistry, materials science, engineering, and nanofabrication have enabled an unprecedented level of control over material parameters. The ability to manufacture pure crystalline semiconductors with controlled heterogeneous composition has allowed us to exploit the physical laws governing the behavior of solid-state systems. We can create structures exhibiting properties of reduced dimensions, such as two-dimensional electron gases, one-dimensional nanowires and carbon nanotubes, as well as zero-dimensional quantum dots. Moreover, it is possible to combine the properties of different materials, such as creating superconducting correlations in a semiconducting material.

At the same time, the art of isolating quantum systems from the environment, such as the invention and spread of dilution refrigerators for the solid-state applications, made it possible to coherently manipulate quantum states. In particular, one can achieve a high degree of control over quantum dots (QD), which can behave as artificial atoms. It is truly remarkable that such complex objects, consisting of multiple compounds and countless atoms, can be effectively described by a Hamiltonian with only a few terms. QDs in solid-state systems have recently received a great deal of attention in the context of quantum information processing[1].

We can, however, view these objects from a different perspective. By assembling multiple quantum dots and enabling them to interact, we can create an effective 1D or 2D "material" made of artificial atoms[2, 3, 4]. Depending on the available on-site terms and interactions, the resulting properties can vary greatly and may be controllable. We can take inspiration from superconducting circuits, which have been successfully used to create useful nonlinear metamaterials, such as Josephson amplifiers[5].

One of the artificial compounds interesting to modern condensed matter physics is the  $p$ -wave, also called a topological superconductor. In low dimensions (1D and 2D), it is predicted to host Majorana quasiparticles with unique physical properties, including nontrivial exchange statistics[6]. Initially proposed as a one-dimensional chain[7], the possibility of creating it in a bulk heterostructure was subsequently introduced[8, 9]. Despite significant experimental efforts, the approach turned out to be futile. Perhaps we have not yet reached the required levels of material purity[10]. However, an alternative approach exists: creating a Kitaev chain using an array of quantum dots with superconducting pairing terms between them[11]. In a way, we have come full circle back to the original proposal. Moreover, even a Kitaev chain of two quantum dots, also known as a Poor Man's Majorana (PMM), exhibits non-trivial properties[12]. Creating a system with controlled superconducting pairing between QDs can also lead to new developments, such as fermionic simulations[13], hybrid qubits[14], spin-qubit gates[15], and other applications of new Hamiltonian terms.

Although there's no advantage in simulating a two-site Hamiltonian using real quantum dots, the simple system can be used as a performance benchmark, since the desired behavior is well known. We can then expand on it to construct a more complex system. Of course, the model used is only a crude approximation, and one of the research questions that needs to be addressed is how accurate this approximation is and which aspects of the real system are detrimental and break the simple model. This, in turn, promotes further development of theoretical models to incorporate additional terms and adjust predictions. In this way, experiment and theory progress hand in hand, with advancements in one field driving developments in the other. Over time, the approach of using PMMs may indeed be seen as naive, given the inherent effects of real systems that are often overlooked in simplified models. However, it is this very uncertainty that makes the research both challenging and deeply rewarding.

The research presented in this thesis explores the control of superconducting pairing between two QDs and the potential of creating and controlling a two-site Kitaev chain. We begin with Chapter 2, which outlines the basic theory used to describe quantum dots (QDs) and their interaction mediated by an Andreev bound state in the proximitized superconducting region. We will describe the electron transfer processes occurring between a pair of QDs - elastic co-tunneling and crossed Andreev reflection. We then discuss how the system behaves as the interaction increases and superconducting correlations in the quantum dots must also be considered. Chapter 3 provides details about the fabrication process, including newly developed designs and methods. In this chapter, we also present several experiments that were not the primary focus of the main thesis topic and, therefore, have not been accounted for in separate chapters. Nevertheless, these experiments were an integral part of the research and clearly demonstrate the measurement and fabrication techniques, such as radio-frequency gate reflectometry and multilayer gate design, used elsewhere in the thesis. Chapters 4 and 5 explore the possibility of using phase-tunable Andreev bound states to mediate inter-dot interactions. We first examine a weak coupling regime and characterize the interaction strength through electrical current measurements, while the subsequent chapter focuses on the strong interaction regime and spectroscopic measurements. Another important difference between these two experiments is the device design, which has a significant impact

---

on the degree of control. In Chapter 6, we turn to exploring less invasive methods for probing the PMM device state. Using RF gate reflectometry, we observe the effects of system parity switching. We conclude the thesis with the [outlook](#), which includes suggestions for future experiments and fabrication improvements.

All analysis code used to generate the figures is available, along with the raw experimental data, in the [4TU.ResearchData](#) repository[16].



# 2

## THEORY

*Theory will take you only so far.*

J. Robert Oppenheimer

*In this chapter, we present some theoretical models of the systems implemented experimentally in the following chapters. We start with the elementary building blocks, such as Andreev bound states and quantum dots, and then show how they can be combined into a two-site artificial Kitaev chain.*

To obtain theoretical models, we will use a series of approximations. It is important to keep track of them, as the underlying details can be crucial for specific aspects of the system under consideration.

Working with semiconducting materials, we are going to sweep under the rug all the complexity of the band structure, the potential of the crystal lattice, and work with effective "electrons", obeying the Schrödinger equation of a free particle with the modified effective mass, effective Landé  $g$ -factor and a Rashba spin-orbit interaction[17, 18]. Furthermore, by confining electrons in a heterostructure, we will factor out motion in the  $z$ -direction (out-of-plane), thus:

$$H\Psi = E\Psi, \quad H = -\frac{\hbar^2}{2m^*}\Delta_{x,y} + U(x,y) + \frac{1}{2}g\mu_B\boldsymbol{\sigma} \cdot \mathbf{B} + \alpha(\sigma_x k_y - \sigma_y k_x) \quad (2.1)$$

In the following step, we abandon the description of the system using propagating particles altogether and focus on the confined states, describing quantum dots (QD)[19, 20] and Andreev bound states. As such, it will be enough to consider electron creation and annihilation operators  $\hat{c}_\sigma^\dagger, \hat{c}_\sigma$  for the specific quantum levels.

The details we have omitted can become important in many practical aspects. Specifics of the semiconducting heterostructure affect the effective Hamiltonian parameters, and the atomic composition can have detrimental effects on the spin decoherence. One must also consider that the confinement in the  $z$ -direction affects the electron mobility (hence the mean free path), and the details of electron motion in all directions are relevant in the context of induced superconductivity[21, 22, 23]. Finally, when focusing on the bound states, the exact wavefunction configuration is relevant, among other aspects, for the tunneling amplitudes.

## 2.1. ANDREEV BOUND STATES

To start our discussion on Andreev bound states, we consider a superconducting Anderson impurity model – a QD coupled to a superconducting lead[24, 25], as schematically represented in Fig. 2.1. The system's Hamiltonian consists of three parts - the one describing the QD, the superconductor, and finally, the interaction term. We will use zero-bandwidth approximation, such that the entire superconductor is represented by a single particle at the gap edge:

$$H = H_{QD} + H_S + H_T, \quad H_S = \Delta d_\downarrow^\dagger d_\downarrow^\dagger + \text{h.c.}, \quad H_T = \sum_\sigma t d_\sigma^\dagger c_\sigma \quad (2.2)$$

To write down the  $H_{QD}$  Hamiltonian, we will consider the total energy of the dot[20] with  $N$  electrons as a reference point and focus on filling the next available orbital:

$$E(N) = \frac{U}{2}(N - n_g)^2 + \sum_{n=1}^N \xi_n(B) \equiv E_0, \quad (2.3)$$

$$E(N+1) = E_0 + U\left(\frac{1}{2} + [N - n_g]\right) + \xi_\downarrow, \quad (2.4)$$

$$E(N+2) = E_0 + U(2 + 2[N - n_g]) + \xi_\downarrow + \xi_\uparrow, \quad (2.5)$$

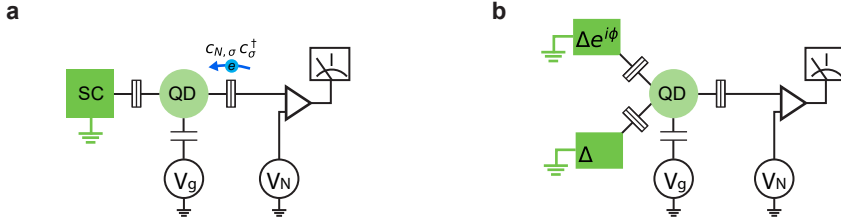


Figure 2.1: Schematic representation of a quantum dot, connected to either a single (a) or a pair (b) of superconducting electrodes. The chemical potential on the QD can be tuned with the gate  $V_g$ . The normal lead is biased with the voltage  $V_N$ , and under certain conditions to be discussed in this chapter, a current can flow.

where  $n_g$  is a so-called "gate-charge" induced by the voltages on all the capacitors connected to the quantum dot, and  $\xi$  contains Zeeman  $E_Z$  and orbital  $\epsilon$  energy. Finally, we shift the energy reference and define  $\mu(V_g) = U(\frac{1}{2} + N - n_g) + \epsilon$ , such that the QD Hamiltonian is

$$H_{QD} = n_\downarrow (\mu - E_Z) + n_\uparrow (\mu + E_Z) + U n_\downarrow n_\uparrow, \quad n_\sigma = c_\sigma^\dagger c_\sigma \quad (2.6)$$

The problem defined by eqs. 2.2,2.6 can be solved using numerical diagonalization considering  $2^4 = 16$  dimensional Fock space. We will return to that shortly, but for now, we will make another approximation to obtain a better understanding of the ABS ground state and excitations. The atomic model assumes  $\Delta \rightarrow \text{inf}$ , under which superconducting pairing term appears in the quantum dot Hamiltonian:

$$H_A = H_{QD} + \Gamma_S c_\downarrow^\dagger c_\uparrow^\dagger + \text{h.c.}, \quad (2.7)$$

where  $\Gamma_S$  represents effective superconducting pairing.

This model can be easily solved, obtaining four energy eigenstates, two of each are even parity singlets  $|S_\pm\rangle = u|0\rangle \pm v|\downarrow\uparrow\rangle$ , and two are odd parity doublets  $|\sigma\rangle$ :

$$E_\downarrow = \mu - E_Z, \quad E_\uparrow = \mu + E_Z, \quad E_{S_\pm} = \tilde{\mu} \pm \sqrt{\tilde{\mu}^2 + \Gamma_S^2}, \quad \tilde{\mu} = \mu + \frac{U}{2} \quad (2.8)$$

while the BCS coherence factors are defined as:

$$u^2, v^2 = \frac{1}{2} \left( 1 \pm \tilde{\mu} / \sqrt{\tilde{\mu}^2 + \Gamma_S^2} \right) \quad (2.9)$$

We can now introduce Bogolyubov creation and annihilation operators (CAPs). We limit ourselves to the case of small charging and Zeeman energy, such that the ground state is always a singlet:  $|GS\rangle = |S_-\rangle$ . New operator  $\gamma$  will define transitions to the excited states:  $\gamma_\sigma^\dagger |GS\rangle = |\sigma\rangle$ . Moreover, the ground state is a vacuum of those Bogolyubov quasiparticles:  $\gamma_\sigma |GS\rangle = 0$ . We can express  $\gamma$  in terms of electron CAPs and vice-versa:

$$\gamma_\downarrow^\dagger = u c_\downarrow^\dagger + v c_\uparrow, \quad \gamma_\uparrow^\dagger = u c_\uparrow^\dagger - v c_\downarrow, \quad \gamma_\downarrow = u c_\downarrow + v c_\uparrow^\dagger, \quad \gamma_\uparrow = u c_\uparrow - v c_\downarrow^\dagger \quad (2.10)$$

$$c_\downarrow^\dagger = u \gamma_\downarrow^\dagger - v \gamma_\uparrow, \quad c_\uparrow^\dagger = u \gamma_\uparrow^\dagger + v \gamma_\downarrow, \quad c_\downarrow = u \gamma_\downarrow - v \gamma_\uparrow^\dagger, \quad c_\uparrow = u \gamma_\uparrow + v \gamma_\downarrow^\dagger \quad (2.11)$$

When deriving relations above, one has to keep track of signs arising due to the fermionic anti-commutation relationship. The operator decomposition is useful when considering electron transport between the ABS and a normal lead or another quantum dot. As an example, a normal lead can either absorb an electron, described by the term  $c_{N,\sigma}^\dagger c_\sigma$ , or emit an electron  $c_{N,\sigma} c_\sigma^\dagger$ .

We can now consider the transport between a normal lead and an ABS. For that purpose, it is convenient to use the semiconducting picture[24, 26, 27], in which we artificially double the degrees of freedom by introducing the negative energy excitations. We will omit here the derivations of the particle-hole symmetric Hamiltonian and refer to[26, 27]. The negative energy excitations are filled in the ground state, while the positive ones are empty.

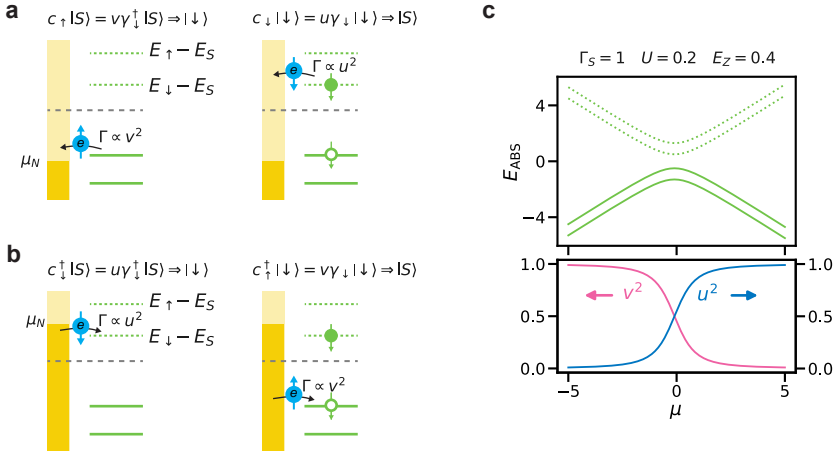


Figure 2.2: Transport between an ABS and a normal lead. For positive bias (a), two electrons per transport cycle flow into the lead, first exciting the ABS and then relaxing it. For the negative bias (b), the direction of the current is inverted. In (c), we plot ABS energy dependence, as well as the coherence factor magnitudes as a function of the ABS chemical potential.

First, we consider the case of a positive bias in the normal lead, Fig. 2.2(a), corresponding to the negative chemical potential  $\mu_N < 0$ . We introduce a small Zeeman term in order to highlight the spin degree of freedom. Once the chemical potential aligns with the filled negative energy ABS, a spin-up electron can be transferred to the lead (or, equivalently, a spin-down hole is transferred to the ABS). The ABS is now in the excited state with higher energy, but the electron entering the lead at negative chemical potential allows to fulfill the energy conservation condition:  $(E_\uparrow - E_S) + \mu_N < 0$ . The rate of this process is proportional to the probability  $v^2$  of finding an electron pair in the singlet[28]. To complete the transport cycle, the ABS has to relax to the singlet ground state. In principle, this can be done by either emitting an electron or a hole (absorbing an electron). The latter is not possible, however, as absorbing an electron would require a net energy gain:  $(E_S - E_\downarrow) - \mu_N > 0$ . Another way of looking into this is that in the semiconducting picture, the ABS cannot emit a hole at negative energy as hole states in the lead are occu-

pied down to  $\mu_N$ . We note here that if the second lead is available, such as for non-local spectroscopy discussed in Ch. 4, it can absorb a hole, resulting in non-local transport. Here, however, the only possibility is emitting an electron, which happens with the rate proportional to  $u^2$ . Overall, we have transferred two electrons into the normal lead, corresponding to one Cooper pair, with a total rate proportional to the product  $u^2 v^2$ .

The case of the negative bias can be considered in the same way, Fig. 2.2(b). Interestingly, the overall rate once again scales as  $u^2 v^2$ . More elaborate configurations, including using quantum dots as spectroscopy probes, can be understood in the same framework.

Now we proceed with expanding the ABS model. Using the same atomic limit, it is straightforward to expand it to accommodate for the two superconducting leads with a phase difference of  $\phi$  between them [29, 30]. For that we will replace  $\Gamma_S$  in eq. 2.7 with  $\Gamma_1 + \Gamma_2 e^{i\phi}$ . Solving this model, we observe typical for a Josephson junction  $2\pi$ -periodic modulation of energy with phase, see Fig. 2.3. Moreover, the BCS coherence factors  $u$  and  $v$  also show a strong phase modulation, which is particularly important when considering non-local transport processes.

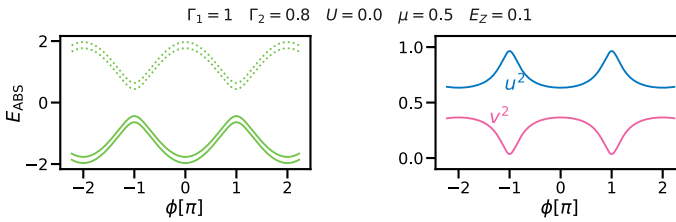


Figure 2.3: Energy spectrum and coherence factors as a function of phase difference  $\phi$  between two superconductors, solved for the proximitized quantum dot in the atomic limit.

Model simplification by assuming an infinitely large superconducting gap comes at a price. One of the shortcomings is the unphysical growth of the ABS energy at a large amplitude of chemical potential, which can be seen in Fig. 2.2(c). In a realistic scenario, one should always be able to excite a system as soon as the energy is above the gap  $\Delta$ .

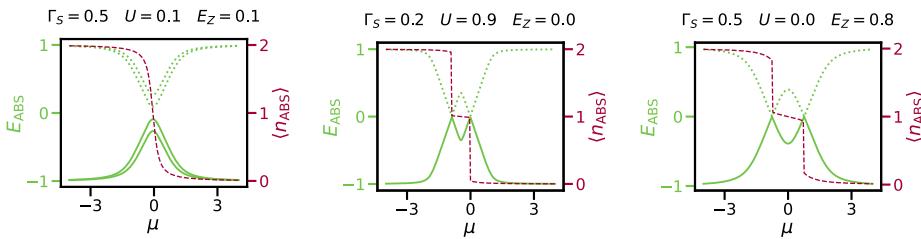


Figure 2.4: Energy spectrum for the zero-bandwidth, finite  $\Delta$  model, computed for several parameter values. Increasing charging energy  $U$  or Zeeman term  $E_Z$  leads to the singlet  $|\downarrow\rangle$  being a possible ground state.

Relaxing the atomic limit condition while still being in the framework of the zero-bandwidth approximation, we go back to the Hamiltonian eq. 2.2 and compute the spec-

trum varying model parameters, Fig. 2.4. Notably, we have restored energy limitation. We also demonstrate two ways in which the system can have a singlet ground state - by either increasing the charging energy or by increasing the Zeeman field. Though the ABS ground state transition is not extensively discussed in this thesis, we will encounter such behavior in the charge sensing experiment in Ch. 6.

## 2.2. ECT AND CAR

We now focus on the second-order electron transport processes, which can be mediated by an Andreev bound state. We utilize a recently developed theoretical framework[31] to describe elastic co-tunneling (ECT) and crossed Andreev reflection (CAR) between two quantum dots. Here, for simplicity, we assume no Zeeman splitting and no spin-orbit interaction, which can be included in a similar manner[31, 32].

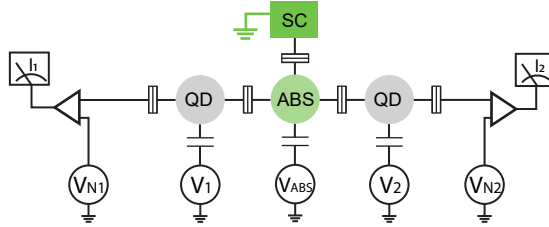


Figure 2.5: Schematic of a non-local transport experiment, measuring elastic co-tunneling and crossed Andreev reflection between a pair of quantum dots, coupled via an Andreev bound state.

Considering initial  $|i\rangle$ , final  $|f\rangle$ , and intermediate  $|m\rangle$  states, the relevant rate under the perturbation  $V$  can be found using the Fermi's Golden rule:

$$W = \frac{2\pi}{\hbar} \left| \sum_m \frac{\langle f|V|m\rangle \langle m|V|i\rangle}{E_i - E_m} \right|^2 \delta(E_i - E_f), \quad V = \sum_{\sigma,i} d_{\sigma,i}^\dagger c_\sigma + c_\sigma^\dagger d_{\sigma,i}, \quad (2.12)$$

where we have included in the perturbation all possible single electron transport processes, with  $d_{\sigma,i}^\dagger$  being the creation operator for the electron on the dot  $i$  with spin  $\sigma$ .

Let us first consider the ECT process, Fig. 2.6(a). As the energy of the initial and final states have to be the same and the ABS is restored to the ground state, the dot energy levels have to be aligned. There are two potential intermediate states: the ABS can either first donate an electron to the second dot while being excited  $d_{1,2}^\dagger c_1 = -v d_{1,2}^\dagger \gamma_1^\dagger$ ; or the ABS accepts an electron from the first dot  $c_1^\dagger d_{1,1} = u \gamma_1^\dagger d_{1,1}$ . Interestingly, the two paths interfere destructively (to keep track of signs one has to consider fermionic anti-commutation relationships). The CAR process can be considered in a similar fashion, Fig. 2.6(b), with the dot energy levels anti-aligned due to the energy conservation constraint. The resulting process rates depend on the BCS coherence factors and the ABS energy  $E_{\text{ABS}} = E_\sigma - E_S$  as:

$$W_{\text{ECT}} = \frac{2\pi}{\hbar} \left| \frac{u^2 - v^2}{E_{\text{ABS}}} \right|^2, \quad W_{\text{CAR}} = \frac{2\pi}{\hbar} \left| \frac{2uv}{E_{\text{ABS}}} \right|^2 \quad (2.13)$$

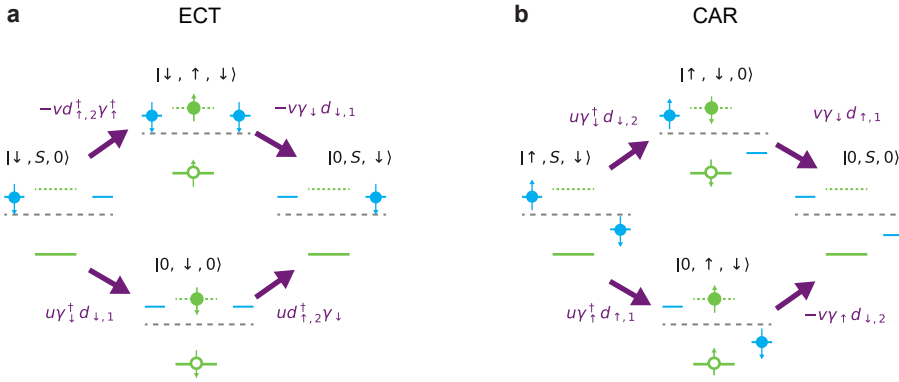


Figure 2.6: Second-order transport cycles for the ECT and CAR processes, considering two potential intermediate states. Arrows indicate matrix elements of the perturbation.

In the previous section, we have seen that the ABS parameters can be controlled with either chemical potential or phase difference in the case of the two superconducting contacts. As such, we can obtain control over the ECT and CAR magnitude, varying experimentally accessible parameters. Using the atomic limit of the ABS, we plot the resulting magnitudes in Fig. 2.7. ECT reaches a minimum at zero chemical potential when  $u = v$  and a maximum at  $\pi$  phase difference. For the CAR, the behavior is inverted. In general, the CAR is maximized when the singlet ground state is the mixture of  $|0\rangle$  and  $|\downarrow\uparrow\rangle$ , corresponding to the strong superconducting correlations. ECT is maximized when the ground state is quantum dot-like – either fully occupied or fully empty.

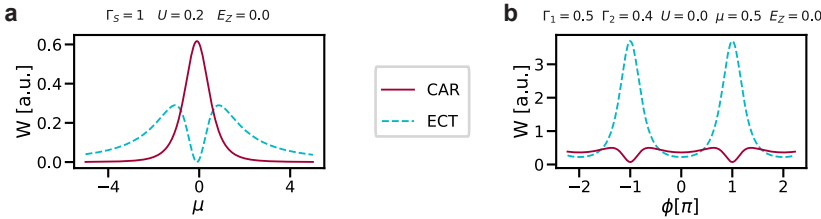


Figure 2.7: ECT and CAR magnitudes as a function of the ABS chemical potential  $\mu$  and the phase difference  $\phi$ .

### 2.3. POOR MAN'S MAJORANA

The effective ECT and CAR interactions between quantum dots can be used to implement an artificial Kitaev chain, hosting Majorana quasiparticles at both ends[7, 11, 12]. Crucially, it requires one to tune the relative strengths of the interactions, and as we have seen, it should be possible by varying the ABS parameters.

The description of the ECT and CAR as second-order tunneling processes, presented above, is useful for understanding the underlying dependencies on the ABS parame-

ters. However, if we want to explore quantum states delocalized between two quantum dots, the effective interaction has to be increased. The consequence is that we should no longer consider the ABS and the quantum dots as isolated systems but instead study the hybridization between all elements. To represent two quantum dots we will use already defined in eq. 2.6 Hamiltonian  $H_{QD}$ , and for the ABS, we assume zero-bandwidth atomic-limit model with zero charging energy and a reduced Zeeman term, being a reasonable approximation considering strong proximity to a superconducting lead. Denoting QD fermionic CAPs with  $d_{\sigma,i}$  and ABS with  $c_{\sigma}$ , the effective Hamiltonian takes the form[33, 34]:

$$H_{PM} = H_{QD,1} + H_{QD,2} + H_{ABS} + \sum_{i,\sigma} t_i (d_{\sigma,i}^{\dagger} c_{\sigma} + \text{h.c.}) + \sum_{i,\sigma} t_{SO,i} (d_{\sigma,i}^{\dagger} c_{\bar{\sigma}} + \text{h.c.}), \quad (2.14)$$

$$H_{QD,i} = n_{\downarrow,i} (\mu_i - E_Z) + n_{\uparrow,i} (\mu_i + E_Z) + U n_{\downarrow,i} n_{\uparrow,i}, \quad n_{\sigma,i} = d_{\sigma,i}^{\dagger} c_{\sigma,i} \quad (2.15)$$

$$H_{ABS} = n_{\downarrow,s} (\mu_s - E_{Z,s}) + n_{\uparrow,s} (\mu_s + E_{Z,s}) + \Delta c_{\downarrow}^{\dagger} c_{\uparrow}^{\dagger} + \text{h.c.}, \quad n_{\sigma,s} = c_{\sigma}^{\dagger} c_{\sigma} \quad (2.16)$$

where we have included spin-flipping coupling terms, accounting for the spin-orbit interaction.

First, we focus on a single QD interacting with the ABS. This resembles the description of *an ABS* in the zero-bandwidth, finite  $\Delta$  model, see Fig. 2.8(c) for the energy spectrum as a function of the QD chemical potential. As such, we expect that the quantum dot singlet even ground state is a superposition  $|S\rangle = u_i |0\rangle - v_i |\downarrow\uparrow\rangle$ . One important consequence is that the transport cycle between such proximitized QD and a normal lead is possible at voltage biases below the gap energy[35, 36] (but above the singlet-doublet energy difference) in a similar manner to how we have considered transport between an ABS and a normal lead. Moreover, the transport is also possible when probing the ABS at zero bias at the points of the system even-odd degeneracy ( $E_{odd} = E_{even}$ ). It can also be seen from the fact that at those points, the matrix elements of the ABS electron CAPs are not zero:  $\langle e | c_{\sigma} | o \rangle \neq 0$ ,  $\langle e | c_{\sigma}^{\dagger} | o \rangle \neq 0$ .

The ABS-QD hybridization can be observed when considering the charge stability diagram (CSD), obtained varying both chemical potentials  $\mu_1$  and  $\mu_s$ , see Fig. 2.8, where we can observe the characteristic *S-shape* bending of the even-odd degeneracy line[34].

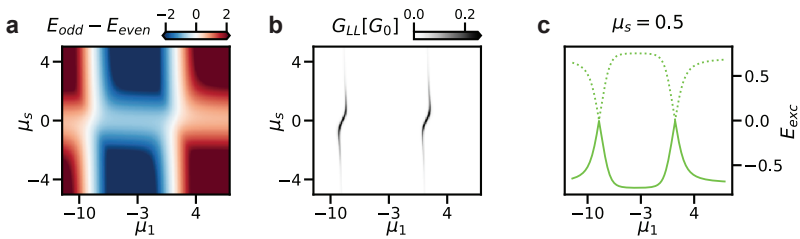


Figure 2.8: Numerical simulations of the QD coupled to the ABS. Energies are in units of  $\Delta$ . (a): Energy difference between lowest even and odd eigenstates. (b): Zero-bias conductance, measured from the normal lead connected to the QD. (c): Energy spectrum as a function of the QD detuning, corresponding to the bias spectroscopy of the QD.

Next, we bring the second dot back into the picture. We will look for a sweet spot (Sw) in the parameter space of  $(\mu_1, \mu_2, \mu_s)$ . For simplicity, we assume symmetric coupling between each of the QDs and the ABS and consider diagonal detuning of the QDs  $\mu_1 = \mu_2 = \mu_{diag}$ . But what exactly are the qualities of the sweet spot we are looking for? Since we want to find Majorana operators, we look for a degeneracy between even and odd ground state:  $E_{odd} = E_{even}$ . Next, we construct the Majorana operators  $\gamma$  out of the fermionic CAPs and introduce corresponding densities  $\rho$ :

$$\gamma_{1,\sigma,i} = d_{\sigma,i} + d_{\sigma,i}^\dagger, \quad \gamma_{2,\sigma,i} = i(d_{\sigma,i} - d_{\sigma,i}^\dagger), \quad \rho_{j,\sigma,i} = |\langle e | \gamma_{j,\sigma,i} | o \rangle|^2, \quad (2.17)$$

A useful metric indicating how a localized on a single cite Hermitian operator  $\gamma$  can switch between parity states[33, 34] is the so-called Majorana polarization(MP):

$$M_i = \frac{\sum_{\sigma} \rho_{1,\sigma,i} - \rho_{2,\sigma,i}}{\sum_{\sigma} \rho_{1,\sigma,i} + \rho_{2,\sigma,i}} \quad (2.18)$$

Notably, high MP doesn't necessarily mean that the entire wavefunction is localized on a single outer dot but rather that the Majorana operators do not overlap. Indeed, if one defines a Majorana localization metric  $\rho = \rho_{1,\uparrow} + \rho_{1,\downarrow}$ , it can be demonstrated that the finite QD-ABS coupling causes the wavefunction to leak into the ABS segment. However, in the limit of a small coupling  $t \ll \Delta$  while in the sweet spot, the  $\gamma$  operators, defined above using local quantum dot CAPs, correspond to the true Majorana operators, flipping the system parity.

Solving the numerical model, we can locate the sweet spot at the intersection of the maximum Majorana polarization on the QD 1 and the even-odd degeneracy, see Fig. 2.9. In the same figure, we plot charge stability diagrams detuning both QD chemical potentials, computed for the sweet spot but also for a few other values of the ABS chemical potential  $\mu_s$ . Interestingly, in the strong interaction model we can define similar quantities as the ECT and CAR couplings, but this time acting between even and odd occupations of the combined two-dot system. Odd states  $|S, \downarrow\rangle$  and  $|\downarrow, S\rangle$  are coupled by the spin-conserving term  $\Gamma_o$ , while the even states  $|\downarrow, \downarrow\rangle$  and  $|S, S\rangle$  by spin-flipping  $\Gamma_e$ , related to the spin-orbit interaction. In this description, the sweet spot is characterized by those two couplings being equal, while asymmetry results in the avoided crossings in the charge stability diagram, similar to the case of an interacting double quantum dot.

Finally, we demonstrate that at the sweet spot, it is impossible to distinguish between even and odd parity states by performing a local measurement. We compute a quantum dot occupation  $\langle n_i \rangle$  for both parity manifolds and also the difference between them. As we observe from Figs. 2.9(g,h), the local parity readout requires detuning of quantum dot chemical potentials. This phenomenon is related to the resilience of the information encoded in the parity to the local perturbations, being an advantage of the Majorana qubit.

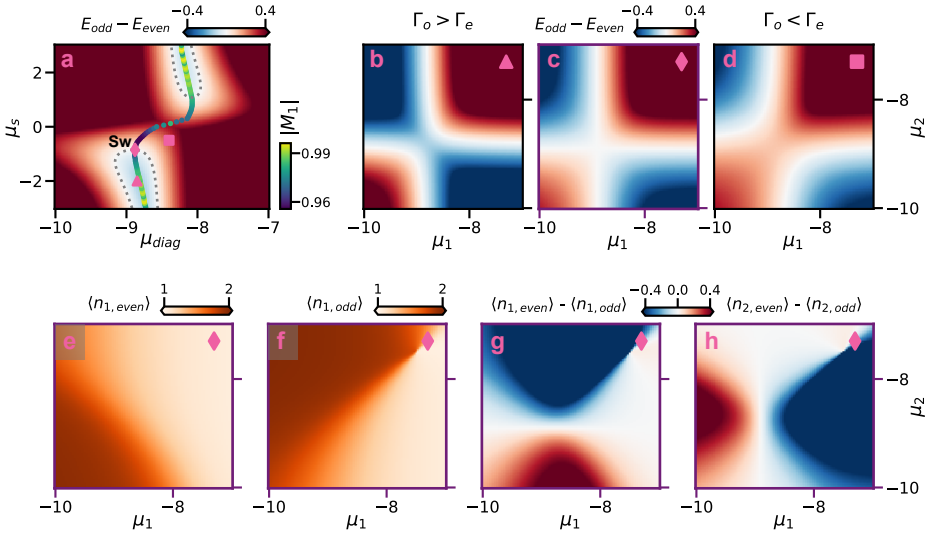


Figure 2.9: Numerical simulations of the PMM system. (a): Locating the sweet spot in  $\mu_s$ ,  $\mu_1 = \mu_2 = \mu_{diag}$  plane. The line of maximum Majorana polarization intersects even-odd degeneracy (dashed line) at the sweet spot. (b-d): CSDs, changing dot chemical potentials, plotting the energy difference between even and odd lowest eigenstates. (c) corresponds to the sweet spot, where  $\Gamma_o = \Gamma_e$ . Bottom panel: local charge measurements at the sweet spot. In (e,f), we plot occupation on the first dot separately for odd and even manifolds. (g,h): difference in occupation between even and odd states for the first and second QD.

# 3

## IMPROVEMENTS IN THE FABRICATION AND MEASUREMENTS METHODS

*Give me six hours to chop down a tree  
and I will spend the first four sharpening the ax.*

Anonymous woodsman

*This chapter presents the results of development and optimization of novel fabrication and measurement methods. We then demonstrate examples of several experiments in which such developments were instrumental.*

---

Parts of this chapter have been published in SciPost Physics **17(3)**, 074 (2024) [37],  
Nature Communications **14(1)**, 4876 (2023) [38],  
Physical Review B **110(6)**, 064518 (2024) [39]

### 3.1. OPTIMISING GATE DESIGN FOR QUANTUM DEVICES

Experiments presented in this thesis were performed with devices made on InSbAs two-dimensional electron gas (2DEG) platform[40]. This material was used due to the favorable combination of several properties. Low effective mass leads to an increased level spacing, relaxing geometrical constraints. High effective Lande  $g$ -factor allows one to achieve spin-polarization at relatively low magnetic fields, while high spin-orbit interaction can be used to create superconducting correlations between quantum levels of the same spin[41]. In turn, the induced superconductivity in the 2DEG itself arises from the epitaxially deposited aluminum layer on top of the hetero-structure, which does not form a Schottky barrier due to a favorable band-bending[22, 42].

To confine electrons to one- or zero-dimensional structures, metallic gates, patented on top of the heterostructures, are used. A dielectric layer prevents gates from shorting to the 2DEG. We operate devices in the depletion mode, meaning that the 2DEG is nominally conductive at zero gate voltage, and a negative voltage is used to deplete certain regions of it.

It is possible to engineer certain devices, such as quantum dots, using only a single layer of gates[43, 44]. However, increasing the number of gate layers (see Fig. 3.1 for a quantum dot example) allows one to significantly expand available device designs. Several layers of gates can be used to implement 2D arrays of quantum dots[45, 46]. Moreover, one can separate gates, used for different purposes (plungers, confining gates, tunnel gates), making the tuning process easier.

The important advantage of a multi-layer design is that one can avoid "puddles" of electrons inevitably forming in the 2DEG between gates. Indeed, as shown in Fig. 3.1b,c, a depletion gate (red) screens plunger and cutter gates and can be extended to the edge of the 2DEG mesa. This can become crucial when probing quantum capacitance with RF resonators connected to the plunger gates, as the electron pockets lead to a parasitic signal[47].

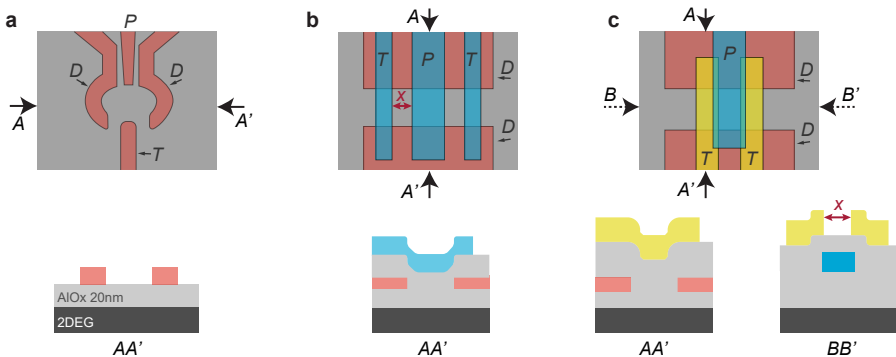


Figure 3.1: Increasing number of gate layers. Top panel: top device view, bottom panel: corresponding cross-sections. (a): typical single-layer gate design for a quantum dot. (b): two-layer design, where the first layer depletion gate (red) creates a one-dimensional channel. Expanding into three layers (c), apart from increased flexibility, allows to make the footprint smaller, bypassing the limitations of lithographical gates separation  $X$ . Depletion gates screen plunger and tunnel gates, avoiding formation of charge pockets

Using multiple layers of gates comes at the cost of increased fabrication complexity. Lithographical alignment between layers has to be performed with precision within 10 nm, which requires several considerations, including the use of an additional set of fine EBPG markers located around each individual device and exposed within one main field, avoiding stage movement.

### 3.1.1. DOUBLE QUANTUM DOT INTERFEROMETER DESIGN

The multi-layer gate approach proved crucial when designing a double quantum dot interferometer device used to demonstrate magnetic flux-tunable hybridization between two electronic levels[37]. The two QDs are connected at two locations (Fig. 3.2(e)), with magnetic flux  $\phi$  threading the inner region and imposing phase difference between the two interdot tunnel couplings. Defining the interdot tunnel couplings in the top and bottom arms as  $t_T$  and  $t_B$ , the effective coupling matrix element for the two-level fermionic system has the magnitude of

$$|t_{\text{eff}}| = |t_T + t_B| = \sqrt{|t_T|^2 + |t_B|^2 + 2|t_T t_B| \cos(2\pi\phi/\phi_0)}, \quad (3.1)$$

Physical implementation of such a device requires depleting the region between two dots while not cutting off the ring. The solution was found by using three layers of gates, with quantum dot plungers screening the arm connecting the middle depletion gate C, see Fig. 3.2(a). The clear separation between gates of different functionalities allows control of the barriers in each arm independently and tuning the double dot into a single ring-shaped dot, which can be useful for additional control experiments. As was mentioned earlier, depletion gates DG and DT screen plungers from potential charge pockets in the 2DEG.

To quantify the interdot coupling  $t_{\text{eff}}$  as a function of magnetic flux, we employed radio-frequency gate reflectometry, which is sensitive to the tunnel coupling between QDs[48, 49, 50, 51, 52, 53]. Via the quantum capacitance,  $t_{\text{eff}}(\phi)$  imparts a frequency shift on the QDL's gate resonator with a maximal value in the ground state  $\propto 1/|t_{\text{eff}}|$ . We focus on a single interdot transition and measure gate- and frequency-dependent traces of the gate L resonator's response as a function of  $B_{\perp}$ . The resonator frequency response is fitted at each gate point to extract the resonance frequency shift  $\Delta f_0^L$ , which can then be converted to the quantum capacitance  $C_q$ , using the fact that  $f_0 = 1/2\pi\sqrt{L(C + C_q)}$ . Finally, we fit the gate dependence of the  $C_q(V_L)$  to a thermal quantum capacitance model (see[37] for details), extracting the  $t_{\text{eff}}$ . The result is shown in Fig. 3.2(f), where we see a periodic modulation of  $t_{\text{eff}}(B_{\perp})$ , explicitly demonstrating control of the hybridization between two fermionic levels with the magnetic flux. The observed magnetic field periodicity agrees well with the flux value of  $h/e$ , considering lithographic dimensions of the loop (180 nm and 360 nm inner and outer radii). In charge stability diagrams, Figs. 3.2(g-i), we show examples of frequency shifts of the gate L resonator for several values of  $B_{\perp}$ , where we observe that for the smaller tunnel coupling ( $h$ ) the transition appears to be narrower, but with a stronger frequency shift.

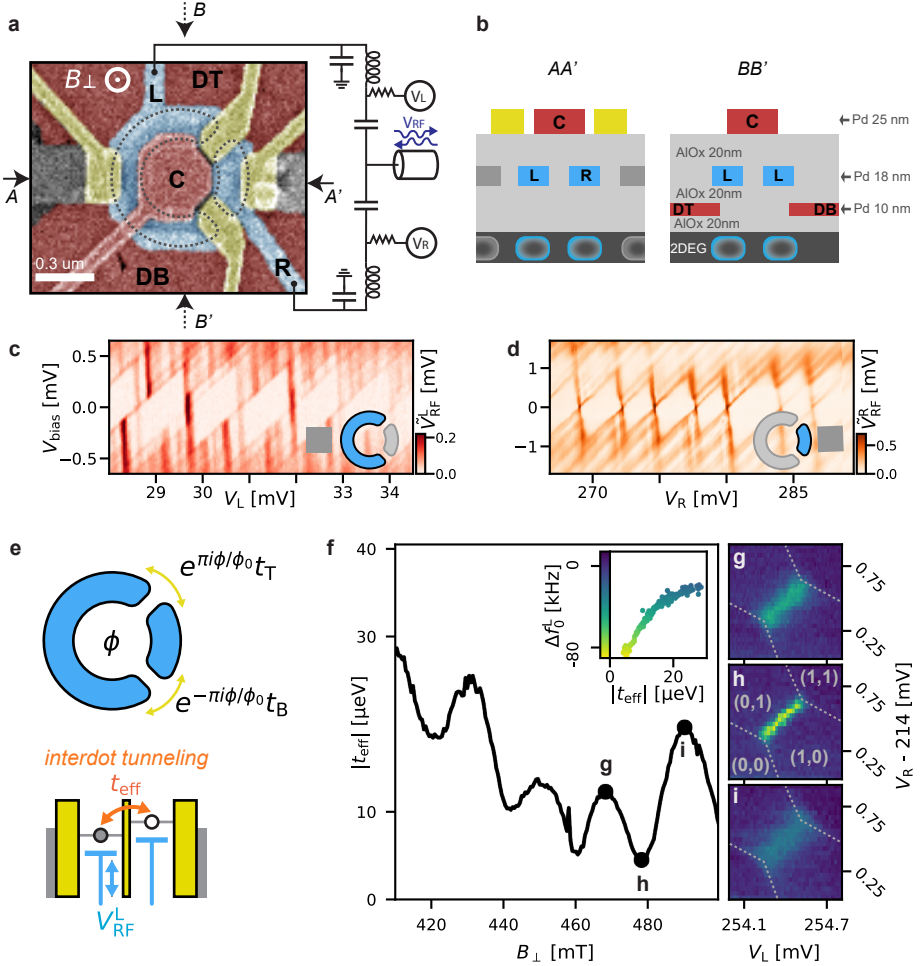


Figure 3.2: Double quantum dot interferometer experiment. **(a)**: False-color electron micrograph of a nominally equivalent device to the one measured, alongside with a schematic of the resonator circuit. Schematic linecuts are shown in **(b)**. Depletion gates (red) are located in the first (DB and DT) and third (C) layers, forming a ring-shaped channel. Tunnel barriers (yellow, in the third layer) form two QDs, while plunger gates L and R are used to tune dots chemical potential. Each quantum dot is characterised first **(c,d)**, where we show individual Coulomb diamonds with a clear level spacing. Magnitude of the reflectometry signal near the resonance frequency of the respective plunger gates resonators is plotted. **(e)**: Schematic of the double dot interferometer, threaded by a magnetic flux  $\phi(B_{\perp})$ , which imparts a phase difference on couplings in each arm. This, in turn, periodically modulates the effective inter-dot coupling  $t_{\text{eff}}$ , which we extract from the resonance frequency shift  $\Delta f_0^L(V_L)$  of the plunger gate L resonator. The extracted  $|t_{\text{eff}}|$  values as a function of  $B_{\perp}$  for a single interdot transition are shown in **(f)**. The tunnel coupling oscillates periodically with varying contrast and amplitude. The inset shows correspondence between the fit  $|t_{\text{eff}}|$  and the maximum observed  $\Delta f_0^L$  for each  $B_{\perp}$  in **(f)**. Selected charge stability diagrams **(g-i)** at few  $B_{\perp}$  values show the lineshape of  $\Delta f_0^L$  across the interdot transitions for different tunnel couplings. Dot occupations are labeled up to an unknown even number.

### 3.2. BRIDGING CONTACTS USING ALD ETCHING

For specific devices, overlapping conductance paths are necessary. One example is the inner spectroscopic probe of a Josephson junction embedded in a superconducting loop. A common approach to engineer such a device is to use a dielectric patch to isolate conducting paths from each other [54, 55], see Fig. 3.3(a) for the schematic representation. However, the lift-off of a dielectric can be complicated due to mostly isotropic deposition methods. At the same time, selective etching of the entire device, except for the patch, may also be undesirable, as it exposes the entire area to aggressive chemicals or plasma. Moreover, the additional conductance channel has to be isolated by etching the 2DEG mesa region away, which can have limitations in terms of the minimal feature size.

The proposed solution uses the depletion gate and the global dielectric to isolate conductance channels and reach the inner region using dielectric etching. The additional contact is then deposited in the same layer as the second layer of gates. Thus, for the devices presented in this thesis, said approach requires only one additional fabrication step of dielectric etching, during which we also open windows on the bond pads to facilitate wire bonding. For the aluminum oxide dielectric, we use RIE ICP etching with  $\text{Cl}_2/\text{BCl}_3/\text{Ar}$  mixture of gasses. As chlorine-based RIE attacks the 2DEG as well, we use pre-deposited Pd contact pads as the etch stop layer. These Pd contacts are also used to increase conductance in the leads coming towards the tunnel junction and increase the density of states in the 2DEG, improving the quality of the spectroscopic measurements.

Finally, we note that the method presented here can also be exploited to create compact frame-gate devices with conduction paths isolated from the boundary of the mesa, see Ch. 7

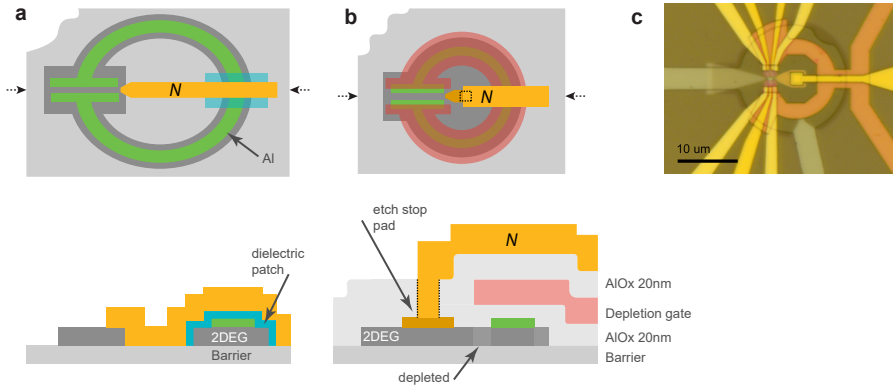


Figure 3.3: Design consideration for isolated overlapping conductance paths. As an example we show a tunnel probe inside a SQUID-loop (a), with the established solution of using a dielectric patch and removing the mesa. The method proposed here (b) is to isolate leads with the depletion gate (red) and use the dielectric etching to reach the 2DEG. This technique is used in the device consisting of quantum dots coupled through a phased-biased Josephson junction, with the optical micrograph shown in (c). This device is explored in Chs. c.

### 3.3. TWO-STEP WET AL ETCHING FOR COMPACT JJS

One of the first steps of the fabrication process for the devices discussed in this thesis is usually to pattern the epitaxial aluminum layer on top of the 2DEG. This is done with selective wet etching using Transene-D as the active chemical and PMMA as a mask. Unfortunately, the process is accompanied by the creeping of the etchant solution underneath the PMMA mask, affecting the shape of the resulting aluminum structure, see Fig. 3.4(a). The problem becomes detrimental when device design requires making a Josephson junction (JJ), which is both narrow and short. One example of such a device (see Chs. 4,6) consists of two QDs coupled via a JJ, with the one-dimensional channel formed by the depletion gates, imposing strict constraints on the length (separation) between the superconducting electrodes. On the other hand, the JJ has to be narrow to ensure the same quantum state is accessible from both sides, unlike[54].

We found a way to mitigate the creeping problem for the compact JJs by separating wet etching into two steps, Fig. 3.4(b). It was observed that the creeping is less severe for narrow lines, thus allowing improved control of the junction dimensions.

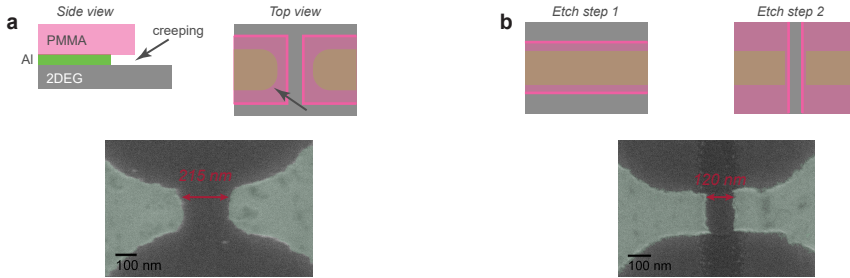


Figure 3.4: Comparing single-step(a) and two-step(b) aluminum wet etching process. The top panel schematically illustrates the PMMA etch mask (pink), as well as the creeping of the etchant. The bottom panel shows typical SEM micrographs of the Josephson junctions for each method. The two-step process reduces minimal lead separation by approximately a factor of two.

#### 3.3.1. FLUX-TUNABLE JOSEPHSON EFFECT IN A FOUR-TERMINAL JUNCTION

One application of the Al patterning method described above is engineering compact multiterminal JJs. Andreev bound states (ABS), present in the junctions, can hybridize with each other, forming a so-called Andreev molecule[56, 57]. Exploring this rich physics necessitates creating compact JJs.

In our work [39], we focus on exploring the current-phase relations of a four-terminal junction (4TJJ). The junction is embedded in two asymmetric DC SQUIDS penetrated by independently controllable magnetic fluxes, arising from the global out-of-plane magnetic field  $B_{\perp}$  and a flux line located around just one of the SQUID loops and made from the sputtered superconducting NbTiN strip. This allows us to control two phase differences across pairs of terminals in the junction, see Fig. 3.5(b,c).

Accordingly, we can measure SQUID oscillations containing information about the CPR across their corresponding 4TJJ terminals in the form of a current-flux relation (CFR).

Using four instead of three terminals, we are able to measure a Josephson effect, which is entirely ‘nonlocal’ in that the CPR between two superconducting terminals is modified by a phase difference across a completely independent pair of terminals. Correspondingly, two terminals of the 4TJJ form a tunable  $\phi_0$ -junction with a phase offset variation over a range larger than  $0.2\Phi_0$  where  $\Phi_0 = h/2e$  is the superconducting flux quantum.

It is crucial to emphasize that the observed non-local behavior is not necessarily indicative of the hybridization between ABS in 4TJJ. Indeed, the system can be modeled as an array of two-terminal junctions[39, 58], yielding the  $\phi_0$ -junction effect in the absence of a hybridized ABS spectrum. Thus, it is necessary to have additional sources of information, such as tunneling spectroscopy measurements, to establish the Andreev molecule behavior with confidence.

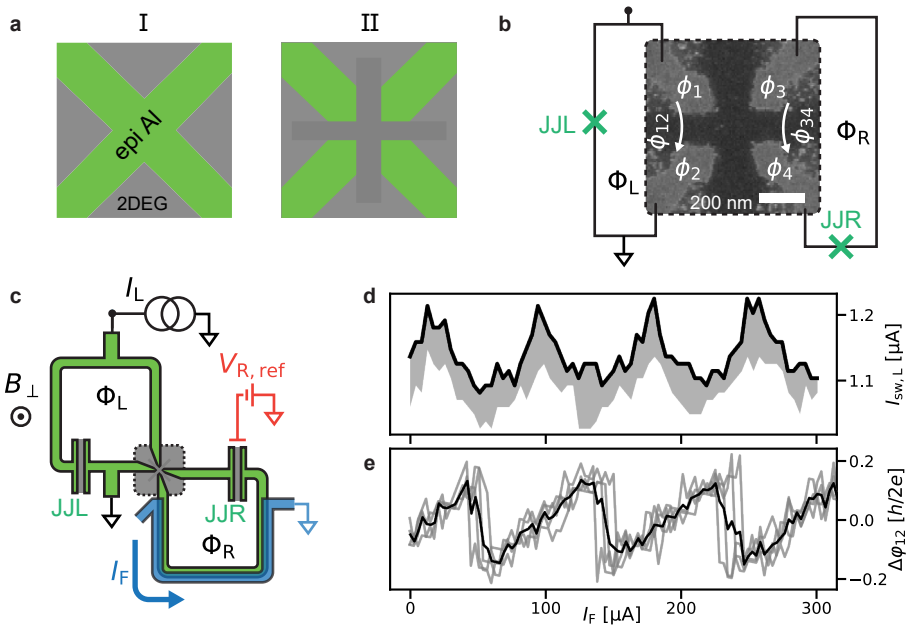


Figure 3.5: Demonstration of the non-local Josephson effect. (a): Forming the Josephson junction with two-step aluminum etching. (b): SEM micrograph of the measured device, schematically illustrating two SQUID loops, each threaded by a magnetic flux. (c): Schematic of the experiment. Left SQUID is biased with the current  $I_L$ , which is used to extract the switching current  $I_{SW,L}$ . Out-of-plane magnetic field  $B_{\perp}$  tunes flux in both SQUIDS, while flux line  $I_F$  affects only the flux in the right SQUID. Gate  $V_R$  can be used to pinch off the right SQUID for a control experiment and calibrations. Figure (d) shows modulation of the switching current in the left SQUID when changing  $\Phi_R(I_F)$ , while  $\Phi_L(B_{\perp})$  is fixed. Finally, we extract the left SQUID current-phase relation as a function of  $I_F$ , demonstrating tunable  $\phi_0$  behavior.

### 3.4. RESONATORS FOR REFLECTOMETRY MEASUREMENTS

As was briefly shown in the example of the double-dot interferometer experiment, radio frequency (RF) methods can be used to extract additional information about a quantum system otherwise not accessible with the standard low-frequency (lock-in) techniques, such as tunnel couplings in an isolated system, or the Sisyphus resistance[59, 60] of a single-lead dot. Moreover, using RF methods allows to significantly speed up conductance measurements[61, 62, 63]. When using RF methods one has to use components with characteristic impedance  $Z_0$  of  $50\ \Omega$ , and since a typical quantum device impedance is much higher, matching resonator circuit has to be used in order to receive any considerable signal. For the comprehensive overview of the RF methods the reader is referred to[53].

#### 3.4.1. OPTIMISING RESONATOR PARAMETERS

For the RF experiments presented in this work, we employ multiplexed[64] off-chip resonators, with the circuit represented schematically in Fig. 3.6. The actual resonator chip contains an RF feed-line; coupling capacitors  $C_C$ , allowing for additional circuit tuning, multiplexing, and forming a bias-tee together with the resistance  $R_{\text{bias}}$ ; and spiral inductors  $L_x$ . The details of the resonator chip fabrication are described below in sec. 3.5. The capacitance of the resonator circuit comes from the parasitic capacitance  $C_p$  of the bond-wire between the resonator chip and a 2DEG device chip, and is usually close to  $0.3\ \text{pF}$ . Fixing bias-tee resistance to be about  $5\ \text{k}\Omega$ , we are left to select the optimal inductance  $L_x$  and capacitance  $C_C$ .

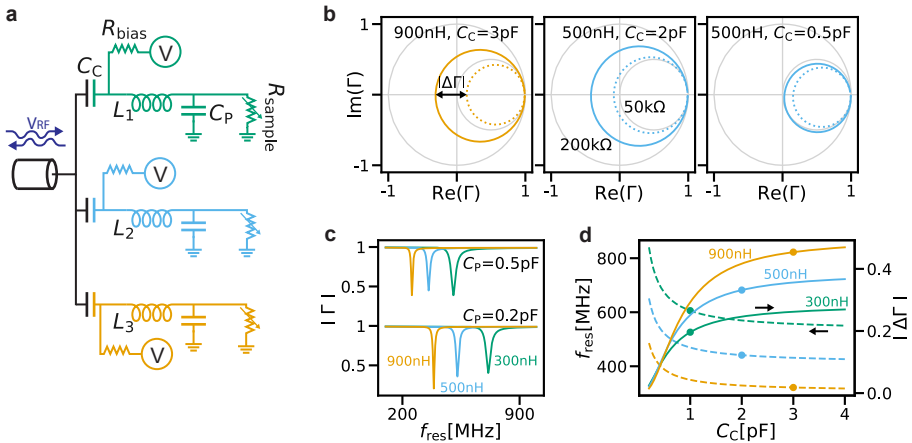


Figure 3.6: Considerations for selecting optimal resonator parameters for the circuit schematically represented in (a). Panel (b) demonstrates Smith charts for several resonator parameters when measuring a device of  $200\ \text{k}\Omega$ (solid) and  $50\ \text{k}\Omega$ (dashed) resistance. Panel (c) shows frequency crowding issue, considering variation in the parasitic capacitance  $C_p$ . Effect of the coupling capacitor  $C_C$  on the resonance frequency (dashed lines) and the signal  $|\Delta\Gamma|$  is shown in (d), where signal corresponds to the resistance difference. Solid dots in (d) correspond to the selected parameters. Model includes a  $10\ \Omega$  series resistance with the inductor, accounting for losses.

To make our reasoning more concrete, we focus on measuring a realistic resistive device, with the variation in resistance from  $50\text{ k}\Omega$  (tunneling conductance) to  $200\text{ k}\Omega$  (close to pinch-off), see Fig. 3.6(b). Using the reflectometry circuit, we can detect the change in the reflection coefficient  $\Gamma$  between two device regimes, defined as  $|\Delta\Gamma|$ . Increasing the resonator inductance and the coupling capacitance leads to a larger signal  $|\Delta\Gamma|$ , as can be seen in Fig. 3.6(d). Unfortunately, we have to consider a few additional restrictions. Firstly, we need to space resonators in frequency band  $100\text{ MHz} - 1\text{ GHz}$  (defined by the experimental setup), ensuring individual addressability, which is complicated by the uncontrollable variations in the parasitic capacitance  $C_P$ , Fig. 3.6(c).

Secondly, fabrication and design limitations have to be taken into account. The footprint of a spiral inductor limits it to a maximum value of a few  $\mu\text{H}$ . Reducing the spacing between windings is undesirable, as it leads to an unwanted parallel capacitance. The interdigitated coupling capacitor also has a footprint scaling with its value. While reducing the separation between fingers is achievable lithographically, it significantly affects reliability and can lead to parasitic inductances.

As such, we design off-chip resonators with inductances typically within  $0.2 - 1.5\ \mu\text{H}$ , and coupling capacitors of  $1 - 4\text{ pF}$ , with smaller  $C_C$  used for smaller inductance resonators. The design and optical micrographs of a typical resonator chip are presented in the Figs. 3.7(c–e), while Figs. 3.7(a–b) demonstrate the characterisation measurement of a pinch-off curve with  $10\text{ mV}$  DC bias applied. Defining  $\tilde{V}^{\text{RF}}$  as the distance from the complete pinch-off, we see that this quantity shows similar features as the DC current.

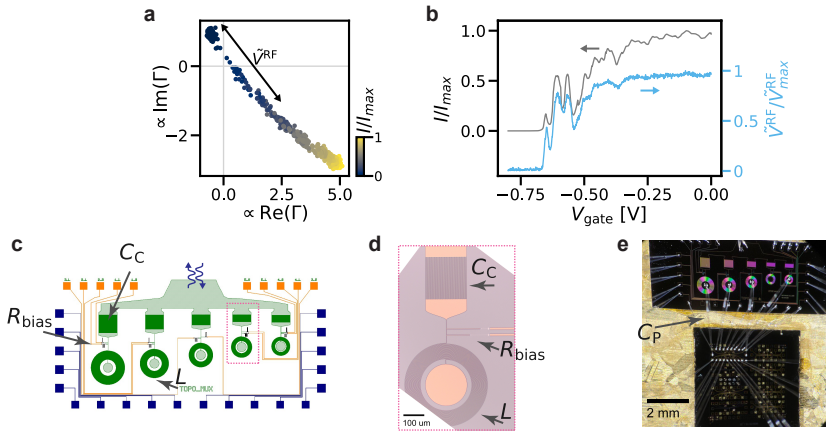


Figure 3.7: Measurements with the off-chip resonators. (a): complex reflected signal, recorded when measuring the pinch-off curve. Comparison between RF and DC signals is shown in (b). Bottom panel shows resonator chip design (c), with the zoomed-in (d) optical micrograph. (e): resonator chip, connected to the 2DEG device chip via wire-bonding.

### 3.4.2. RASTERING MEASUREMENTS WITH REFLECTOMETRY

As mentioned above, RF techniques allow a much faster data acquisition rate than standard lock-in methods. To fully benefit from this speed, we must ensure that the device

parameters can be tuned at a comparable rate. This can be achieved using the rastering method, see Fig. 3.8. We use an arbitrary waveform generator (AWG), applying a two-channel sawtooth signal. The first channel has a single wave period, while the second channel has as many periods  $N_2$  as the number of lines in the resulting diagram. The frequency  $f_B$  of the fast channel is limited by the RC filter cut-off frequency. The number of points in each line  $N_1$  is limited by the acquisition device memory  $N_1 \cdot N_2$  and the acquisition bandwidth  $f_B \cdot N_1 < BW$ .

Sawtooth signals from the AWG are connected to the optical isolator, breaking any potential ground loops, and are combined with the constant DC offsets using a voltage divider. They are then fed into the device through a set of filtered low-frequency fridge lines.

The AWG starts outputting the signal when initiated by the control software. Simultaneously, AWG outputs a trigger signal, which is fed into the acquisition device, in this case, a vector network analyzer (VNA). On trigger event, VNA records  $N_1 \cdot N_2$  points such that the total acquisition time equals the period  $T_A$  of the slow channel wave. The VNA measures the complex reflected signal amplitude, with the RF circuit designed in such a way that the incident and reflected from the resonator waves are separated into two lines with the help of a directional coupler. Finally, the output one-dimensional data string from the VNA is mapped into a two-dimensional matrix corresponding to the two swept parameters.

As an example, we show a measurement of a charge stability diagram of a double quantum dot system, comparing the RF rastering Fig. 3.8(b) with a standard lockin measurement (c). Note that here, the RF measurement time was not optimized and, without a significant decrease in quality, can be lowered further down to 10 s.

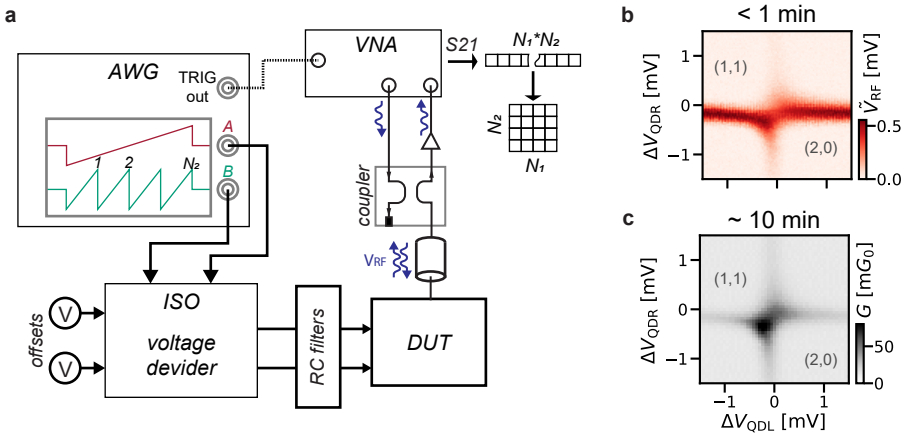


Figure 3.8: (a): Schematic of a rastered reflectometry measurement. The arbitrary wave generator is used to provide two sawtooth signals, while the synchronized vector network analyzer acquires a complex reflection coefficient. This method allows to significantly reduce the measurement time of the charge stability diagram (b) compared to the lock-in measurement (c). Charge occupations are labeled up to an arbitrary even number.

### 3.5. APPENDIX: FAB FLOW FOR THE OFF-CHIP RESONATORS

High-resistivity Si wafer (with native oxide) is cleaned in fuming nitric acid for 5 minutes, rinsed, followed by native oxide removal in 40% HF aqueous solution for 5 minutes. The wafer is again rinsed in DI water and immediately transferred to the load lock of the deposition machine. We then use reactive sputtering in  $N_2/Ar$  DC magnetron plasma, depositing 200nm of NbTiN from NbTi target. The wafer is covered in protective resist and diced into rectangular pieces.

We proceed with patterning NbTiN. We first spin-coat PMMA A4 495 @4k rpm, bake on a hotplate, and then spin-coat negative resist ARN 7520.17 @4k rpm, which is also baked on a hot plate @90°C for 1 min. The resist is exposed in electron beam pattern generator (EBPG) and developed in the alkaline solution. This leaves PMMA layer intact. We then proceed with the two-step reactive ion etching. First, using oxygen plasma, PMMA, not protected by the negative resist, is burned away, revealing NbTiN. Second, NbTiN is removed in the fluorine-based ( $CF_4O_2$ ) plasma. The PMMA can be now dissolved in any suitable organic solvent, while ARN is lifted-off, thus avoiding the problem of removing hardened negative resist.

Finally, bias-tee resistors are deposited using standard liftoff with a PMMA mask. We use electron-beam evaporated chromium 30 nm thick, overlapping with NbTiN. To ensure good ohmic contact, NbTiN is first cleaned from any surface oxides in the same deposition chamber using Ar ion-beam milling.

The reliability bottleneck for the resonator fabrication are potential shorts in the interdigitated capacitors. Thus, one has to avoid any contamination during the NbTiN patterning process, using appropriate resist filters, etc.

### 3.6. APPENDIX: FAB FLOW FOR INSBAS CHIPS

Lastly, we present the entire fabrication flow, used to make devices presented in the subsequent chapters. Fabrication on InSbAs 2DEG is complicated due to the presence of the Sb in the heterostructure, which can form disordered large band-gap semiconductor AlInSb[65]. As such, the temperature budget is limited to 50°C, which is below the glass transition point of the PMMA or ARN resists, affecting the quality of lithography and limiting the resolution. The resist "baking" is done at room temperature in vacuum environment for the duration of 1–2 hours.

**1. Coarse Al etching** Starting with a 2DEG with the epi-Al layer, we clean the surface first in the organic solvent AR600-71 (dioxolane) and then in a barrel etcher with the oxygen plasma (400W power, 0.66mbar, 60sec) *this ensures significantly improved resist adhesion*. We then spin-coat (here and for all subsequent lithographic steps @4000 rpm unless specified otherwise) adhesion promoter AR 300-80 and dry it in the vacuum oven for 1h, followed by coating PMMA A4 950, dried for 2 hours. The pattern is defined in EBPG. *We use proximity error correction in the region 15μm around devices, splitting exposure into medium and coarse zones*. After the resist development (@RT, in MIBK:IPA 1:3 volumetric ratio), we again perform a descum in the barrel etcher (400W power, 0.66mbar, 60sec). *We speculate that this not only removes any resist residues but also smoothens the undercut, reducing creeping*. The sample is again dried in the vacuum oven for a few hours *potentially removing any*

*remaining developer and stabilizing PMMA mask.* The sample is then etched for 6 s in Transene-D aluminum etchant, kept in 48 °C. The sample is rinsed *immediately* in water beakers of the same temperature adjacent to the beaker with the etchant. Resist is removed in AR600-71 solvent.

2. **Mesa etching** Using the Al layer as a mask, 2DEG is patterned to form required conductive channels. We use the mixture of 560 mL DI water, 9.6 g citric acid monohydrate, 4 mL 85% phosphoric acid and 5 mL 31% hydrogen peroxide. Etching time of 70 s results in the etch depth of about 60 nm. *Considering the 2DEG thicknesses of 30 nm, this depth is enough to isolate mesa regions from each other.*
- 3, 4. **Fine Al etching I and II** Here, the same fabrication as for the coarse Al etching is used. Only a small part of the chip is exposed in EBPG, *including Al on the bondpads.* We perform Al etching at the reduced temperature of 38 °C with time increased to 10 s. *Small amount of aluminum residues is not crucial during that step.*
5. **Fine ohmic contacts** Using lift-off lithography with PMMA A4 950 resist, we deposit thin ohmic contacts of 3 nm Ti and 10 nm Pd. The deposition in the electron-beam evaporator is preceded by a gentle ion-milling without breaking the vacuum. Those contacts reduce the resistant path leading towards the device, improve tunneling spectroscopy quality, and act as an etch stop for the following dielectric etching. Here and in the following metal depositions, liftoff is done in AR600-71 (dioxolane) @40 °C. We perform sonication in the ultrasonic bath at the lowest setting for 1 min.
6. **Bond pads** We deposit relatively thick (50 nm Ti, 50 nm Cr, 5 nm Pd) bonding pads to facilitate wire bonding, with Pd acting as an etch stop for the following dielectric etching.
7. **AlOx dielectric** Dielectric is deposited globally using atomic layer deposition @40 °C. *Reduced temperature requires a significant increase in the cycle time.* Layer thickness is 20 nm. Prior to the deposition, the sample is cleaned in the oxygen plasma barrel etcher.
8. **Fine gates** Using ARP6200.09 resist, which provides better feature size, we deposit the first layer of gates, consisting of 3 nm Ti and 12 nm Pd. *The thickness is kept as small as possible to allow the climbing of the fine gates of the subsequent layers.*
9. **Additional gate lead resistance** Using the lift-off method, we deposit meandering lines of thin 18 nm Cr, capped with 3 nm Pd. *The resistors 100 kΩ in value prevent RF signal leakage into the ground due to capacitive coupling between plunger gates and depletion gates.*
- 10, 11. **Coarse gates, dielectric II** Using lift-off lithography with double layer PMMA A6 495 / PMMA A4 950 resist, we deposit 10 nm Ti, 75 nm Au and 5 nm Pd thick gates. *The thickness guarantees climbing of the 2DEG mesa boundary.* After the lift-off, we proceed with dielectric deposition (same as 7)

**12. Dielectric etching** Using ARP6200.13 resist mask (with AR300-80 adhesion promoter), we perform ICP RIE etching with  $\text{Cl}_2/\text{BCl}_3/\text{Ar}$  mixture of gasses. Pd acts as an etch stop layer. *Etch windows are also open at the bond pads.*

**13, 14. Fine and coarse gates II** Deposited in the same manner as steps 8,10, with the thickness of fine gates II increased to 18 nm Pd and coarse gate II to 120 nm Au, without Pd capping.

**15, 16, 17. Dielectric III, fine and coarse gates III** Deposited in the same manner as the second layer, with the thickness of fine gates III increased to 25 nm.

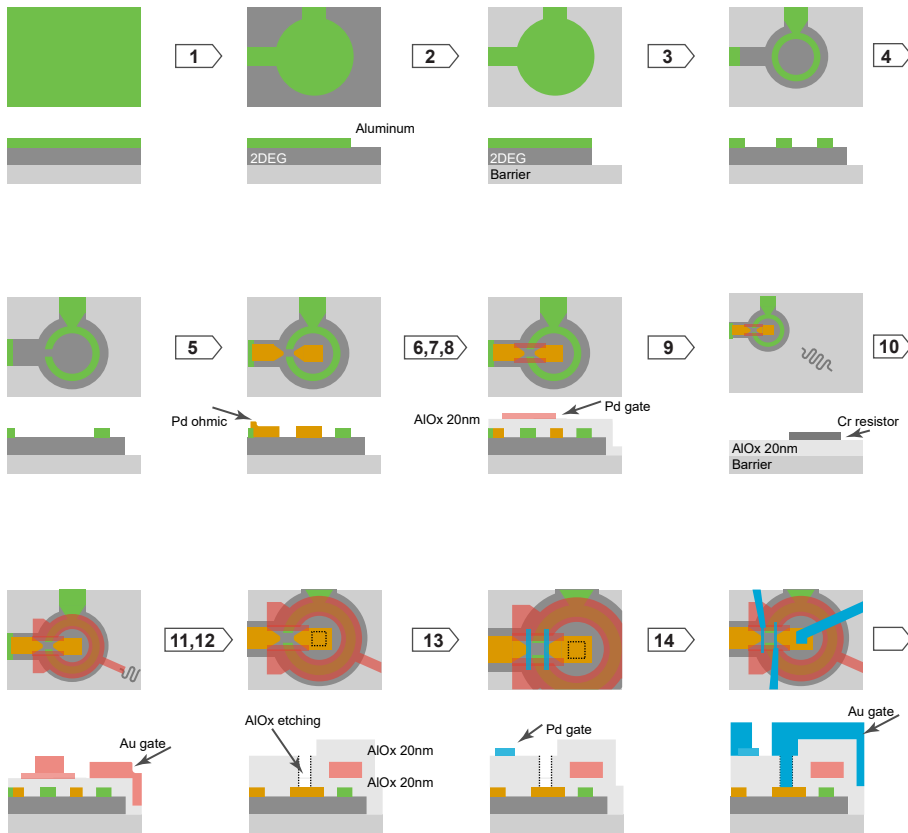


Figure 3.9: Fabrication flow for a typical device on InSbAs 2DEG. Not all of the fabrication steps are shown. Lithography is not shown. Side view does not always correspond to the specific cross-section and is only used to highlight important device aspects.



# 4

## COUPLING QUANTUM DOTS VIA A PLANAR JOSEPHSON JUNCTION

**Ivan KULESH, Sebastiaan R. ROELOFS, Qingzhen WANG,  
Sebastiaan L. D. TEN HAAF**

*In this chapter, we explore non-local transport arising when two quantum dots (QD) are coupled via an Andreev bound states (ABS) in a planar Josephson junction, defined in a two-dimensional electron gas. Using QDs as energy and charge filters, we can, with high efficiency, separate Cooper-pair splitting (CPS) from elastic cotunneling (ECT) and local processes. The junction is embedded in a superconducting loop, thus allowing us to control the phase difference across it with an applied flux, in turn periodically modulating the amplitudes of the CPS and ECT processes.*

## 4.1. INTRODUCTION

Cooper-pair splitting (CPS), arising due to crossed Andreev reflection (CAR) into spatially separated terminals, is a potential source of entangled electron pairs[66, 67, 68]. It can naturally be accompanied by elastic co-tunneling (ECT) and local Andreev reflection (AR) processes. Quantum dots (QDs) can be used to force electron flow into separate leads[67], as the charging energy suppresses the double occupation of a single QD and thus local AR. This approach was explored experimentally in several material platforms[69, 70, 71, 72, 73]. However, the amplitude of the CPS in the above studies was not independently controlled and limited due to the exponential decay of an electron wavefunction in the bulk superconductor.

It was recently discovered that an Andreev bound state (ABS) can mediate CAR and ECT through a second-order tunneling process[31, 32, 74]. This provides several crucial advantages, the first being that the magnitudes of the non-local processes are no longer exponentially suppressed with the superconducting segment length (and, hence, the inter-dot separation). The second aspect is the dependence of the CAR and ECT amplitudes on the ABS parameters: energy and the coherence factors  $u$  and  $v$ . In semiconducting-superconducting hybrid devices, those parameters can be tuned electrostatically with a gate. This tunability drastically widens the potential applications, including the implementation of an artificial Kitaev chain[11, 12].

In a simple model of no Zeeman splitting of the ABS and QDs with a single level each, the currents originated from ECT and CAR depend on the ABS coherence factors ( $u$  and  $v$ ) and energy  $E_{\text{ABS}}$  as following[31, 32]:

$$I_{\text{ECT}} \sim \left| \frac{u^2 - v^2}{E_{\text{ABS}}} \right|^2, \quad I_{\text{CAR}} \sim \left| \frac{u \cdot v}{E_{\text{ABS}}} \right|^2 \quad (4.1)$$

The natural system to host ABS is a semiconducting Josephson junction (JJ)[54, 75]. In a JJ, one can manipulate ABS with the phase difference  $\Delta\phi$  between superconducting (SC) electrodes. Interestingly, the phase difference affects not only the energy of the ABS but also the coherence factors  $u$  and  $v$ . This indicates that  $\Delta\phi$  can be used to change not only the absolute value but also relative magnitudes of the ECT and CAR processes, acting as an additional control knob alongside electrostatic gate[30]. As such, phase control has the potential to expand the operational regime and provide several practical advantages, including the absence of electrostatic cross-coupling.

We implement the device using InSbAs two-dimensional electron gas with epitaxial aluminum layer[40], see Fig. 4.1. The Josephson junction is defined by selectively etching Al in a two-step process, described in chapter 3. A one-dimensional channel is established by the depletion gate (red), imposing constraints on the junction length such that the terminals are not screened. The junction is embedded in a grounded SC loop  $72 \mu\text{m}^2$  in area, while out-of-plane magnetic field  $B_{\perp}$  imposes phase difference  $\Delta\phi = \phi_2 - \phi_1$ . Normal leads (yellow) can be independently biased with voltages  $V_1$  and  $V_2$  while monitoring currents  $I_1$  and  $I_2$  flowing in them. The chemical potentials of the QDs and ABS are controlled with the plunger gates (blue) located in the second layer of gates. The confinement is achieved with the tunnel gates (purple), shown only in Fig. 4.1(b). The detailed fabrication description can be found in 3.6. The measurements were performed in a dilution refrigerator with a base temperature of 40 mK.

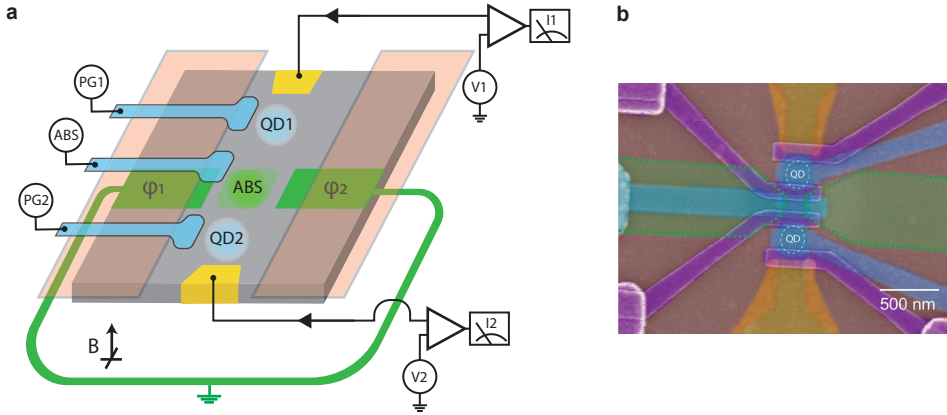


Figure 4.1: Schematic of the device and measurement circuit (a) alongside the SEM micrograph (b) of the device similar to the one measured. Andreev bound state is formed between superconducting terminals  $\phi_1$  and  $\phi_2$ , while quantum dots are defined by tunnel gates (purple) inside a channel between depletion gates (red). Plunger gates (blue) are used to change QDs and the ABS chemical potentials.

## 4.2. ABS SPECTROSCOPY

As the processes of interest, ECT and CAR, are mediated by an Andreev bound state, we require the ABS to be extended and accessible from both sides of the junction. To verify that, we perform the tunneling spectroscopy of the ABS by energizing only the inner tunnel barriers and measuring the differential conductance  $G_{xx} = dI_x/dV_x$ . We compare the spectrum on both sides of the junction, as well as the non-local spectroscopy[76, 77], varying the ABS chemical potential, Fig. 4.2. Correlated features in the conductance indicate the presence of the extended ABS. While the non-local signal on one side of the JJ demonstrates sign change at the energy extrema points, Fig. 4.2(c), consistent with the zero ABS charge  $u = v$ , that is not the case when measuring in the opposite configuration, Fig. 4.2(d). We speculate that this discrepancy arises due to the charge filtering in the tunnel barrier as a result of accidental dot formation[78].

We then perform the spectroscopy as a function of the out-of-plane magnetic field  $B_{\perp}$ , Fig. 4.3, demonstrating the periodic energy modulation in agreement with the loop area. Importantly, unlike the single ABS model used in[30], the JJ contains multiple states, responding to the change in the phase difference  $\Delta\phi(B_{\perp})$ . It is possible that multiple states can mediate the non-local processes, with the total amplitude being the sum over multiple paths. Moreover, some of the sub-gap states show stronger phase modulation compared to the isolated state of interest with strong chemical potential dependence. This behavior is especially detrimental close to the  $\Delta\phi = \pi$ , where multiple sub-gap states reach zero, effectively closing the superconducting gap and obscuring the measurements of the non-local transport phenomena.

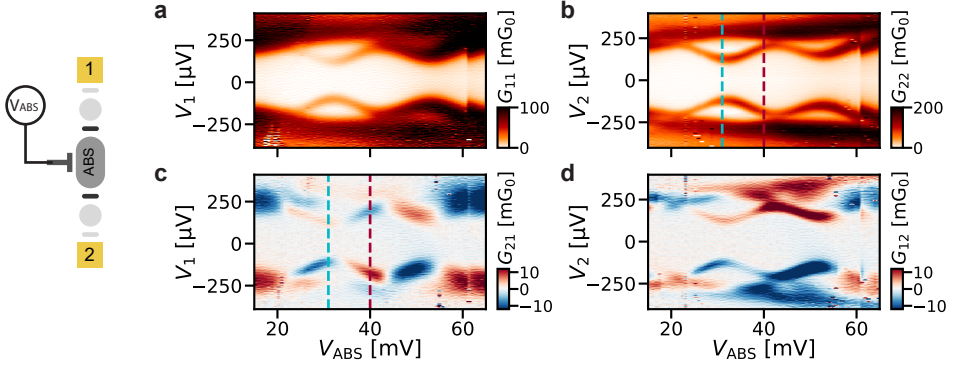


Figure 4.2: Gate control of the ABS. Local (a,b) and non-local (c,d) tunneling spectroscopy as a function of the ABS chemical potential, controlled by the gate voltage  $V_{\text{ABS}}$ . Dashed lines indicate the gate values at which flux conductance features are taken. Correlated conductance features indicate the presence of an extended ABS in the junction, accessible from both sides.

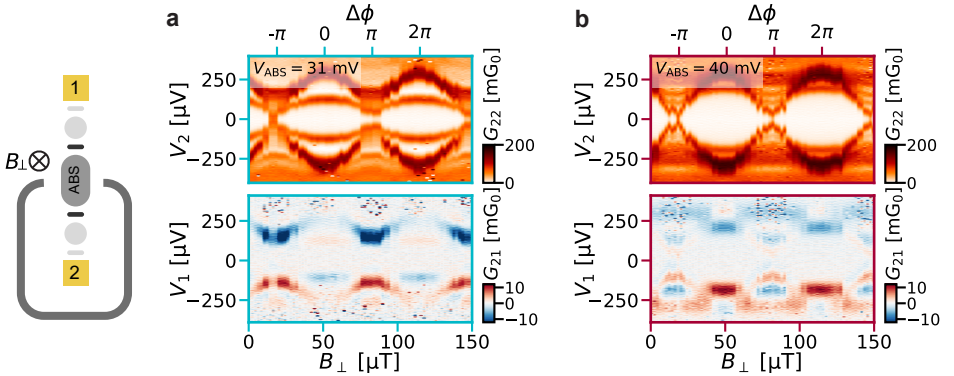


Figure 4.3: Tunneling spectroscopy as a function of the superconducting phase difference, controlled by the out-of-plane magnetic field  $B_{\perp}$ . ABS gate is fixed at two different values (corresponding to panels a and b). We observe that both the energy and charge character of the ABS change with  $\Delta\phi(B_{\perp})$ . At phase differences  $\Delta\phi = (2N + 1)\pi$  the induced gap approaches zero.

### 4.3. ECT, CAR

Established that the ABS in the junction has the wavefunction extending into both sides, we proceed with forming quantum dots. For that, we energize all tunnel barriers such that the couplings of the QDs to the ABS are strong enough to measure considerable currents but sufficiently weak that the QDs are not hybridized with the ABS. The latter is verified by the presence of the superconducting gap in the bias-plunger charge stability diagrams (absence of zero-bias Coulomb peaks). The charging energy of both quantum dots is about 1.5 mV (Fig. 4.4), which is significantly larger than the induced superconducting gap in the JJ ( $250\mu\text{V}$ ), ensuring only a single electron transport through each

QD. The sizeable orbital energy spacing  $0.8\text{ mV}$  allows us to consider a single level for all relevant processes.

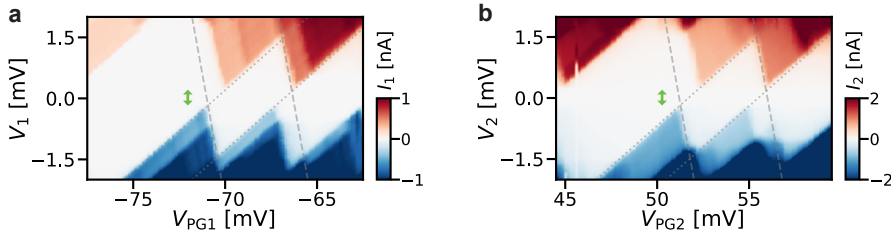


Figure 4.4: Coulomb diamonds, measured for individual QDs, demonstrate the absence of the local current around zero bias (green arrow).

To focus on the non-local transport processes, we apply voltage bias  $100\mu\text{V}$  in amplitude on both leads, below the energy of the ABS, see Fig. 4.5(a,c). The polarity of the bias is used for the differentiation between ECT and CAR processes; namely, a bias of the same sign allows for currents of the same directions flowing in both leads, corresponding to CAR, while the opposite bias allows for ECT. Fixed the bias voltage, we record charge stability diagrams, varying plungers of both QDs around charge degeneracy points, and measuring currents flowing in the terminals, Fig. 4.5(b,d).

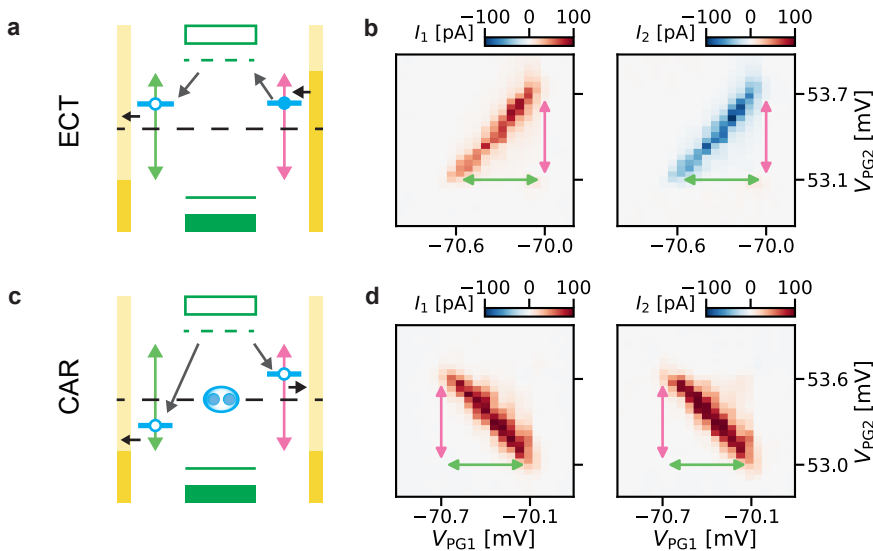


Figure 4.5: Non-local transport processes. The left panel shows schematically the transport cycles for ECT (a) and CAR (c). Green rectangles indicate a quasiparticle continuum, while dashed (solid) lines indicate the ABS. Bias in the normal terminals (yellow) is kept below the energy of the ABS and, at the same time, acts as the limit for the chemical potential span at which a non-local process is allowed (green and pink arrows). QD levels have to be (anti-) aligned to fulfill energy conservation.

The energy conservation requirements for the coherent second-order non-local processes impose restrictions on the quantum dot chemical potentials  $\mu_x$ , Fig. 4.5(a,c). As such, elastic co-tunneling is only possible when  $\mu_1 = \mu_2$ , corresponding to the positively sloped diagonal line in the CSD. In contrast, the energy of electrons forming a Cooper pair during CAR, or arising from splitting of such, must have opposite and equal energies w.r.t. the Fermi level, corresponding to the condition  $\mu_1 = -\mu_2$ . This restricts CAR to occur only at the ant-diagonal line in the CSD. At the same time, the bias window limits the span of the non-local process – once the QD enters a Coulomb blockade, it can no longer provide (accepts) electrons. We note that the span of the ECT and CAR in Fig. 4.5(b,d) roughly corresponds to the bias window of  $2 \times 100 \mu\text{V}$  when converting gate voltages to the chemical potentials using the appropriate lever arms  $\alpha_{1,2} \approx 0.33$ .

## 4

#### 4.4. SPIN BLOCKADE

The spins of the electrons, involved in the non-local processes, have an effect that depends on the bias configuration and the QDs occupations. We focus on the specific example of  $0 \leftrightarrow 1$  transitions for both QDs, where Pauli spin-blockade[79] is irrelevant, and at zero magnetic field an electron with arbitrary spin direction can occupy the QD level. This allows a Cooper pair to be split, with electrons of opposite spin tunneling into QDs. Elastic co-tunneling is also possible, regardless of a possible spin rotation in the ABS region.

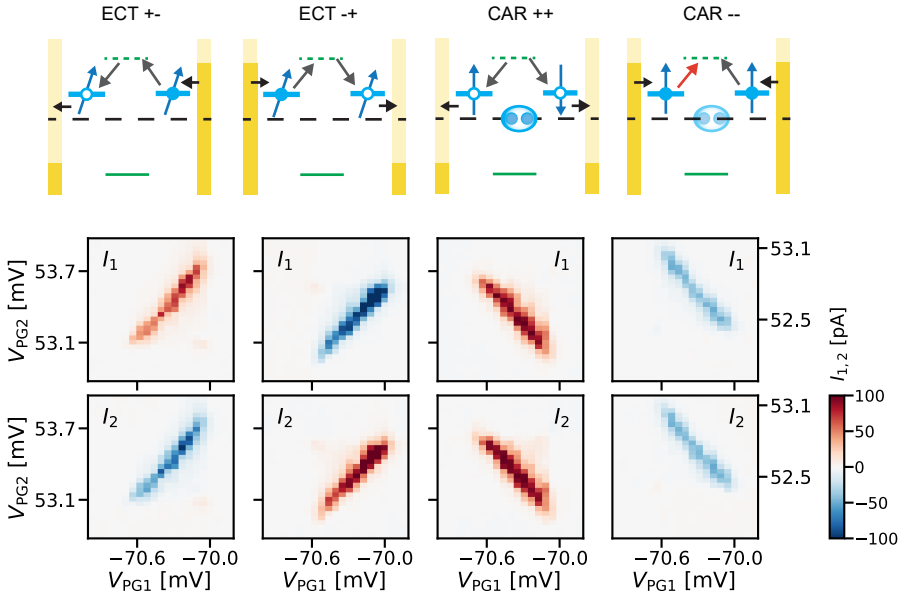


Figure 4.6: Spin-blockade of non-local processes. For the  $0 \leftrightarrow 1$  transitions on both QDs, only the process of two electrons merging into a Cooper pair (CAR $--$ ) is suppressed. It happens when electrons enter both QDs with the aligned spin. This results in the reduction of current from  $\sim 100 \text{ nA}$  for CAR $++$  to  $\sim 50 \text{ nA}$  for CAR $--$ .

However, when considering a non-local process of two electrons forming a Cooper pair (CAR $^-^-$ ), the *s-wave* nature of the superconductor requires that the electrons form a spin-singlet. For that reason, QDs have to provide electrons with the opposite spin. Electrons entering QDs from the leads have no preferred spin orientation and accidentally can have the same one. This prevents the CAR process, with electrons "stuck" on the dots. Eventually, spin relaxation, potentially caused by the hyperfine interaction[80, 81], changes the spin orientation, and the transport is restored. This reasoning explains reduced (but finite) current for the CAR $^-^-$  configuration in Fig. 4.6. Finally, we note that when considering next charge transitions  $1 \rightarrow 2$ , the Pauli exclusion principle, as well as the availability of both spin-species in occupation 2, has to be taken into account, resulting in different configurations being blocked[38].

## 4.5. TUNING ECT AND CAR AMPLITUDE

As mentioned earlier, amplitudes of the non-local processes depend on the parameters of the ABS (charge and energy), which can be controlled by changing either the chemical potential or the phase difference between superconducting terminals of the JJ. In order to explore those dependencies, we vary ABS gate  $V_{\text{ABS}}$  for fixed  $\Delta\phi = 0$  while recording charge stability diagrams with the bias applied either for the ECT or the CAR configuration. We then extract the magnitude of the maximum correlated current  $\langle I_{\text{corr}} \rangle$ , see section 4.7 for the detailed description. The resulting dependencies are presented in Fig. 4.7(a), while the corresponding ABS spectrum is shown below (c). We observe that when varying  $V_{\text{ABS}}$  we can tune the system across the point of equal ECT and CAR amplitudes, a prerequisite for engineering a two-cite artificial Kitaev chain[12, 82].

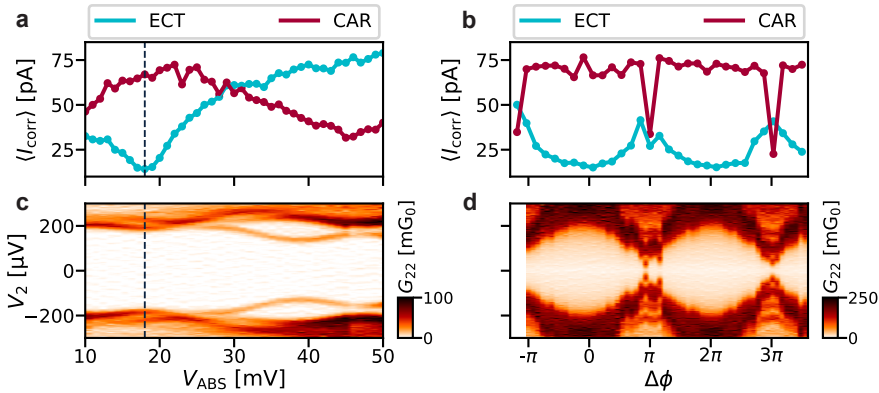


Figure 4.7: Dependence of the ECT and CAR extracted correlated currents ( $\langle I_{\text{corr}} \rangle$ ) as a function of the ABS gate (a) and the phase difference  $\Delta\phi(B_{\perp})$ . Corresponding spectroscopic measurements are shown in the bottom panels. The dashed line indicates the value of the  $V_{\text{ABS}}$  at which plots (b, d) are taken. The phase dependence is predominately concentrated around  $\Delta\phi = (2N + 1)\pi$  values, at which the induced gap is close to zero, and the local transport process is superimposed on the ECT and CAR signals.

Fixing the value of the  $V_{\text{ABS}}$  and using the same protocol for extracting  $\langle I_{\text{corr}} \rangle$ , we explore how the phase difference  $\Delta\phi$  affects ECT and CAR amplitudes. We observe that the

strongest change in the signal occurs around  $\Delta\phi = \pi$ , which agrees with the single ABS model[30]. Qualitatively, it can be explained by the quasiparticle excitation of the ABS approaching character of a single electron ( $u^2 = 1$  or  $v^2 = 1$ ), thus suppressing intrinsically superconducting CAR. Unfortunately, at the same phase  $\Delta\phi$  value, the induced superconducting gap becomes close to zero, allowing for local transport due to the finite bias in the leads. As such, we can only extract the non-local amplitudes by subtracting the local currents.

#### 4.6. APPENDIX: USING QUANTUM DOT AS A SPECTROSCOPY TOOL

4

The range of transport phenomena that can be studied in the device is not limited by the ECT and CAR. In this section, we utilize the quantum dot as a spectroscopic probe of the ABS, while the outer tunnel barrier of the second dot is not energized. Again, we perform measurements using the 3-probe configuration. In contrast to the study of ECT and CAR, we apply bias of  $+300\mu\text{V}$  to the normal contact of the QD1, exceeding the superconducting gap, see Fig. 4.8(a). The second normal contact is kept at zero voltage.

The transport cycle becomes possible when the dot chemical potential level is lowered to the filled ABS excitation, marked with **1**. The dot can accept an electron while the ABS is excited into the doublet state  $|D\rangle$ . To complete the transport cycle, normal lead on the other side can either accept or donate an electron, while the probability of those events is determined by the ABS coherence factors  $u$  and  $v$ . This second part of the cycle results in the non-local current  $I_2$ , see Fig. 4.8(c,f). It is possible to convert the distance  $\Delta V_{\text{PG1}}$  between points **1** and **3** on the dot spectroscopy scan to the energy of the ABS using the fact that  $V_{\text{bias}} - E_{\text{ABS}} = \alpha_1 \cdot \Delta V_{\text{PG1}}$ .

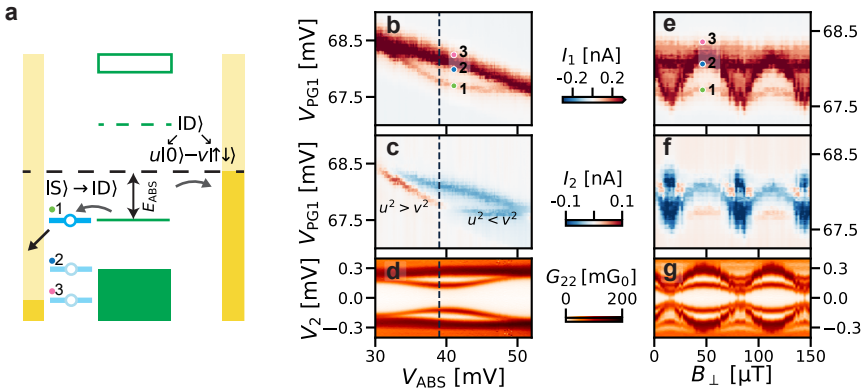


Figure 4.8: (a) Schematic of the transport cycle. The process is possible only between points marked as **1** and **3**, outside of which the QD is in the Coulomb blockade. Plots (d,g) show tunneling spectroscopy measurements using the normal probe. Field scans are taken at the  $V_{\text{ABS}}$  value indicated by the dashed line. Note that the dot spectroscopy plots (b,c,e,f) show the value of current and not a derivative. The absence of current between points **1** and **2** indicates that energy relaxation is absent.

Quantum dot can be used a spin-selective spectroscopy tool[83], which can be explored to study spin-split ABS in a Josephson junction with spin-orbit and Zeeman interactions[84, 85, 86].

#### 4.7. APPENDIX: EXTRACTING ECT AND CAR AMPLITUDES

Here we show a protocol, used to extract  $\langle I_{\text{corr}} \rangle$  in Fig. 4.7. As an example, the charge stability diagram obtained at the phase  $\Delta\phi \approx \pi$  is shown, containing considerable local current.

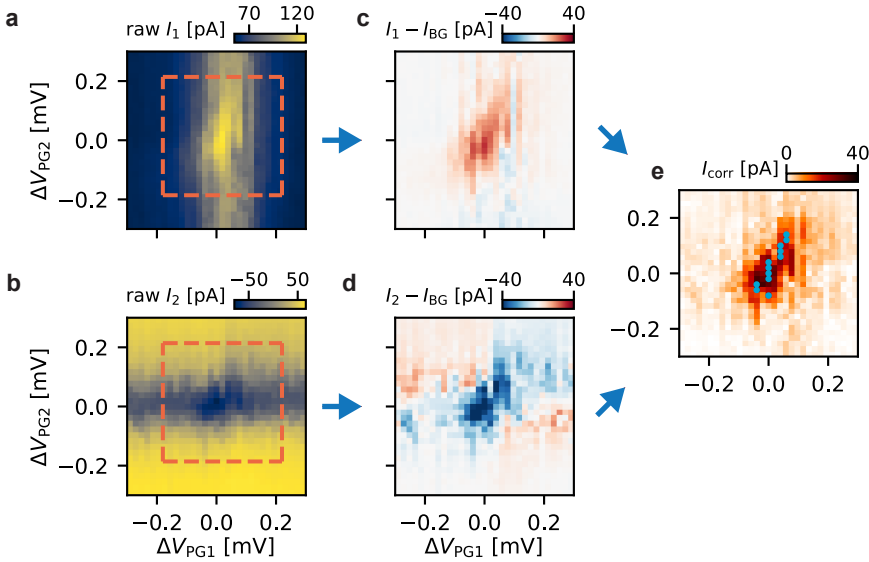


Figure 4.9: Raw current values (a,b) contain contributions from non-local and local processes, as well as the constant instrumental offsets. To separate the values of interest, we first define a region that contains ECT/CAR (dashed orange rectangle), average lines (columns) outside of it and subtract them from the raw signal, obtaining pure non-local component (c,d). We then compute correlated current  $I_{\text{corr}} = \sqrt{(I_1 - I_{\text{BG}}) \cdot (I_2 - I_{\text{BG}})}$  (e). Finally, the value  $\langle I_{\text{corr}} \rangle$  is obtained by averaging points, sampled from each row, for which value exceeds a threshold defined as the 50% of the absolute maximum  $I_{\text{corr}}$ .

#### 4.8. APPENDIX: ADDITIONAL DATA FOR THE FIRST GENERATION DEVICE

Here, we present the data measured on a nominally similar device. The major difference is that the two-step Al etching was not used here, increasing the length of the Josephson junction. We believe that, together with the electrostatic fringing fields imposed by the depletion gates, contribute to the more crowded ABS spectrum with a relatively small induced gap. However, it was still possible to resolve ECT and CAR processes in this device.

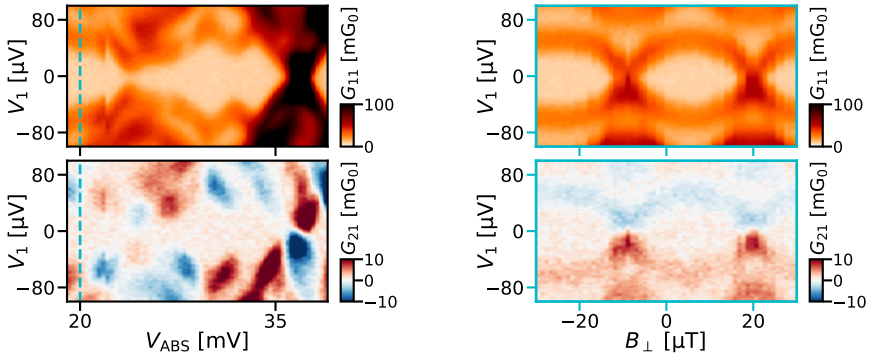


Figure 4.10: Local and non-local spectroscopy as a function of ABS gate and out-of-plane magnetic field for the first generation device. Note a significantly smaller induced superconducting gap compared to the device in the main text.

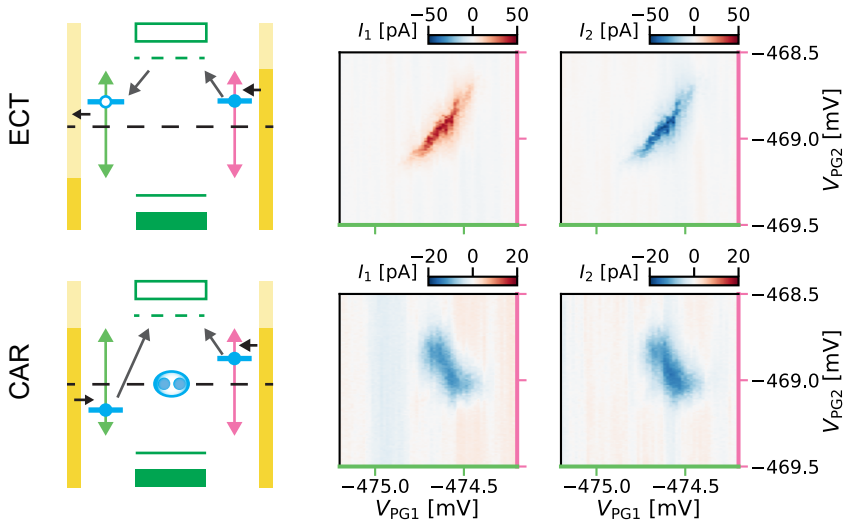


Figure 4.11: Non-local transport processes, measured in the first generation device. Here, the applied bias is  $50 \mu\text{V}$  in magnitude.

# 5

## FLUX-TUNABLE PMM

**Ivan KULESH, Sebastiaan L. D. TEN HAAF, Qingzhen WANG,  
Vincent P.M. SIETSES, Yining ZHANG, Sebastiaan R.  
ROELOFS, Christian G. PROSKO, Di XIAO, Candice THOMAS,  
Michael J. MANFRA, Srijit GOSWAMI**

*In semiconducting-superconducting hybrid devices, Andreev bound states (ABSs) can mediate the coupling between quantum dots (QDs), allowing for the realisation of artificial Kitaev chains. In order to engineer Majorana bound states (MBSs) in these systems one must control the energy of the ABSs. In this work, we show how extended ABSs in a flux tunable Josephson junction can be used to control the coupling between distant quantum dots separated by  $\approx 1 \mu\text{m}$ . In particular, we demonstrate that the combination of electrostatic control and phase control over the ABSs significantly increases the parameter space in which MBSs are observed. Finally, by employing an additional spectroscopic probe in the hybrid region between the QDs, we gain information about the spatial distribution of the Majorana wave function in a two-site Kitaev chain.*

Quantum dots (QDs) with an induced superconducting (SC) coupling can be used to create solid-state quantum entanglers [67, 68, 87, 88, 89], as well as to implement quantum gates for spin-qubits [15, 90]. Moreover, QDs with both a superconducting coupling and hopping interactions offer a platform for constructing an artificial Kitaev chain [7, 11], hosting Majorana bound states (MBSs). The minimal chain is a system of two QDs, which can be tuned to host so-called poor man's Majoranas (PMM) [12, 33]. While not topologically protected from perturbations, these states are expected to have Majorana properties, such as non-Abelian exchange statistics [91, 92]. A crucial prerequisite to implement a PMM is the ability to control the coupling between spin-polarized QDs. It was demonstrated that a proximitized semiconducting-superconducting hybrid region, hosting Andreev bound states (ABS), is an excellent mediator to couple the QDs [31, 32, 38, 93]. The nature and magnitude of this coupling can be tuned by changing the electrostatic potential of the hybrid region, as well as by changing the orientation of the external magnetic field [32, 38]. Both were recently explored in experiments demonstrating the realization of the PMM states [36, 82].

5

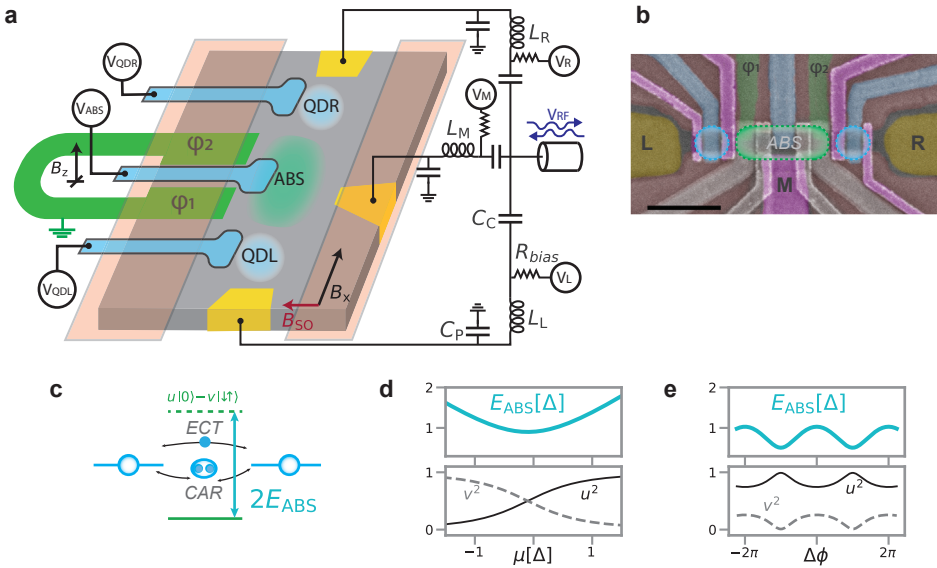


Figure 5.1: Schematic of the device measured (a) and false-colored SEM image (b): a grounded superconducting loop (green) is used to create a phase difference between two terminals  $\phi_1$  and  $\phi_2$ , extending into the ABS region in a one-dimensional channel, formed by two depletion gates (red). Plunger gates (blue) are used to control QDs and ABS chemical potential. Three normal spectroscopic terminals (yellow) are connected to resonators, formed by off-chip coil inductors  $L_X$  and the parasitic capacitances of bondwires  $C_P$ , with coupling capacitors  $C_C$  allowing for a multiplexed read-out. Cutter gates (pink, shown only in (b)) are used to confine quantum dots and define tunnel barriers. The scale bar in (b) is 500 nm. The experiment is shown schematically in (c): ABS (green) mediates ECT and CAR between quantum dots. The amplitudes of those non-local processes depend on the ABS energy  $E_{\text{ABS}}$  and its coherence factors  $u$  and  $v$ , which, in turn, can be controlled by either the ABS chemical potential  $\mu$  (d) or the phase difference  $\Delta\phi$  (e).

Here, we further explore the role of ABSs in realizing PMM states by exploiting a novel

geometry in a two-dimensional electron gas (2DEG) hybrid system. Motivated by recent theory work [30], we utilize ABSs coupled to two SC electrodes embedded in a loop, such that the phase difference between the electrodes can be controlled with an applied perpendicular magnetic field. Taking advantage of the long coherence length of the 2DEG, we are able to couple QDs separated by about  $1\ \mu\text{m}$ . We observe that the superconducting phase difference changes the effective coupling between two QDs and allows for finding PMM sweet spots within a continuous range of the ABS chemical potential. This is an improvement on systems without this phase control, where sweet spots arise only at two discrete points of the ABSs chemical potential [31, 32]. Despite the relatively large separation of the two QDs, an induced inter-dot coupling on the order of  $10\text{-}30\ \mu\text{eV}$  is extracted from the spectroscopic measurements. This demonstrates a clear advantage of using ABSs in proximitized semiconductors for providing a long-range coupling between QDs and relaxes spatial restrictions on PMM-device design. Lastly, exploiting the flexible 2DEG architecture, we utilize a spectroscopic probe connected to the proximitized ABS segment. This additional probe allows us to study the spatial distribution of the PMM wavefunctions in the strongly coupled regime [34].

## 5.1. DEVICE DESIGN & CHARACTERIZATION

The device is implemented on an InSbAs two-dimensional electron gas capped with 7 nm epitaxial aluminum [40]. Operating in depletion mode, the first layer of gates (red, Fig. 5.1 a,b) define a one-dimensional channel connected to three spectroscopy terminals (yellow). Voltages are applied to the plunger gates (blue), with  $V_{\text{QDL}}$  and  $V_{\text{QDR}}$  tuning the respective QDs chemical potentials, while  $V_{\text{ABS}}$  controls the chemical potential of the hybrid region. The plunger gates and the tunnel (purple) gates are situated in the second and third layers.

Two superconducting terminals (green) are connected in a loop and protrude into the channel, establishing an extended proximitized region hosting ABS. The superconducting loop is kept grounded, so that an out-of-plane field  $B_z$  controls the phase difference  $\Delta\phi = \phi_2 - \phi_1$  between the two SC electrodes. Measurements are performed using sub-GHz off-chip resonators, which are connected to the corresponding tunnel probes (see supplementary information SI for schematics). The resonators can be probed simultaneously using a multiplexed reflectometry setup [64]. The complex reflected RF signal of each resonator is converted to the single real value  $\tilde{V}_{\text{RF}}^X$  by performing a rotation in the complex plane (SI). This signal is representative of the device conductance [62, 63, 94]. Each resonator is connected to a bias-tee  $R_{\text{bias}}$ , allowing for applying a bias voltage to each spectroscopic normal lead, as well as for measuring the currents through them. This allows to additionally extract the device conductance  $G_{xx} = dV_x/dI_x$  using a standard low-frequency lock-in technique. The measurements are performed in a dilution refrigerator with the base temperature of 20 mK.

The QDs are coupled by a hopping interaction through elastic co-tunneling (ECT) and by a pairing interaction arising from crossed Andreev reflection (CAR), schematically illustrated in Fig. 5.1c. The amplitudes of these non-local processes both depend on the ABS energy  $E_{\text{ABS}}$  [31]. Additionally, ECT and CAR respond differently to the charge character of the ABS (determined by the coherence factors  $u$  and  $v$ ). Thus, when varying

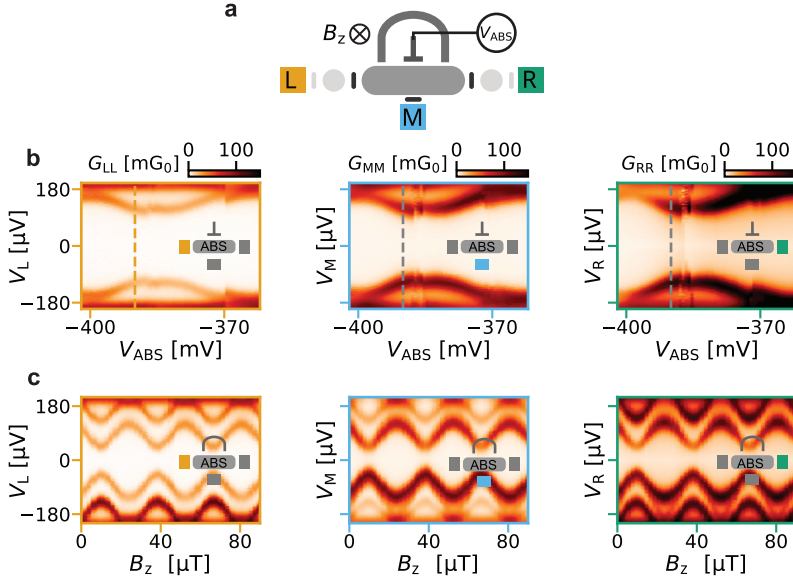


Figure 5.2: Schematic of the device with three tunneling spectroscopy terminals used to probe an extended ABS (a). The four outermost gates, used for forming the quantum dots, are not energized. Top panel (b): tunneling spectroscopy measurements acquired while varying the ABS chemical potential. Bottom panel (c): tunneling spectroscopy measurements, varying the out-of-plane field threading the SC loop, at the  $V_{ABS}$  value indicated by the dashed line in (b). For both panels we plot conductance  $G_{XX} = dV_X/dI_X$ . The periodicity in field ( $28 \mu T$ ) agrees well with the loop area ( $60 \mu m^2$ ). Both measurements are performed at zero in-plane magnetic field.

the ABS parameters with either the chemical potential  $\mu$  or the phase  $\Delta\phi$  (schematically illustrated in Fig. 5.1d,e), one expects to control the ECT to CAR ratio [30].

To mediate ECT and CAR between the distant QDs, an ABS is required that extends throughout the entire hybrid region in between them. We first establish the presence of such an extended state in this device, particularly considering the relatively large length of this region (700 nm). This is achieved by performing tunneling spectroscopy measurements from three sides (left, middle and right), while the four outermost barriers used for forming quantum dots are not energized (Fig. 5.2a). We separately vary either the ABS chemical potential by changing the voltage  $V_{ABS}$ , or the phase  $\Delta\phi$  by applying a magnetic field  $B_z$ . We observe that the spectrum shows correlated dependence from all three terminals, both as a function of gate voltage (Fig. 5.2b) and magnetic field (Fig. 5.2c), implying that a single quantum state is accessible to both quantum dots.

## 5.2. TUNING INTO PMM REGIME

Having established the presence of extended ABSs in our device, we proceed with forming the PMM system. First, we energize the additional outermost gates to define the QDs. An in-plane magnetic field  $B_x = 150 mT$  is applied, in order to spin-polarize the QDs. To achieve strong coupling between the QDs, the innermost gates are set to have

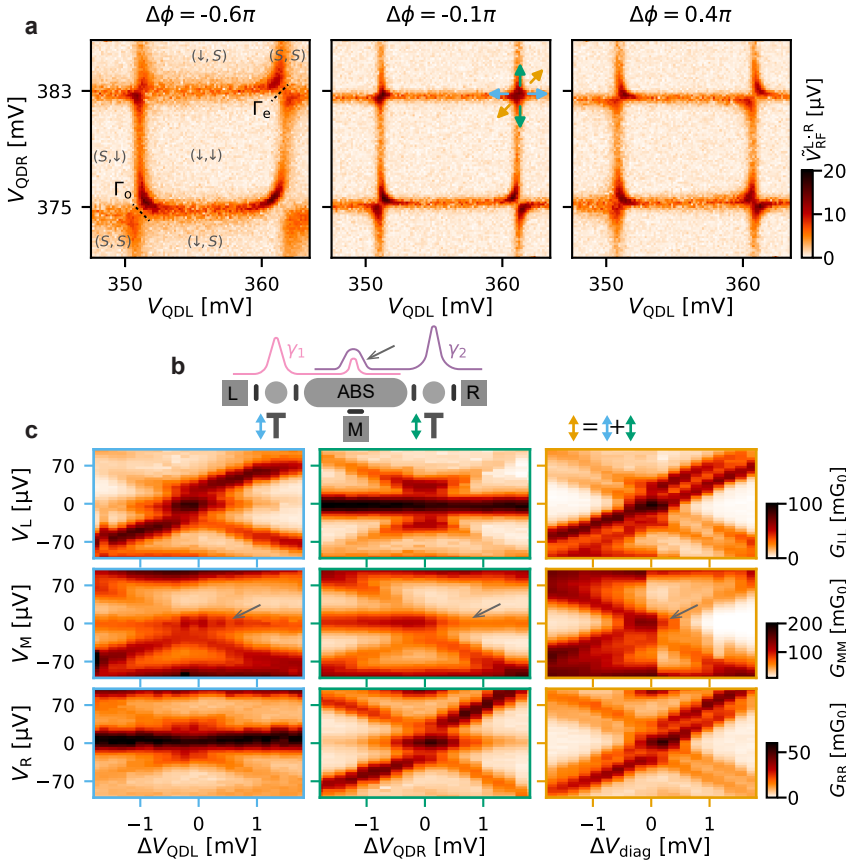


Figure 5.3: Tuning into the PMM sweet spot and verifying the PMM spectrum. Top panel (a): charge stability diagrams, shown in correlated voltage  $\tilde{V}_{RF}^{L,R} = \sqrt{\tilde{V}_{RF}^L \cdot \tilde{V}_{RF}^R}$  (each component measured from the Coulomb blockade SI), varying the superconducting phase difference  $\Delta\phi$  ( $B_z$ ). Combined QD states are indicated in brackets. States, coupled by  $\Gamma_o$  ( $\Gamma_e$ ) are connected with the dashed lines. (b): Schematic of the detuning experiment, showing PMM wave-functions  $\gamma_1$  and  $\gamma_2$ , which can reside partially in the ABS region. (c): tunneling spectroscopy, measured from all three probes, plotted in conductance  $G_{XX}$ . Note the signal at zero bias measured at the middle probe, highlighted with the arrows.

relative high tunneling between the QDs and the hybrid region [34, 35]. In this regime, the QDs are commonly described as Yu-Shiba-Rusinov (YSR) states [95, 96, 97, 98, 99], as observed in spectroscopy measurements SI. Depending on the dot chemical potential, the ground state of each QD is either a  $|\downarrow\rangle$  doublet or a singlet  $|S\rangle$  superposition of the empty and double-occupied QD state. With this description of the QD states, the simple picture of ECT and CAR interactions can be extended. Considering the combined state of the two QDs, two types of effective interactions can be defined [34, 36]: spin-conserving  $\Gamma_o$ , coupling  $|S, \downarrow\rangle$  with  $|\downarrow, S\rangle$ , and spin non-conserving  $\Gamma_e$  which couples  $|\downarrow, \downarrow\rangle$  with  $|S, S\rangle$ , see Fig.5.3a. Notably, those quantities can be expressed via ECT and CAR amplitudes  $t$

and  $\Delta$ . Thus,  $\Gamma_o$  is a linear combination of spin-conserving terms  $t_{\uparrow\downarrow}, t_{\uparrow\uparrow}, \Delta_{\uparrow\downarrow}, \Delta_{\uparrow\uparrow}$  (note that the CAR couples opposite spins), while  $\Gamma_e$  can be expressed via spin-flipping terms  $t_{\uparrow\downarrow}, t_{\downarrow\uparrow}, \Delta_{\uparrow\downarrow}, \Delta_{\downarrow\uparrow}$ . Without the spin-orbit interaction present, or when the external magnetic field is applied alongside the spin-orbit field  $B_{SO}$ , only  $\Gamma_o$  is significant. Therefore, we apply the in-plane magnetic field alongside the dot-dot axis, perpendicular to the direction of the  $B_{SO}$ , see SI.

The different types of couplings between the QDs are revealed in charge stability diagrams (CSD), obtained by sweeping the QD plunger voltages and measuring reflected RF signals from the left and right normal leads, Fig.5.3a. We record the CSDs while varying  $B_z$ , which can be converted to the phase difference  $\Delta\phi$  across SC electrodes (we assign  $\Delta\phi = 0$  to the point of maximum  $E_{ABS}$  SI). Measured avoided crossings demonstrate the  $\Gamma_o$  ( $\Gamma_e$ ) coupling dominating, depending on whether the avoided crossing is (anti-)diagonal. In this example, we observe that varying  $\Delta\phi$  indeed can change the coupling regime from  $\Gamma_e > \Gamma_o$  to  $\Gamma_e < \Gamma_o$  for the top-right transition, with the modulation being  $2\pi$ -periodic in  $\Delta\phi$  SI. This ability to change the coupling regime with the phase difference originates from the fact that  $\Delta\phi$  affects the ABS coherence factors  $u$  and  $v$  (Fig.5.1), contributing in a different manner to ECT and CAR [30, 31], and, consequently, to  $\Gamma_e$  and  $\Gamma_o$ . Moreover, the presence of Zeeman field and the spin-orbit interaction in the proximitized region further affects the interplay between  $\Delta\phi$  and the spin-split ABS spectrum [84, 85, 86], additionally affecting the spin-conserving(-flipping) ECT  $t_{\sigma_1\sigma_2}$  and CAR  $\Delta_{\sigma_1\sigma_2}$  amplitudes [32].

The point of  $\Gamma_e = \Gamma_o$  corresponds to the so-called PMM sweet spot [34, 36], with the dot transitions crossing in straight lines. We proceed to verify the sweet spot conditions by performing the spectroscopy measurements (Fig.5.3b,c) while detuning either one or both QDs. As expected [12], the zero-bias conductance peak persists when detuning only one QD and splits from zero energy when detuning both QDs. The minimum energy of the excited states allows for estimating the coupling amplitudes to be on the order of  $18\mu\text{V}$  (and up to  $30\mu\text{V}$  for the regime described in SI). This is comparable to previously reported values [35, 36], indicating that the increased length of the ABS segment does not significantly impact the interaction strength. Operating in the strong coupling regime, a finite overlap of the PMM wave functions inside the ABS segment is expected [30, 34] but has not yet been directly probed. Leveraging the flexibility of the 2DEG platform, we utilize the spectroscopic probe of the ABS region to study this. As shown in Fig.5.3c, we find that a zero-bias conductance peak is also clearly visible in the conductance  $G_{MM}$ . This is an indication that the PMM wave functions  $\gamma_1$  and  $\gamma_2$  both reside partially in the ABS region, such that electron transfer from the lead M to the delocalized zero-energy fermionic mode is possible.

It is important to note that the observed wave function overlap in the ABS region is not detrimental for the device performance. In contrast, the outer QDs must support only a single PMM wave function to ensure optimal conditions to explore the MBS physics [30, 34, 92].

### 5.3. EXPLORING GATE-PHASE PARAMETER SPACE

The section above demonstrates that the relative amplitudes of  $\Gamma_e$  and  $\Gamma_o$  couplings can be accurately controlled through controlling the superconducting phase difference. Now, we proceed to explore how this can be used to compliment the previously established control utilising the ABS chemical potential [32, 38, 82]. As with phase, this tunability is achieved through the dependence of the ABS energy  $E_{\text{ABS}}$ , as well as the coherence factors  $u$  and  $v$ , on ABS gate voltage [31]. Moreover, one expects that the dependence of the ABS parameters on the phase difference  $\Delta\phi$  is modified when varying the ABS chemical potential  $\mu$  [30]. Qualitatively this can be seen as the junction transparency being a function of  $\mu$ . This further motivates us to explore the two-dimensional  $V_{\text{ABS}}, \Delta\phi$  parameter space.

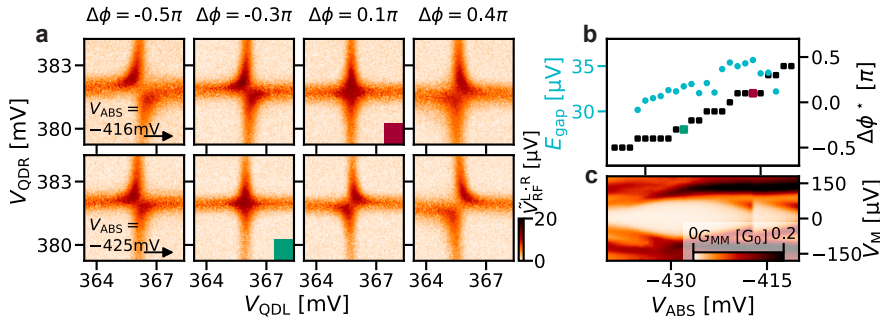


Figure 5.4: The sweet spot location in the ABS gate - SC phase difference space. We capture charge stability diagrams (a) for a set of fixed  $V_{\text{ABS}}$  voltages while varying  $\Delta\phi$ . The sweet spot  $\Delta\phi^*$  is then determined for each  $V_{\text{ABS}}$  as a crossover between  $\Gamma_o$  and  $\Gamma_e$ , corresponding to the straight QD charge transition lines, and marked with a colored square. We repeat this procedure for multiple  $V_{\text{ABS}}$  values and plot the extracted  $\Delta\phi^*$  alongside the excitation gap, determined from the spectroscopic measurements, in (b). ABS spectrum as a function of the ABS gate, measured with the dots detuned, shown in (c).

The results of this experiment are summarized in Fig. 5.4. We record CSDs, zoomed-in on a specific transition (corresponding to the top-right on the Fig. 5.3a), while varying  $\Delta\phi(B_z)$ . Comparing CSDs at different  $V_{\text{ABS}}$ , we observe that the position of the PMM sweet spot, corresponding to the crossover between dominant  $\Gamma_e$  to  $\Gamma_o$ , is achieved at the different  $\Delta\phi^*$  (SI provides additional measurements of the field detuning spectrum). Moreover, small changes in the  $V_{\text{ABS}}$  result in a small change of the sweet spot phase difference  $\Delta\phi^*$ . This demonstrates that for certain  $\Delta\phi, V_{\text{ABS}}$  range, the PMM sweet spot spans a continuous line in a two-dimensional space instead of being a single point at a specific gate (phase) value. It is possible that the sweet spot characteristics, such as the excitation gap, change alongside  $\Gamma_e = \Gamma_o$  line in the  $\Delta\phi, V_{\text{ABS}}$  plane. However, we haven't observed any systematic behavior, exploring multiple regimes throughout several device cool-downs (see SI). This discrepancy with the theoretical predictions [30] can be attributed to the presence of multiple states in the proximitized region (Fig. 5.2c), as well as the spin-splitting of said states.

## 5.4. CONCLUSIONS

We have demonstrated the possibility of strongly coupling two QDs via an extended Andreev bound state in a proximitized InSbAs 2DEG on a 700 nm-long hybrid segment. Obtained coupling amplitudes are on the same order of magnitude as reported in preceding studies with short hybrid segments, thus relaxing constraints for future designs. We found that embedding the hybrid region in a SC loop allows for a novel control knob over the effective ECT and CAR couplings between the two QDs with the superconducting phase difference. Our design can be of interest for realizing a long-range tunable superconducting coupling for spin-qubit architectures [15]. Here, we explored the phase control to tune the system to a set of sweet spots hosting PMM states. Combined with control through the ABS chemical potential established in previous works, we found that sweet spots can be obtained along a continuous path in the gate-phase space. Future studies can benefit from dedicated flux lines to control the interaction between QDs, which may reduce gate cross-coupling and enhance charge stability when compared with the electrostatic gate control. Lastly, we studied the PMM wave functions in the ABS segment and observed their presence in tunneling spectroscopy, suggesting the states are not fully localized on the QDs. These results expand the device geometry and support the understanding of coupled quantum dots in a PMM system.

## 5.5. SUPPLEMENTARY

### 5.5.1. DEVICE FABRICATION

All devices were fabricated using techniques similar to [40]. An aluminum ring with two narrow extended strips is defined in an InSbAs-Al chip by wet etching, followed by the deposition of three normal Ti/Pd contacts. After placing 20 nm AlO<sub>x</sub> via atomic layer deposition (ALD), three Ti/Pd depletion gates are evaporated. Following a second ALD layer (20 nm AlO<sub>x</sub>), multiple Ti/Pd finger gates are evaporated. In a similar fashion, we define a third layer of gates. Finger gates in the second and third layers are used to define the barriers and tune the chemical potentials. The depletion gates define a quasi-1D channel with a width of about 150 nm, contacted on each side and in the middle by a normal lead. The aluminum ring extends into the channel and induces superconductivity in the ABS section of the device, with an induced gap on the order of 200 μeV. ABSs are found to be present over a large range of  $V_{\text{ABS}}$ , the voltage applied to the gate covering the hybrid region. Finger gates define QDs with charging energies 1 mV order of magnitude.

A single device was used to obtain the data presented in the main text. Measurements were performed in a dilution refrigerator with a base temperature of 20 mK. The main text contains information from a single cool-down, while the supplementary contains additional datasets from the preceding cool-down (5.12,5.13).

### 5.5.2. TRANSPORT MEASUREMENTS AND DATA PROCESSING

Measurements are performed using sub-GHz off-chip resonators connected to the corresponding tunnel probes. Each resonator circuit is formed by the spiral superconducting inductor and a parasitic capacitance of the bond wire. The resonators can be probed simultaneously using multiplexed reflectometry setup[64], with frequencies  $f_{L,M,R} = 723, 505, 248$  MHz, determined by the variation in the inductances

$L_{L,M,R} = 0.2, 0.5, 1.5 \mu\text{H}$ . We convert the complex reflected RF signal of each resonator to the single real value  $\tilde{V}_{RF}^X$  performing rotation in the complex plane, see 5.6. This signal is expected to be linear in conductance, expressing the same features [62, 63, 94]. To fully benefit from the increased acquisition speed, we use the rastering method, 5.5, with an arbitrary waveform generator (AWG) applying a two-channel sawtooth signal to the dot plunger gates. The first channel has a single wave period, while the second channel has as many periods  $N_2$  as the number of rows in the resulting charge stability diagram. The frequency  $f_B$  of the fast channel is limited by the RC filter cut-off frequency. The number of points in each row  $N_1$  is limited by the acquisition device memory  $N_1 \cdot N_2$  and the acquisition bandwidth  $f_B \cdot N_1 < BW$ . Sawtooth signals from the AWG are connected to the optical isolator, breaking any potential ground loops, and are combined with the constant DC offsets using a voltage divider. They are then fed into the device through a set of filtered low-frequency fridge lines.

On the AWG trigger event, the VNA records  $N_1 \cdot N_2$  points such that the total acquisition time equals the period  $T_A$  of the slow channel wave. The VNA measures the complex reflected signal amplitude, with the RF circuit designed so that the incident and reflected from the resonator waves are separated into two lines with the help of a directional coupler. Finally, the output one-dimensional data string from the VNA is mapped into a two-dimensional matrix corresponding to the charge stability diagram.

Each resonator is connected to the bias-tee  $R_{bias}$ , thus allowing the application of a bias voltage to each spectroscopic normal lead, as well as measuring the current flowing through it. This allows to extract device conductance  $G_{xx}$  using standard low-frequency lock-in technique. We assume total line resistances to be order of  $10 \text{ k}\Omega$ , and neglect voltage divider effect, which for currents  $I_x < 1 \text{ nA}$  results in  $< 10 \mu\text{V}$  voltage offsets.

Instrumental offsets of the applied voltage biases are corrected by independently calibrating the spectroscopic measurements on each side. When applying a DC voltage to the specific tunnel probe, the other probes are kept at the offset voltage value.

Magnetic fields were applied using a 3D vector magnet.

Due to device instabilities or charge jumps, electrostatics of the QDs experience small drifts over the course of the measurements. Investigated orbitals were tracked while collecting the presented datasets. Such drifts are the cause of small discrepancies in gate voltages between figures from the same dataset.

### 5.5.3. SUPPLEMENTARY FIGURES



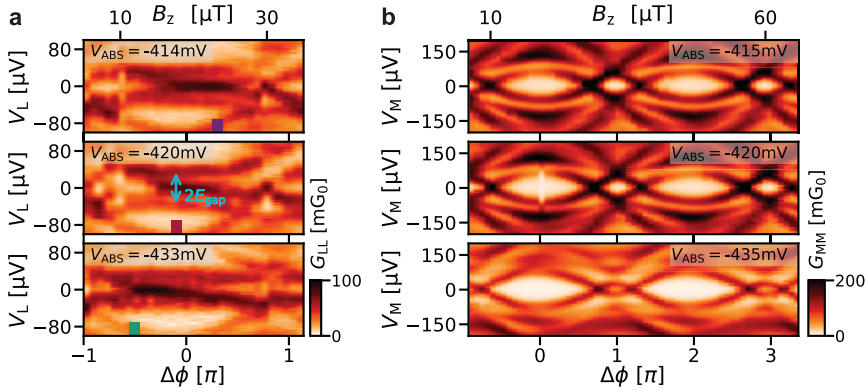


Figure 5.7: Tunneling spectroscopy of the PMM system around a sweet spot (a), measured from the left terminal. When detuning the phase difference  $\Delta\phi$ , we observe the splitting of the zero-bias peak, as the sweet spot exists only for the specific value  $\Delta\phi^*$ . For each  $\Delta\phi$  point, quantum dot chemical potentials are adjusted to stay at the charge degeneracy point. Changing the ABS chemical potential with the  $V_{\text{ABS}}$  gate shifts the sweet spot position, as shown in the main text. To gain further insight into the relation between the sweet spot location and the system parameters, we record the ABS spectrum with the quantum dots in the Coulomb blockade as a function of the phase difference (b).

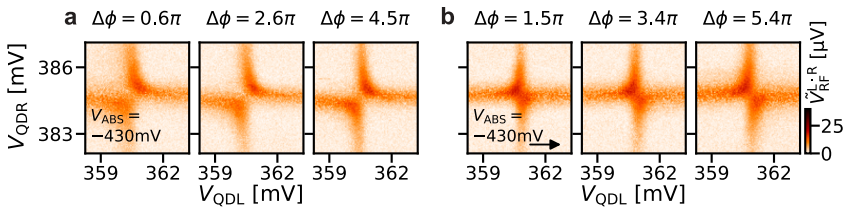


Figure 5.8: As the phase modulation of the ABS parameters is  $2\pi$ -periodic, we expect the same periodicity for the quantum dots interaction type and strength. To verify this, we record charge stability diagrams in a large  $\Delta\phi$  range. Charge stability diagrams, shown for two different starting phase values (a, b), confirm the expected behavior.

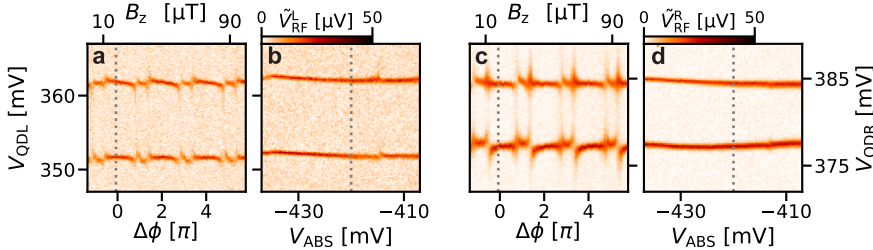


Figure 5.9: ABS not only acts as an interaction mediator between two quantum dots but also couples to an individual QD, modifying energy levels. ABS-QD coupling is revealed in the Coulomb peak shift as a function of the phase difference (a for QDL and c for QDR) and the ABS gate (b,d for QDL and QDR respectively). Avoided crossings are present when the ABS energy approaches zero and are clearly visible when sweeping  $\Delta\phi$ .

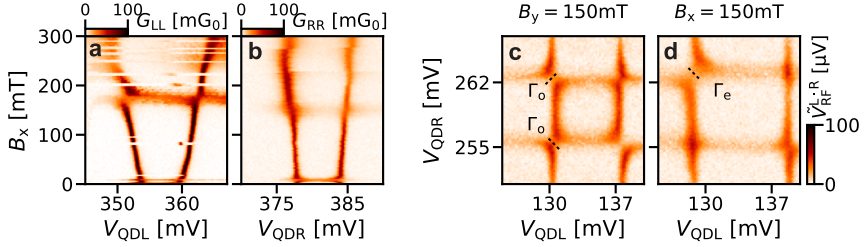


Figure 5.10: Coulomb peak evolution with the in-plane magnetic field (a, b) shows a clear Zeeman splitting, necessary for the quantum dot levels spin polarization. Depending on the in-plane field angle with respect to the spin-orbit field, charge stability diagrams demonstrate either only spin-conserving interaction  $\Gamma_o$  is allowed (c,  $B_{SO} \parallel B_Y$ ), or, additionally, spin non-conserving  $\Gamma_e$  (d,  $B_{SO} \perp B_X$ ).

5

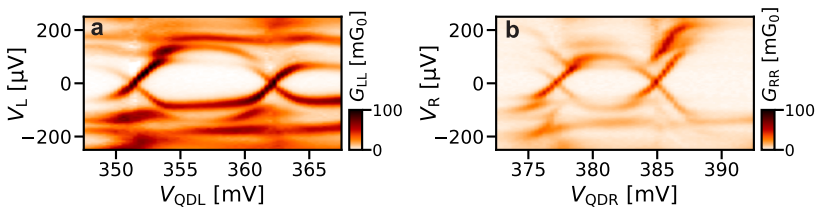


Figure 5.11: Tunneling spectroscopy of YSR states in the left quantum dot (a) demonstrates a strong coupling to the ABS. Thusly, the QDL ground state as either a singlet  $|S\rangle = u_L|0\rangle - v_L|\downarrow\downarrow\rangle$ , or a doublet  $|\downarrow\rangle$ . Tunneling spectroscopy of the right QD (b) shows a similar behavior.

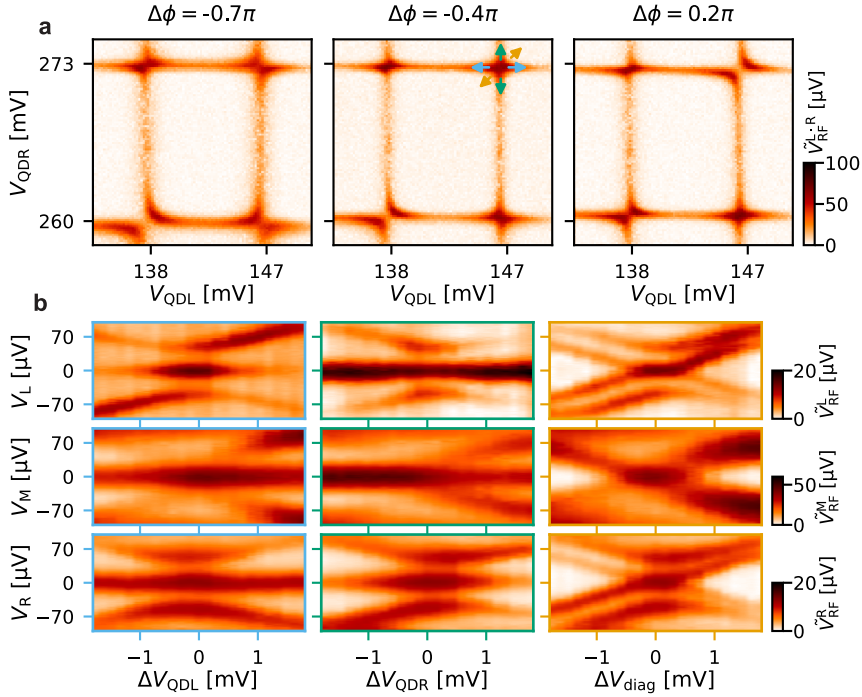


Figure 5.12: Additional data for device cool-down II, demonstrating tuning into a sweet spot with magnetic flux, shown with the charge stability diagrams while varying  $\Delta\phi$  (a). We verify the PMM sweet spot conditions with the tunneling spectroscopy measurements from all three probes while detuning quantum dot plunger gates (b).

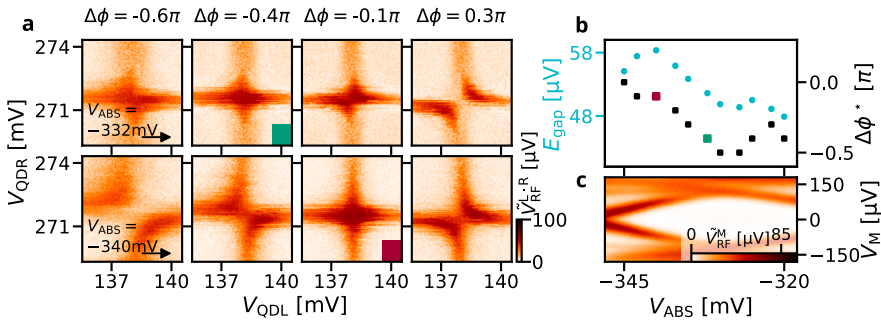


Figure 5.13: Sweet spot location in the  $\Delta\phi - V_{ABS}$  parameter space for device cool-down II. The sweet spot phase difference  $\Delta\phi^*$  is found by inspecting charge stability diagrams (a) while varying  $\Delta\phi$  for a fixed  $V_{ABS}$  gate value and corresponds to the transition between dominant  $\Gamma_o$  and  $\Gamma_e$  (marked with a colored square). The same protocol is repeated for a range of  $V_{ABS}$  values with the extracted  $\Delta\phi^*$ , as well as the excitation gap in the sweet spot  $E_{gap}$ , shown in (b). Corresponding ABS spectrum at  $\Delta\phi = 0$  as a function of  $V_{ABS}$  measured with the quantum dots in the Coulomb blockade is shown in (c).



# 6

## GATE AND CHARGE SENSING OF PMM DEVICES

**Ivan KULESH, Sebastiaan L. D. TEN HAAF, Yining ZHANG,  
Christian G. PROSKO, Tijn DEGROOTE, Eoin M. MULLALLY,  
Wietze D. HUISMAN**

*I think we agree, the past is over.*

George W. Bush

*This chapter explores PMM characterization methods that do not rely on transport through normal leads. We observe that the dispersive gate sensing signal contains information about non-local processes in a system of two quantum dots coupled through an Andreev bound state. Moreover, we measure the signal originating from the system being in both parity states and study the effect of normal leads on the quasiparticle poisoning and relaxation. Lastly, we present the preliminary results on charge sensing of an ABS using a single-lead QD sensor.*

## 6.1. INTRODUCTION

In the previous chapters, we have seen how the transport measurements can be used to characterize systems of quantum dots coupled through an Andreev bound state. However, probing the non-Abelian statistics and creating a Majorana qubit requires control over the parity of the system[91, 92], prohibiting the use of normal tunneling probes. As such, alternative measurement techniques have to be adapted, which do not require electron transport into the PMM system. In this chapter, we explore quantum capacitance  $C_q$  measurements of a poor man's Majorana (PMM) device, see Fig. 6.1, using multiplexed sub-GHz off-chip resonators.

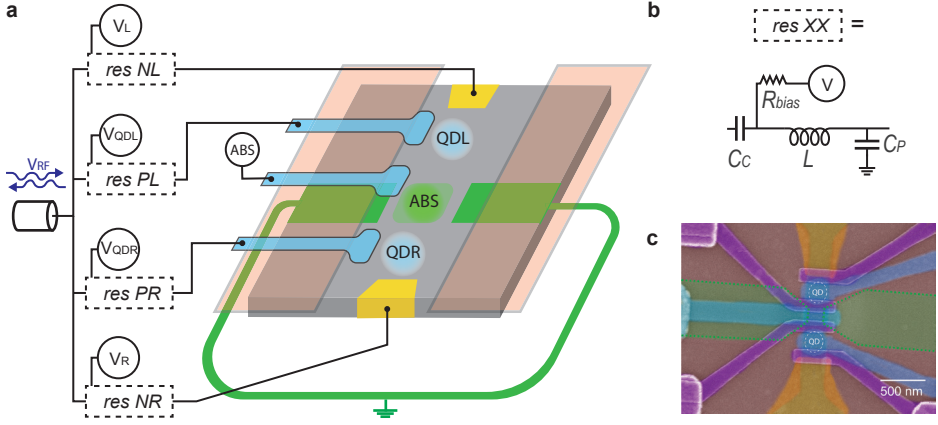


Figure 6.1: Schematic of the device and measurement circuit (a,b) alongside the SEM micrograph (c) of the device similar to the one measured. Multiplexed off-chip resonators, formed by the inductance  $L$  and the parasitic capacitance  $C_p$ , are connected to the QDs plunger gates (blue), as well as to the normal terminals (yellow). A one-dimensional channel is formed between depletion gates (red), while the tunnel gates (purple, c) define QDs and the ABS.

When considering a resonator connected to a plunger gate of a quantum dot, one has to account for the additional capacitance contribution[53, 100, 101], originating from the voltage-driven change in the dot electron occupation. Considering the resonator as a classical circuit, the relevant quantities affecting its load are gate voltage  $V_G$  and the current  $dq_2/dt$ , where  $q_2$  is the charge on the gate capacitor  $C_G$ , see Fig. 6.2. For convenience, we denote all capacitors between the QD and the ground as  $C_{rest} = C_\Sigma - C_G$ . Expressing the unknown charge  $q_1$  on this capacitor in terms of  $q_2$  and the expectation of the total QD charge  $\langle n \rangle$ , we can obtain the expression relating  $V_G$  and  $q_2$ .

So far, there was nothing "quantum" in the above reasoning. To continue, we will assume that the change in  $\langle n \rangle$  arises exclusively from the change in the ground state wave function. Doing this disregards dissipative effects when the probability distribution of occupation of different quantum states changes due to the microwave drive. In this limit,  $\langle n \rangle$  depends exclusively on the gate voltage and has no explicit time dependence. In other words, the charge on the capacitor (and QD) follows the gate voltage without any delay and thus can be represented as a purely reactive load capacitor:

$$\frac{dq_2}{dt} \Big|_{\langle n \rangle(V_G, \dot{V}_G)} = \frac{\delta q_2}{\delta V_G} \frac{dV_G}{dt} \equiv C_{\text{load}} \frac{dV_G}{dt}, \quad C_{\text{load}} = \underbrace{\alpha C_{\text{rest}}}_{C_{\text{geom}}} + \underbrace{\alpha |e| \frac{\delta \langle n \rangle}{\delta V_G}}_{C_q}, \quad \alpha = \frac{C_G}{C_\Sigma}, \quad (6.1)$$

The load capacitance consists of two parts, the geometric contribution  $C_{\text{geom}}$  and the additional *positive* quantum capacitance term  $C_q$ , present when the charge can be redistributed from the dot. Note that in contrast to a single capacitor with a finite density of states [102], the quantum capacitance contribution for a charge island is positive.

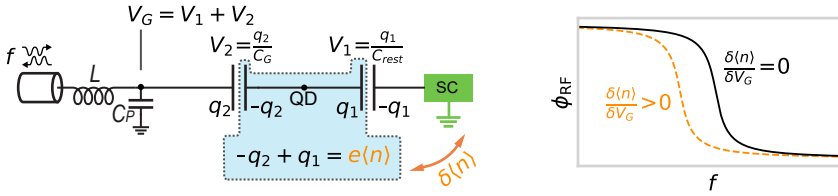


Figure 6.2: A simple electrostatic model of a quantum dot allows one to relate the relevant as seen from the  $LC$ -resonator quantities - the charge  $q_2$  on the gate capacitor  $C_G$  and the gate voltage  $V_G$ . When the gate voltage changes the charge expectation  $\langle n \rangle$ , load capacitance increases, reducing the resonance frequency, as observed in the phase response.

The quantum capacitance correction shifts the resonance frequency, as

$$f_{\text{res}} = 1/2\pi \sqrt{L(C_P + C_{\text{geom}} + C_q)}, \quad f_{\text{res}}^0 = 1/2\pi \sqrt{L(C_P + C_{\text{geom}})} \quad (6.2)$$

We characterize the plunger resonator response at the fixed frequency  $f_{\text{res}}^0$ , with the phase shift  $\tilde{\phi}_{\text{RF}}^{\text{PX}}$  linear in the quantum capacitance[53], such that  $\tilde{\phi}_{\text{RF}}^{\text{PX}} \equiv \Delta \arg \Gamma \propto -1 \cdot C_q$ .

## 6.2. GATE SENSING IN SEMI-ISOLATED SYSTEM: COMPARISON WITH CONDUCTANCE

Firstly, we compare the quantum capacitance signal, corresponding to the phase shift  $\tilde{\phi}_{\text{RF}}^{\text{PX}}$ , to the lead reflectometry measurements of the paired dot, which we characterize with the magnitude  $\tilde{V}_{\text{RF}}^{\text{NX}}$  of the complex reflected signal change. Notably, the dot being probed with the gate resonator is isolated from the corresponding normal lead, such that the dot-lead transition does not contribute to the plunger resonator signal, see schematics in Fig. 6.3(a,c).

We observe that the quantum capacitance signal is present exactly at the avoided crossings of the opposing quantum dot lead transitions, which in turn are characterized by the increased dissipative load on the lead resonator due to conductance signal and the Sisypus resistance[103]. Dominant elastic co-tunneling interaction couples charge state with the total charge being equal, such as  $(0, 2) \leftrightarrow (1, 1)$  in Fig. 6.3(b, ECT), with the dot occupations defined up to an arbitrary even number. Varying the ABS chemical potential with the gate  $V_{\text{ABS}}$ , the dominant interaction type can be changed[31, 32]

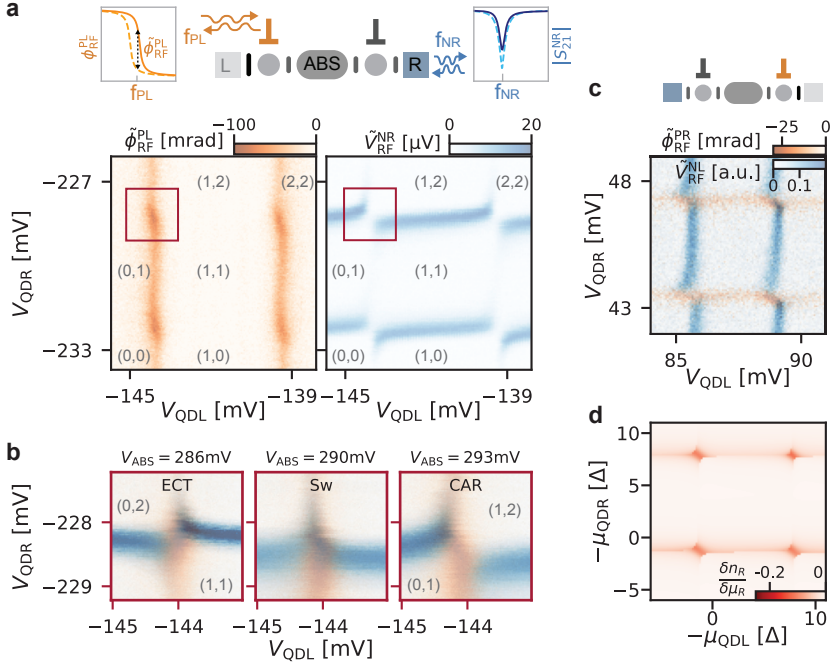


Figure 6.3: Comparing quantum capacitance signal, characterized by the phase shift  $\phi_{RF}^{PX}$  at a fixed frequency, to the lead reflectometry of the opposite QD, plotted as the magnitude of the reflected voltage. Panel (b) shows superimposed signal zoom-in of the top left transition when the dominant interaction between QDs changes from ECT to CAR. In (d), we show results of the numerically simulated charge derivative proportional to the corresponding quantum capacitance. Note the non-zero signal presence alongside the entire line of QD charge degeneracy point as a result of charge transfer between the QD and the ABS.

to the crossed Andreev reflection, Fig. 6.3(b), CAR), with QDs states coupled by emitting/absorbing a Cooper pair into the grounded superconductor. The crossover point corresponds to the PMM sweet spot[12, 82] (Sw).

Notably, the quantum capacitance signal is present away from the opposing dot transition. This indicates that the charge from the gate-sensed QD is redistributed not only between dots but also between the dot and the ABS. This behavior is well captured by the simple model, Fig. 6.3(d).

As in the case of a double quantum dot system[48, 49, 50, 51], decreasing coupling increases the quantum capacitance signal. Qualitatively, this can be understood as the strong interaction smears out the charge between subsystems, making transitions less sharp, such that the derivative of the charge w.r.t. the chemical potential becomes smaller. We verify this behavior by tuning the barrier between the gate-probed QD and the ABS. Interaction between the quantum dot and the ABS is revealed in the charge stability diagram while varying respective chemical potentials with the gates, Fig. 6.4(a), where we also observe the characteristic *S-shape* bending of the dot ABS-transition[34]. Decreasing the ABS-QD coupling, in turn, affects the coupling between quantum dots, re-

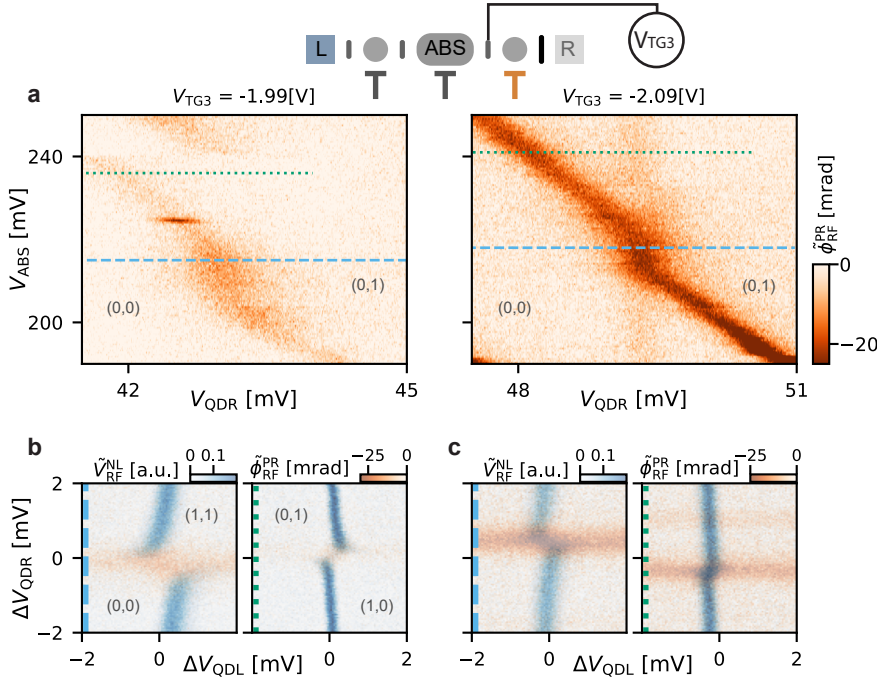


Figure 6.4: Effect of changing the interaction strength on the quantum capacitance signal. Increasing the tunnel barrier strength between the left gate-sensed quantum dot and the ABS decreases the interaction, in turn making the signal larger. The effect is visible in ABS-QD charge stability diagrams (a), as well as in avoided crossings between QD transitions (b,c).

sulting in smaller avoided crossings and an increase in the quantum capacitance signal, Fig. 6.4(c).

### 6.3. GATE SENSING WITHOUT NORMAL LEADS: EFFECTS OF PARITY

We have established that the gate sensing signal, corresponding to the quantum capacitance, agrees well with the system behavior observed from the normal lead reflectometry. However, we have swept under the rug an important aspect of the system, which was the main motivation for using gate sensing in the first place – the parity of the system. Indeed, the presence of a normal reservoir means that the system parity always corresponds to the lowest energy state, as it can always relax by emitting/absorbing a single quasiparticle.

The behavior changes drastically when the normal leads are pinched off. Now, the PMM system can be found in a parity state with higher energy. For example, when the odd parity state is energetically favorable  $E_o < E_e$ , the system can remain in the even state  $|e\rangle$ , as the parity is fixed. The mechanism flipping the parity is the quasiparticle

poisoning (QPP)[104, 105, 106, 107] from the superconducting terminal. Of course, QPP is also present when the normal leads are connected. However, its rate is much lower than the tunneling rate to the normal leads.

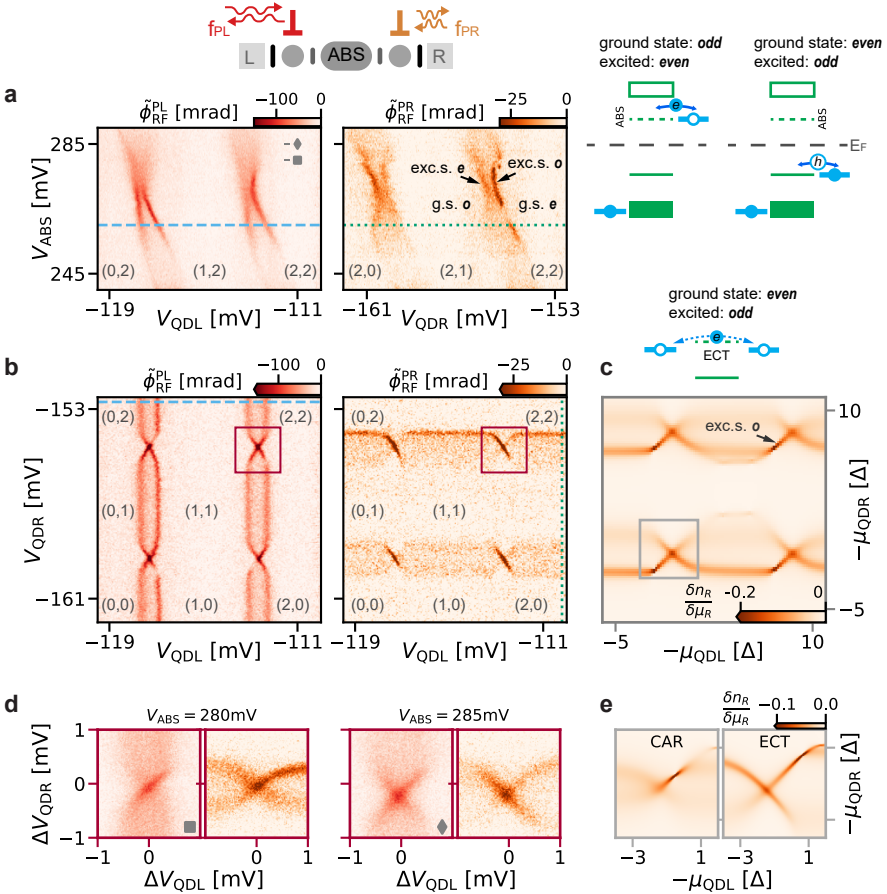


Figure 6.5: Quantum capacitance measurements of the PMM system without normal leads. The top panel (a) shows the effect of the system being in both parity states when measuring the interaction between individual QDs and the ABS, with the cartoon demonstrating that the ABS-dot hybridization happens predominantly in the poisoned state. Dot-dot charge stability diagrams (b, d) contain the signal originating from both ECT (diagonal lines) and CAR (anti-diagonal lines). Simulations (c, e) demonstrate qualitative agreement with the experimental data.

When the integration time for each point in the parameter space is larger than the QPP time, we expect the resulting signal to be the average of the components originating from the even and odd states. Those measurements are presented in Fig. 6.5. We first characterize how individual QDs interact with the ABS, recording corresponding charge stability diagrams. The signal around a QD charge transition comes in pairs, as the location of the maximum signal in the CSD is shifted between different parities.

A similar behavior is observed when capturing CSD for two QDs. Double-line features away from the dot-dot crossing points correspond to the QD-ABS interaction that has already been mentioned. At the regions of inter-dot transition, we observe diagonal and anti-diagonal lines corresponding to the ECT and CAR processes, respectively. The span of those lines is limited by roughly  $2E_{\text{ABS}}$  in terms of dot chemical potentials if we neglect hybridization between QDs and the ABS. Interestingly, compared to the single normal lead case, we can observe a stronger quantum capacitance signal originating from the weaker non-local process, present only when the system is in the energetically unfavorable parity state.

Varying the ABS chemical potential with the  $V_{\text{ABS}}$  gate, we observe a change in the (relative) magnitude of the ECT and CAR signals Fig. 6.5(d). Naively, we expect the signal strength to inversely correlate with the interaction strength, the behavior observed in the numerical simulations. As such, a PMM sweet spot would correspond to the regime of equal signal amplitude on the diagonal and anti-diagonal lines. However, it is possible that a strong coupling asymmetry between dots makes the analysis unreliable. Indeed, Fig. 6.5(d) doesn't show a clear correlation between left and right gate sensing signal, especially for the  $V_{\text{ABS}} = 285\text{mV}$ . We suggest that a further investigation to relate gate sensing signal with the relative strength of the non-local processes and sweet-spot location is needed, potentially using microwave signals to probe the system spectrum[86, 108, 109] without normal leads.

Finally, we explore the intermediate regime of normal lead being *almost* cut off when the lead-QD tunneling rate becomes comparable to the QPP rate. We note that the currents in the lead are still well below the detectable level. The idea behind the experiment is illustrated schematically in Fig. 6.6(a). Normal lead can both emit (**A**) and absorb (**B**) an electron into the adjacent QD, provided the chemical potential in the lead is above (below) the dot level.

The electron exchange with the normal lead changes the occupations of parity states depending on the position in the CSD, Fig. 6.6(b), and since the quantum capacitance signal originates predominantly from the excited parity state, we expect to see increased (reduced) signal when the excited (ground) state has higher occupation probability. This effect can be observed in Fig. 6.6(c) when varying the chemical potential in the right lead allows selecting between processes **A** ( $V_{\text{R}} = -150\mu\text{V}$ ) or **B** ( $V_{\text{R}} = +150\mu\text{V}$ ).

Focusing on the ABS-QD interaction, we observe that the threshold bias, at which the quantum capacitance and hence the occupation of parity states is affected, depends on the quantum dot level being aligned with the ABS energy  $E_{\text{ABS}}$ , in turn, tuned by the ABS chemical potential with the gate  $V_{\text{ABS}}$ . As one might expect, the effect is reduced until it disappears completely when closing the outer tunnel lead, Fig. 6.6(f).

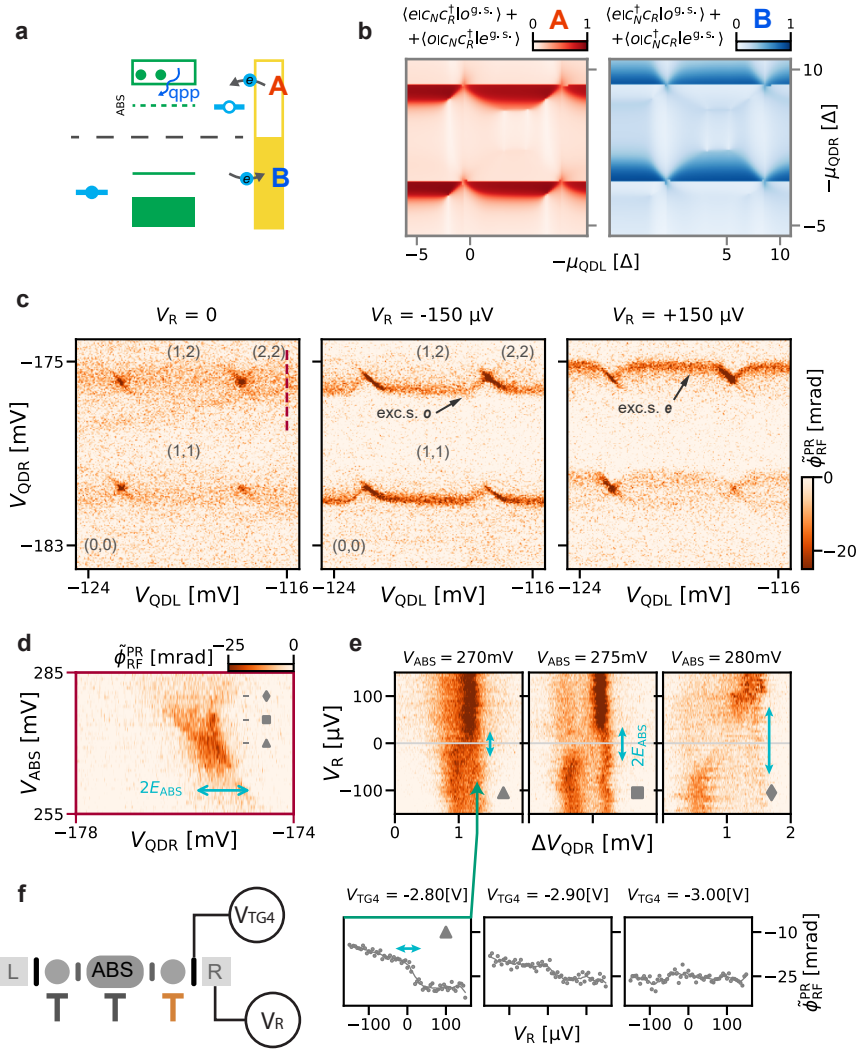


Figure 6.6: Effect of normal leads on the quasiparticle dynamic. **(a)**: Cartoon representation of the normal lead exchanging electrons with the dot. **(b)**: Numerical simulations showing regions of the charge stability diagram where the parity state can be excited by absorbing / emitting an electron. Predicted regions appear in the measured CSD **(c)** when the bias in the lead  $V_R$  allows for one of the processes. Focusing on the QD-ABS interaction **(d)**, line-cuts at different ABS chemical potentials demonstrate change in the threshold voltage bias **(e)**, evolving in a similar manner as the ABS energy. Increasing the outer tunnel barrier **(f)** reduces the variation in the gate sensing signal.

## 6.4. CONTROLLING THE ABS ENERGY WITH MAGNETIC FLUX

The ABS in the device is formed between two superconducting terminals, comprising a Josephson junction and embedded in a SC loop. We vary the phase difference  $\Delta\phi$  be-

tween the SC terminals with the out-of-plane field  $B_{\perp}$ , changing the ABS energy. This can be observed in the gate sensing signal of the QDs, interacting with the ABS, see Fig. 6.7, providing additional support for the correspondence between the ABS energy and the dot chemical potential distance between two signal branches.

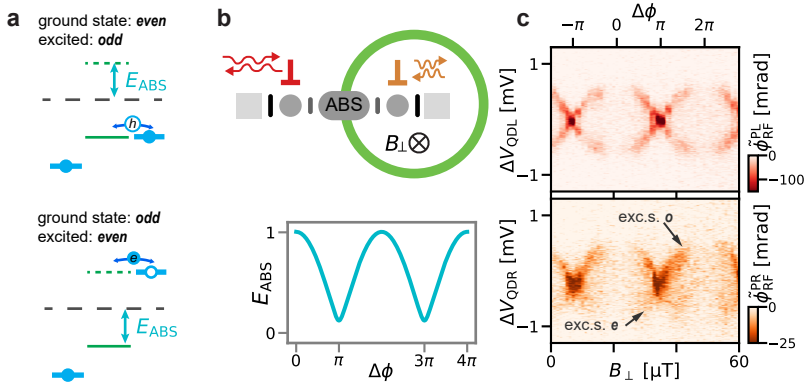


Figure 6.7: In a simplified picture (a), the gate sensing signal appears when the dot level is aligned with the ABS and the parity state is unfavorable in energy. Controlling the energy of the ABS via phase difference  $\Delta\phi(B_{\perp})$  (b), we observe modulation of the distance between two signal branches, measured separately for both QDs (c).

## 6.5. CHARGE SENSING

Another non-invasive method to deduce information about the state of a quantum system is charge sensing using a capacitively coupled QD[110, 111]. Change in the electron occupation on a sensed device shifts chemical potential levels in the sensor QD. In turn, the position of the sensor dot level can be detected with a single lead using RF reflectometry[60, 112], as the dissipation due to the Sisyphus resistance arises at the dot-lead resonance.

To establish the charge sensing in our material platform, suitable for the PMM applications, we use a device resembling the one discussed in this chapter but with a single superconducting lead, similar to the one in[38]. Furthermore, we energize tunnel gates such that only a single quantum dot is formed on the right side of the ABS, with the barrier between them preventing any transport and providing only capacitive coupling, Fig. 6.8(a). In this particular device, ABS region has relatively large charging energy, resulting in singlet–doublet ground state transitions as a function of the ABS chemical potential[95, 96, 97, 98, 99], revealed in the tunneling spectroscopy measurements, Fig. 6.8(b). At the transition points, we expect the charge to change abruptly[113], causing shifts in the sensor dot level.

This result demonstrates that the charge sensing technique can be employed in InSbAs 2DEG to characterize a full PMM device by incorporating additional quantum dots.

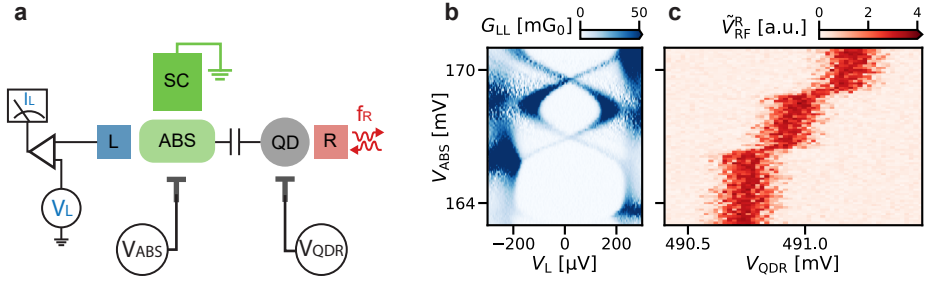


Figure 6.8: Schematic of the experiment (a), relating the charge and spectrum of the Andreev bound state. Varying the ABS chemical potential with the gate  $V_{ABS}$ , we observe singlet-doublet ground state transitions in the tunneling spectroscopy measurement (b), corresponding to the shifts in the sensor dot level (c), observed in the magnitude of the reflected RF voltage.

## 6.6. APPENDIX: DETAILS OF THE SIMULATIONS

Numerical simulations of the PMM system, shown in Figs. 6.3, 6.5, 6.6, were obtained using the three-site model, adapted from [35]. Considering that each site can be occupied by two spin species, the total dimension of the Fock space is 32 for each parity. The model is solved using numerical matrix diagonalization.

Below, we present plots of the charge expectation values on left and right quantum dots, as well as their derivatives w.r.t. the chemical potentials, corresponding to the quantum capacitance measurements. Here, we only consider the lowest energy eigenstate for each parity. Importantly, when computing system parameters, the parity is fixed, and to relate results to the observations, we need to either average the signal, assuming equal parity occupation, or condition the system to be in the parity state lowest in energy.

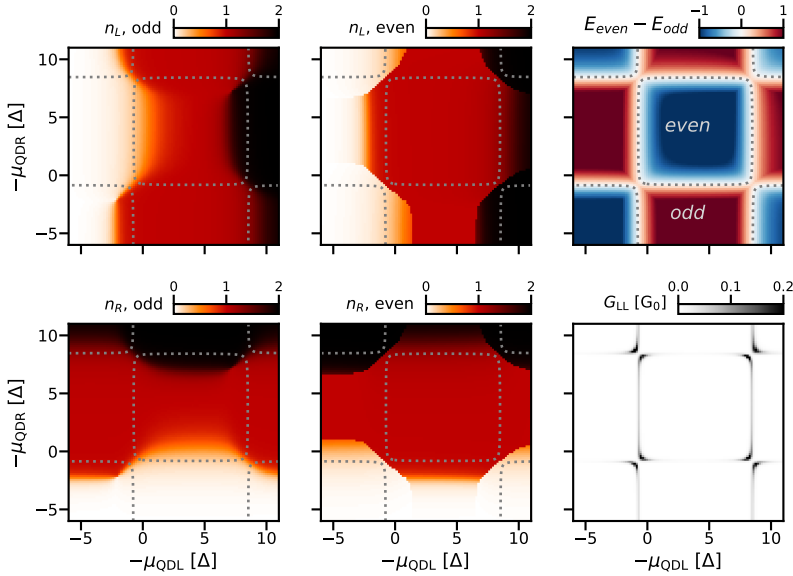


Figure 6.9: The expectation value of the charge on the left ( $n_L$ ) and right ( $n_R$ ) quantum dots are computed separately for even and odd parity subspace. The difference between energies of parity states provides information about the system's overall ground state, while the degeneracy points correspond to the local transport being allowed from the normal lead ( $G_{LL}$ ).

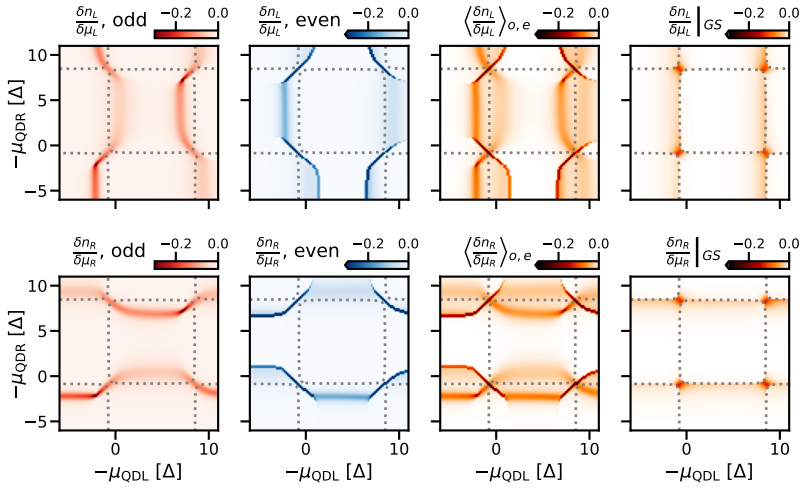


Figure 6.10: Derivatives of the charge expectation value w.r.t. the chemical potential of the corresponding dots, computed separately for each parity state. In the case of the QPP rate faster than the acquisition speed and no normal leads present, we expect both parities to have equal probability, and thus, the signal is the average of two parities. In contrast, presence of a normal lead forces the system to always be in the overall ground state, and the response can be found by conditioning the signal on the system parity.



# 7

## CONCLUSIONS AND OUTLOOK

*So there ain't nothing more to write about, and I am rotten glad of it, because if I'd a knowed what a trouble it was to make a book I wouldn't a tackled it and ain't going to no more.*

Mark Twain

### 7.1. RESULTS DISCUSSION

The results presented in this thesis lay the groundwork for further exploration of confined hybrid systems. The fabrication methods outlined in Chapter 3 have been extensively utilized in producing the devices studied. A common feature in the device design is the presence of a bottom global depletion gate, which defines the conductance path: ring-shaped in the case of the double-dot interferometer, and one-dimensional in the case of PMM devices discussed in Chapters 4,5,6. This bottom depletion gate was not only essential for device design but also crucial for RF gate sensing performance, as it screens plunger gates from potential charge islands that may form in the 2DEG. It is worth noting that, for conductance measurements, a single-layer gate design is viable for a PMM system.

Another significant development was the adaptation of the RF reflectometry measurement technique using off-chip resonators. This approach enables the characterization of quantum devices without the use of normal leads, which is essential for preserving parity. Additionally, RF reflectometry greatly accelerates conductance measurements. This seemingly qualitative improvement allows for the exploration of a vast parameter space and significantly speeds up the tuning process. A fast tune-up is particularly advantageous when searching for a stable gate regime, especially in devices prone to charge jumps.

Chapter 4 explored the non-local transport processes mediated by an ABS in a Josephson junction. We clearly resolved the ECT and CAR processes and demonstrated that

tuning the ABS via gate and phase control affects the amplitudes of non-local processes. However, extracting the phase dependence of ECT and CAR was complicated by local currents, which inevitably arose due to the selected measurement technique involving finite voltage biases. Additionally, the presence of multiple ABS in the device added complexity to the experimental system compared to the simple model. It should also be noted that a similar device was investigated in Chapter 6 in a strong coupling regime, where no clear phase tunability of the dominant interaction type was observed at the time of writing.

In contrast, the device studied in Chapter 5 exhibited a clear phase modulation of the inter-dot interaction, enabling tuning into the PMM sweet spot through phase difference control. This discrepancy compared to the previous device can be attributed to differences in geometry, which affect the ABS spectrum, its phase dependence, and the increased influence of spin-orbit interaction in the hybrid segment. We have also verified our understanding of a strongly coupled PMM system, confirming the presence of the wave function in the hybrid segment by leveraging the versatility of the 2DEG platform. The exact dependence of the interaction and the excitation gap on the phase difference did not align with the predictions of the simple model, which we attribute to the complex hybrid spectrum composed of multiple spin-split ABS states. However, this should not be discouraging, as the key aspect is the ability to tune the system into a PMM sweet spot and relax the geometric constraints on the hybrid segment length, which was successfully demonstrated.

Though some interesting physics can be inferred from tunneling spectroscopy measurements, focusing on a system with a well-defined parity requires the use of more advanced characterization methods – charge and gate sensing, explored in Chapter 6. We have shown that it is feasible to utilize gate sensing in the hybrid 2DEG platform, building on the design ideas developed for the double-dot loop interferometer. By differentiating the signal from two parity states, we showed that normal leads can be sufficiently pinched off by examining the bias effect on the distribution of parity states. However, we still need to demonstrate that the system can remain in a specific parity state for a duration significantly longer than the measurement time, or, equivalently, that the quasiparticle poisoning (QPP) rate is much lower than the measurement bandwidth (BW). This was not the case for the measurements presented in the Ch.6, where increasing the BW has led to signal-to-noise ratio deterioration without a clear signature of the even-odd switching. This can indicate that better care might be taken to reduce the QPP rate in the system, potentially through improved filtering techniques[114, 115], but also that the sensitivity of the gate sensing in our experiment was insufficient for parity readout. Further investigation is required to determine the QPP rate. A potential approach could involve using methods with higher sensitivity, such as charge sensing, to first estimate the QPP rate. If necessary, this can be followed by an investigation to determine if optimized gate sensing can achieve the required BW.

## 7.2. FURTHER DEVELOPMENT

Devices based on the 2DEG platform can be easily adapted for PMM charge sensing by adding extra sensing dots on the sides of the device or incorporating an antenna, Fig. 7.1. Both approaches have their own limitations in terms of gate layout and measurement

sensitivity.

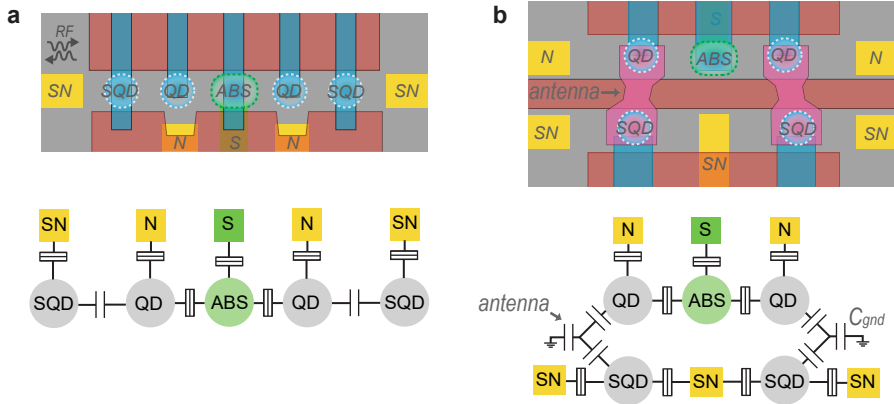


Figure 7.1: Potential layouts for PMM charge sensing are shown. Tunnel gates are omitted for simplicity. Sensing quantum dots (SQDs) can be placed on the sides of the PMM (a) within the same channel. The 2DEG platform allows for the inclusion of normal probes (N, yellow), facilitating the tune-up process. However, if the sensing dots are connected to only a single probe, as shown, they can only be probed using RF reflectometry. Alternatively, SQDs can be placed in a separate channel (b) and capacitively coupled to the PMM QDs using antennas (floating metallic gates). In this configuration, each sensing dot is connected to two normal leads, enabling conductance measurements for probing the SQDs. The parasitic capacitance  $C_{gnd}$  between an antenna and the bottom depletion gate reduces the effective sensitivity and imposes geometric constraints on the design.

The parity of the PMM system can be measured without detuning from the sweet spot by utilizing a loop quantum dot interferometer (Ch.3), following the approach described in[116]. However, in the near-term experiments, focusing on a much simpler technique of dot detuning and local measurement might be more fruitful. Moreover, controlling the flux through a small loop formed between dots on a fast enough time scale poses a significant challenge due to the large currents required. It should be noted that a gate, capacitively coupled to both QDs, can also be used to read out the non-local parity[91].

Of course, fabrication and materials play a crucial role, alongside device design and measurement techniques. Several useful improvements have already been mentioned above. Below, I provide details on additional developments, some of which can be directly applied, while others require further investigation.

### 7.2.1. RETHINKING FAB AND MATERIALS

We have seen that Al etching is a crucial and yet a low-yield process, primarily due to poor resist adhesion. At the same time, the requirements for the Al feature size are shrinking. When working with ternary InSbAs compounds, the temperature budget is strongly limited, compromising the resist quality. Utilizing a hard mask for Al etching has the potential to address this issue, see Fig. 7.2. Perfecting Al etching would not only resolve the yield issue but, like many other fabrication improvements, would pave the

way for a multitude of new devices. These could include on-chip inductors, such as nanowire kinetic inductors and arrays of Josephson junctions.



Figure 7.2: Patterning of the aluminum superconducting layer using a grown hard mask. Areas, where Al will be removed, are covered with resist (preferably ARP for better plasma resilience). The sample is then exposed (1) to a fluorine-rich plasma, such as SF<sub>6</sub>, which creates a thin (few nanometers) layer of AlF<sub>3</sub> at the surface of the Al layer. Preventing prolonged sample exposure to the ambient air, the resist is immediately removed in an organic solvent (2). The sample is then etched (3) in heated to 40 °C Transene aluminum etchant type D, with etching time dependent on the Al layer properties (usually around 10 s). AlF<sub>3</sub> is removed in warm water (4). SEM micrograph of the Al structure, patterned on InSbAs 2DEG with the described method, is shown in the bottom right corner.

Another potential direction is to revise the superconducting layer. One of the most common superconductors used with III/V semiconductors is aluminum. It has favorable band-bending[22, 42] preventing Schottky barrier formation at the super-semi interface, offers selective chemical patterning, forms self-terminating native oxide, and can be uniformly deposited epitaxially[117] with thicknesses significantly smaller than magnetic penetration length, thereby achieving an increased in-plane critical field. Al is shown to induce strong proximity in InSbAs 2DEGs.

Despite the advantages of Al films, a wider selection of superconducting materials could expand the application range and operational parameters of quantum devices. Specifically, group V metals, such as vanadium, niobium, and tantalum, offer increased superconducting gap, larger in- and out-of-plane critical magnetic fields, and can be deposited with conventional PVD. A higher magnetic field increases Zeeman splitting, which can improve the polarization of PMM states and might be necessary for materials with smaller *g*-factors, such as InAs 2DEGs.

However, patterning group V materials on a semiconducting 2DEG can be complicated, as the available etchants are too aggressive. As such, an interesting approach can be to combine the two materials[118]. Aluminum, in that case, can serve two purposes - providing an epitaxial interface, as well as acting as an etch stop layer for the patterning purpose. Al can be selectively etched away in a wet process. An alternative method is to utilize a very thin Al layer (few nm), which, when exposed, oxidizes completely. Further investigation is required to ensure that the resulting native oxide does not negatively impact the device's stability due to charge traps in the material.

The preliminary results, shown in Fig. 7.3, demonstrate an increased induced gap.

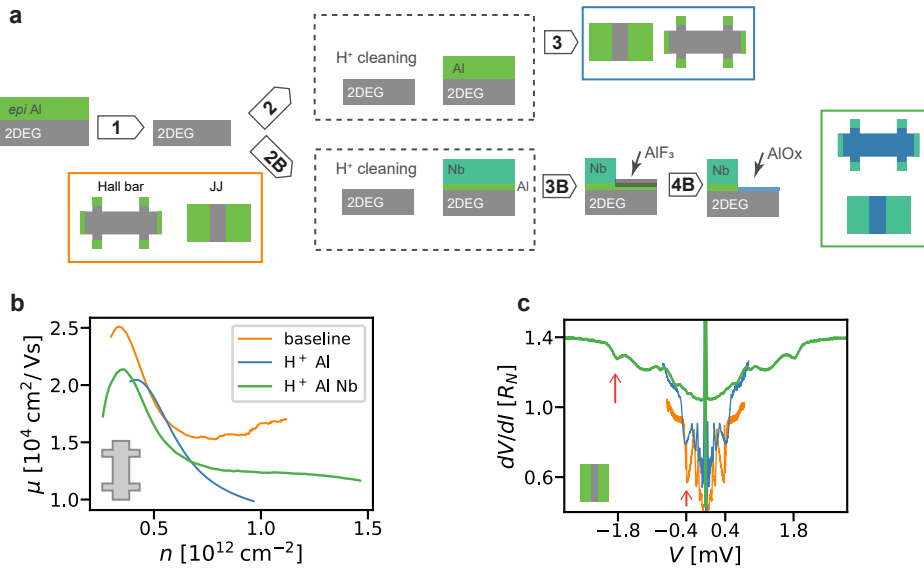


Figure 7.3: Initial study of the Al/Nb superconducting bilayer. Fabrication flow is schematized in (a). We start with 2DEG samples covered with epitaxially deposited Al. This layer is covered with native oxide and thus not suitable for depositing Nb layer on top. We remove Al by wet etching in Transene D (1). At this stage, we also characterize the baseline performance of the 2DEG with Hall bar measurements (b), plotting mobility as a function of density. Induced superconductivity is demonstrated in the multiple Andreev reflection (MAR) [119] plots (c, with plots offset for clarity), where a red arrow indicates the first-order resistance dip, corresponding to the  $2\Delta_{ind}$  value (we note that for highly transparent junctions this relation is modified [120]). After exposure to ambient air, the 2DEG surface has to be cleaned *in situ* before superconductor PVD. Hydrogen radicals are used for that purpose [121]. We separately optimize the performance of the hydrogen cleaning, depositing only the Al layer (2) and patterning it using wet etching (3). Device characterization demonstrates some mobility reduction, while induced superconductivity is on par with the epitaxial aluminum. Finally, we test Al/Nb bilayer deposition (2B). The bilayer is patterned by first etching the Nb in a fluorine-based plasma (3B), with Al acting as an etch stop by forming a hardened AlF<sub>3</sub> layer. AlF<sub>3</sub> layer is removed by prolonged exposure in warm water (4B). The initial thickness of the Al layer was chosen so that after fluoride removal, the remaining Al is fully oxidized. This somewhat elaborate process does not cause any mobility deterioration apart from attributed to the hydrogen cleaning. MAR measurement demonstrates an enhanced induced gap, though the conductance peaks are less prominent.

However, transparency is limited (in the range of 0.70.8, as deduced from the excess current). Potential culprits include the poor quality of the deposited Nb, the absence of a capping layer leading to Nb oxidation, and damage to the Al-2DEG interface due to the extremely high thermal radiation from the Nb crucible during evaporation. In summary, the bilayer large-gap superconductor stack adds complexity to the fabrication process, and several unknowns remain regarding process performance. Nevertheless, further investigation may be warranted if the properties of Al become the limiting factor.

Finally, we should critically examine the material comprising the 2DEG – the ternary compound InSbAs. Despite its unique properties, it is challenging to fabricate devices using this material due to its low thermal budget. Moreover, its availability to the scientific community seems to have stalled. Therefore, alternative 2DEG platforms need to

be explored. A natural candidate is InAs, which has a well-established record of inducing superconductivity in mesoscopic structures [120, 122, 123]. The downsides include a reduced effective Landé  $g$ -factor, which hinders experiments requiring high Zeeman splitting, and an increased effective mass, which reduces the level spacing. We have initiated experiments with InAs as a potential replacement for the ternary 2DEG and have demonstrated promising preliminary results, Fig. 7.4.

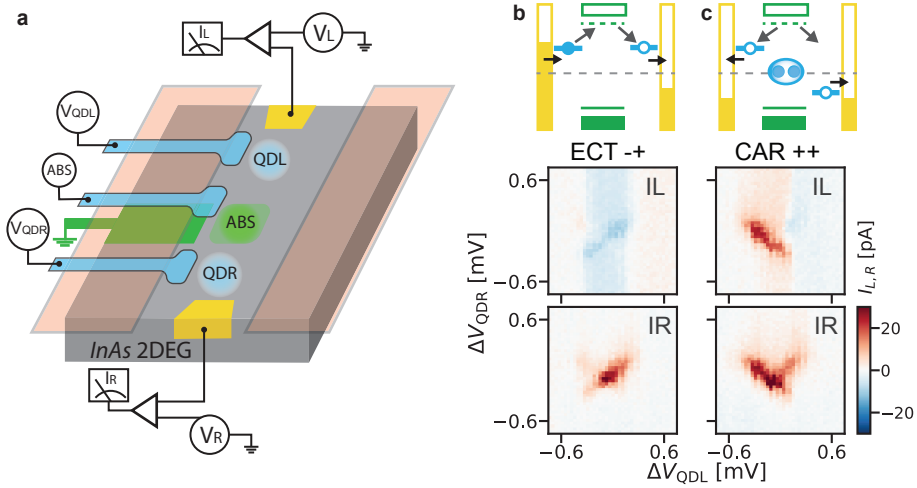


Figure 7.4: Initial demonstration of non-local transport processes in InAs 2DEG. The device is schematically shown in (a). Despite showing ECT (b) and CAR (c), this particular sample suffered from gate instabilities and was not measured further. Deviations from clear ECT and CAR signals, presented elsewhere in this thesis, are partly attributed to voltage offsets in the normal leads.

It should be emphasized that most of the fabrication and design techniques can be applied directly to InAs 2DEG, including AIF hard mask aluminum etching and multi-layered superconducting stacks. Ohmic contacts with ALD-through vias can be used for the compact frame gate design, addressing the potential issue of parasitic edge conductance, Fig. 7.5.

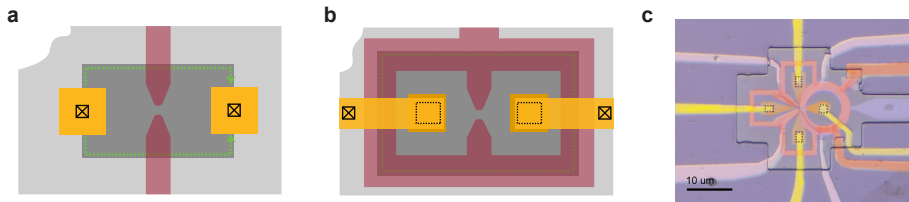


Figure 7.5: It is possible that the combination of the 2DEG and the gate dielectric materials results in the mesa edges having residual conductance[124, 125], schematically shown for a quantum point contact device (a). By contacting the device inside the depletion gate through vias in the dielectric layer (b), the parasitic channel contribution to the conductance is eliminated. Optical micrograph (c) demonstrates a device with the compact frame gate and four normal leads, implemented in InAs 2DEG.



# BIBLIOGRAPHY

- [1] Burkard, G., Ladd, T. D., Pan, A., Nichol, J. M., & Petta, J. R. (2023). Semiconductor spin qubits. *Reviews of Modern Physics*, 95(2), 025003. <https://doi.org/10.1103/RevModPhys.95.025003>
- [2] Barthelemy, P., & Vandersypen, L. M. (2013). Quantum dot systems: a versatile platform for quantum simulations. *Annalen der Physik*, 525(10-11), 808–826. <https://doi.org/10.1002/andp.201300124>
- [3] Hensgens, T., Fujita, T., Janssen, L., Li, X., Van Diepen, C., Reichl, C., Wegscheider, W., Das Sarma, S., & Vandersypen, L. M. (2017). Quantum simulation of a Fermi–Hubbard model using a semiconductor quantum dot array. *Nature*, 548(7665), 70–73. <https://doi.org/10.1038/nature23022>
- [4] Kiczynski, M., Gorman, S., Geng, H., Donnelly, M., Chung, Y., He, Y., Keizer, J., & Simmons, M. (2022). Engineering topological states in atom-based semiconductor quantum dots. *Nature*, 606(7915), 694–699. <https://doi.org/10.1038/s41586-022-04706-0>
- [5] Esposito, M., Ranadive, A., Planat, L., & Roch, N. (2021). Perspective on traveling wave microwave parametric amplifiers. *Applied Physics Letters*, 119(12). <https://doi.org/10.1063/5.0064892>
- [6] Leijnse, M., & Flensberg, K. (2012a). Introduction to topological superconductivity and Majorana fermions. *Semiconductor Science and Technology*, 27(12), 124003. <https://doi.org/10.1088/0268-1242/27/12/124003>
- [7] Kitaev, A. Y. (2001). Unpaired Majorana fermions in quantum wires. *Physics-uspekhi*, 44(10S), 131. <https://doi.org/10.1070/1063-7869/44/10S/S29>
- [8] Oreg, Y., Refael, G., & Von Oppen, F. (2010). Helical liquids and Majorana bound states in quantum wires. *Physical review letters*, 105(17), 177002. <https://doi.org/10.1103/PhysRevLett.105.177002>
- [9] Lutchyn, R. M., Sau, J. D., & Das Sarma, S. (2010). Majorana Fermions and a Topological Phase Transition in Semiconductor-Superconductor Heterostructures. *Physical review letters*, 105(7), 077001. <https://doi.org/10.1103/PhysRevLett.105.077001>
- [10] Ahn, S., Pan, H., Woods, B., Stanescu, T. D., & Das Sarma, S. (2021). Estimating disorder and its adverse effects in semiconductor Majorana nanowires. *Physical Review Materials*, 5(12), 124602. <https://doi.org/10.1103/PhysRevMaterials.5.124602>
- [11] Sau, J. D., & Sarma, S. D. (2012). Realizing a robust practical Majorana chain in a quantum-dot-superconductor linear array. *Nature communications*, 3(1), 964. <https://doi.org/10.1038/ncomms1966>
- [12] Leijnse, M., & Flensberg, K. (2012b). Parity qubits and poor man’s Majorana bound states in double quantum dots. *Physical Review B*, 86(13), 134528. <https://doi.org/10.1103/PhysRevB.86.134528>

- [13] Vilkelis, K., Manesco, A., Luna, J. D. T., Miles, S., Wimmer, M., & Akhmerov, A. (2024). Fermionic quantum computation with Cooper pair splitters. *SciPost Phys.*, 16, 135. <https://doi.org/10.21468/SciPostPhys.16.5.135>
- [14] Pino, D. M., Souto, R. S., & Aguado, R. (2024). Minimal Kitaev-transmon qubit based on double quantum dots. *Physical Review B*, 109(7), 075101. <https://doi.org/10.1103/PhysRevB.109.075101>
- [15] Leijnse, M., & Flensberg, K. (2013). Coupling spin qubits via superconductors. *Physical review letters*, 111(6), 060501. <https://doi.org/10.1103/PhysRevLett.111.060501>
- [16] Kulesh, I. (2024). *Raw data and analysis scripts accompanying the PhD thesis*. 4TU.ResearchData. <https://doi.org/10.4121/558017cb-7964-4f5a-8fb2-4fe489f1555d>
- [17] Ihn, T. (2009). *Semiconductor Nanostructures: Quantum states and electronic transport*. OUP Oxford. <https://doi.org/10.1093/acprof:oso/9780199534425.003.0001>
- [18] Schäpers, T. (2021). *Semiconductor spintronics*. Walter de Gruyter GmbH & Co KG. <https://doi.org/10.1515/9783110639001>
- [19] Kouwenhoven, L. P., Austing, D., & Tarucha, S. (2001). Few-electron quantum dots. *Reports on progress in physics*, 64(6), 701. <https://doi.org/10.1088/0034-4885/64/6/201>
- [20] Hanson, R., Kouwenhoven, L. P., Petta, J. R., Tarucha, S., & Vandersypen, L. M. (2007). Spins in few-electron quantum dots. *Reviews of modern physics*, 79(4), 1217. <https://doi.org/10.1103/RevModPhys.79.1217>
- [21] Mikkelsen, A. E., Kotetes, P., Krogstrup, P., & Flensberg, K. (2018). Hybridization at superconductor-semiconductor interfaces. *Physical Review X*, 8(3), 031040. <https://doi.org/10.1103/PhysRevX.8.031040>
- [22] Schuwalow, S., Schröter, N. B., Gukelberger, J., Thomas, C., Strocov, V., Gamble, J., Chikina, A., Caputo, M., Krieger, J., Gardner, G. C., et al. (2021). Band Structure Extraction at Hybrid Narrow-Gap Semiconductor–Metal Interfaces. *Advanced Science*, 8(4), 2003087. <https://doi.org/10.1002/advs.202003087>
- [23] Liu, C.-X., Schuwalow, S., Liu, Y., Vilkelis, K., Manesco, A., Krogstrup, P., & Wimmer, M. (2021). Electronic properties of InAs/EuS/Al hybrid nanowires. *Physical Review B*, 104(1), 014516. <https://doi.org/10.1103/PhysRevB.104.014516>
- [24] Wang, G. (2023). *Quantum Dots Coupled to Superconductors* [Doctoral dissertation]. <https://doi.org/10.4233/uuid:b86bec0b-0f27-4fac-90ae-7ad4bcac407a>
- [25] Souto, R. S., & Aguado, R. (2024). Subgap states in semiconductor-superconductor devices for quantum technologies: Andreev qubits and minimal Majorana chains. *arXiv preprint arXiv:2404.06592*. <https://doi.org/10.48550/arXiv.2404.06592>
- [26] Bretheau, L. (2013). *Localized excitations in superconducting atomic contacts: probing the Andreev doublet* [Doctoral dissertation, Ecole Polytechnique X].
- [27] Hays, M. (2022). *Realizing an Andreev Spin Qubit: Exploring Sub-gap Structure in Josephson Nanowires Using Circuit QED* [Doctoral dissertation]. <https://doi.org/10.1007/978-3-030-83879-9>

- [28] Schindele, J., Baumgartner, A., Maurand, R., Weiss, M., & Schönenberger, C. (2014). Nonlocal spectroscopy of Andreev bound states. *Physical Review B*, 89(4), 045422. <https://doi.org/10.1103/PhysRevB.89.045422>
- [29] Oriekhov, D., Cheipesh, Y., & Beenakker, C. (2021). Voltage staircase in a current-biased quantum-dot Josephson junction. *Physical Review B*, 103(9), 094518. <https://doi.org/10.1103/PhysRevB.103.094518>
- [30] Luna, J. D. T., Bozkurt, A. M., Wimmer, M., & Liu, C.-X. (2024). Flux-tunable Kitaev chain in a quantum dot array. *arXiv preprint arXiv:2402.07575*. <https://doi.org/10.48550/arXiv.2402.07575>
- [31] Liu, C.-X., Wang, G., Dvir, T., & Wimmer, M. (2022). Tunable superconducting coupling of quantum dots via Andreev bound states in semiconductor-superconductor nanowires. *Physical review letters*, 129(26), 267701. <https://doi.org/10.1103/PhysRevLett.129.267701>
- [32] Bordin, A., Wang, G., Liu, C.-X., Ten Haaf, S. L., Van Loo, N., Mazur, G. P., Xu, D., Van Driel, D., Zatelli, F., Gazibegovic, S., et al. (2023). Tunable crossed Andreev reflection and elastic cotunneling in hybrid nanowires. *Physical Review X*, 13(3), 031031. <https://doi.org/10.1103/PhysRevX.13.031031>
- [33] Tsintzis, A., Souto, R. S., & Leijnse, M. (2022). Creating and detecting poor man's Majorana bound states in interacting quantum dots. *Physical Review B*, 106(20), L201404. <https://doi.org/10.1103/PhysRevB.106.L201404>
- [34] Liu, C.-X., Bozkurt, A. M., Zatelli, F., ten Haaf, S. L., Dvir, T., & Wimmer, M. (2023). Enhancing the excitation gap of a quantum-dot-based Kitaev chain. *arXiv preprint arXiv:2310.09106*. <https://doi.org/10.48550/arXiv.2310.09106>
- [35] Zatelli, F., van Driel, D., Xu, D., Wang, G., Liu, C.-X., Bordin, A., Roovers, B., Mazur, G. P., van Loo, N., Wolff, J. C., et al. (2023). Robust poor man's Majorana zero modes using Yu-Shiba-Rusinov states. *arXiv preprint arXiv:2311.03193*. <https://doi.org/10.48550/arXiv.2311.03193>
- [36] ten Haaf, S. L., Wang, Q., Bozkurt, A. M., Liu, C.-X., Kulesh, I., Kim, P., Xiao, D., Thomas, C., Manfra, M. J., Dvir, T., et al. (2023). Engineering Majorana bound states in coupled quantum dots in a two-dimensional electron gas. *arXiv preprint arXiv:2311.03208*. <https://doi.org/10.48550/arXiv.2311.03208>
- [37] Prosko, C. G., Kulesh, I., Chan, M., Han, L., Xiao, D., Thomas, C., Manfra, M., Goswami, S., & Malinowski, F. K. (2024). Flux-tunable hybridization in a double quantum dot interferometer. *SciPost Physics*, 17(3), 074. <https://doi.org/10.21468/SciPostPhys.17.3.074>
- [38] Wang, Q., Ten Haaf, S. L., Kulesh, I., Xiao, D., Thomas, C., Manfra, M. J., & Goswami, S. (2023). Triplet correlations in Cooper pair splitters realized in a two-dimensional electron gas. *Nature Communications*, 14(1), 4876. <https://doi.org/10.1038/s41467-023-40551-z>
- [39] Prosko, C. G., Huisman, W. D., Kulesh, I., Xiao, D., Thomas, C., Manfra, M. J., & Goswami, S. (2024). Flux-tunable Josephson effect in a four-terminal junction. *Physical Review B*, 110(6), 064518. <https://doi.org/10.1103/PhysRevB.110.064518>
- [40] Moehle, C. M., Ke, C. T., Wang, Q., Thomas, C., Xiao, D., Karwal, S., Lodari, M., van de Kerkhof, V., Termaat, R., Gardner, G. C., et al. (2021). InSbAs two-

- dimensional electron gases as a platform for topological superconductivity. *Nano Letters*, 21(23), 9990–9996. <https://doi.org/10.1021/acs.nanolett.1c03520>
- [41] Reeg, C. R., & Maslov, D. L. (2015). Proximity-induced triplet superconductivity in Rashba materials. *Physical Review B*, 92(13), 134512. <https://doi.org/10.1103/PhysRevB.92.134512>
- [42] Mayer, W., Schiela, W. F., Yuan, J., Hatefipour, M., Sarney, W. L., Svensson, S. P., Leff, A. C., Campos, T., Wickramasinghe, K. S., Dartiailh, M. C., et al. (2020). Superconducting proximity effect in InAsSb surface quantum wells with in situ Al contacts. *ACS Applied Electronic Materials*, 2(8), 2351–2356. <https://doi.org/10.1021/acsaelm.0c00269>
- [43] Ciorga, M., Sachrajda, A., Hawrylak, P., Gould, C., Zawadzki, P., Jullian, S., Feng, Y., & Wasilewski, Z. (2000). Addition spectrum of a lateral dot from Coulomb and spin-blockade spectroscopy. *Physical Review B*, 61(24), R16315. <https://doi.org/10.1103/PhysRevB.61.R16315>
- [44] Mortemousque, P.-A., Chanrion, E., Jadot, B., Flentje, H., Ludwig, A., Wieck, A. D., Urdampilleta, M., Bäuerle, C., & Meunier, T. (2021). Coherent control of individual electron spins in a two-dimensional quantum dot array. *Nature Nanotechnology*, 16(3), 296–301. <https://doi.org/10.1038/s41565-020-00816-w>
- [45] Tadokoro, M., Nakajima, T., Kobayashi, T., Takeda, K., Noiri, A., Tomari, K., Yoneda, J., Tarucha, S., & Koderu, T. (2021). Designs for a two-dimensional Si quantum dot array with spin qubit addressability. *Scientific Reports*, 11(1), 19406. <https://doi.org/10.1038/s41598-021-98212-4>
- [46] Borsoi, E., Hendrickx, N. W., John, V., Meyer, M., Motz, S., Van Riggelen, E., Sammak, A., De Snoo, S. L., Scappucci, G., & Veldhorst, M. (2024). Shared control of a 16 semiconductor quantum dot crossbar array. *Nature Nanotechnology*, 19(1), 21–27. <https://doi.org/10.1038/s41565-023-01491-3>
- [47] Croot, X., Pauka, S., Jarratt, M., Lu, H., Gossard, A., Watson, J., Gardner, G., Fallahi, S., Manfra, M., & Reilly, D. (2019). Gate-sensing charge pockets in the semiconductor-qubit environment. *Physical Review Applied*, 11(6), 064027. <https://doi.org/10.1103/PhysRevApplied.11.064027>
- [48] Cottet, A., Mora, C., & Kontos, T. (2011). Mesoscopic admittance of a double quantum dot. *Physical Review B*, 83(12), 121311. <https://doi.org/10.1103/PhysRevB.83.121311>
- [49] Urdampilleta, M., Chatterjee, A., Lo, C. C., Kobayashi, T., Mansir, J., Barraud, S., Betz, A. C., Rogge, S., Gonzalez-Zalba, M. F., & Morton, J. J. (2015). Charge dynamics and spin blockade in a hybrid double quantum dot in silicon. *Physical Review X*, 5(3), 031024. <https://doi.org/10.1103/PhysRevX.5.031024>
- [50] Mizuta, R., Otxoa, R., Betz, A., & Gonzalez-Zalba, M. F. (2017). Quantum and tunneling capacitance in charge and spin qubits. *Physical Review B*, 95(4), 045414. <https://doi.org/10.1103/PhysRevB.95.045414>
- [51] Talbo, V., Lavagna, M., Duong, T., & Crépieux, A. (2018). Charge susceptibility and conductances of a double quantum dot. *AIP Advances*, 8(10), 106311. <https://doi.org/10.1063/1.5043108>
- [52] De Jong, D., Van Veen, J., Binci, L., Singh, A., Krogstrup, P., Kouwenhoven, L. P., Pfaff, W., & Watson, J. D. (2019). Rapid detection of coherent tunneling in an in as

- nanowire quantum dot through dispersive gate sensing. *Physical Review Applied*, *11*(4), 044061. <https://doi.org/10.1103/PhysRevApplied.11.044061>
- [53] Vigneau, F., Fedele, F., Chatterjee, A., Reilly, D., Kuemmeth, F., Gonzalez-Zalba, M. F., Laird, E., & Ares, N. (2023). Probing quantum devices with radio-frequency reflectometry. *Applied Physics Reviews*, *10*(2). <https://doi.org/10.1063/5.0088229>
- [54] Moehle, C. M., Rout, P. K., Jainandunsing, N. A., Kuri, D., Ke, C. T., Xiao, D., Thomas, C., Manfra, M. J., Nowak, M. P., & Goswami, S. (2022). Controlling Andreev bound states with the magnetic vector potential. *Nano Letters*, *22*(21), 8601–8607. <https://doi.org/10.1021/acs.nanolett.2c03130>
- [55] Banerjee, A., Lesser, O., Rahman, M., Thomas, C., Wang, T., Manfra, M., Berg, E., Oreg, Y., Stern, A., & Marcus, C. (2023). Local and nonlocal transport spectroscopy in planar Josephson junctions. *Physical review letters*, *130*(9), 096202. <https://doi.org/10.1103/PhysRevLett.130.096202>
- [56] Coraiola, M., Haxell, D. Z., Sabonis, D., Weisbrich, H., Svetogorov, A. E., Hinderling, M., Ten Kate, S. C., Cheah, E., Krizek, F., Schott, R., et al. (2023). Phase-engineering the Andreev band structure of a three-terminal Josephson junction. *Nature Communications*, *14*(1), 6784. <https://doi.org/10.1038/s41467-023-42356-6>
- [57] Matsuo, S., Imoto, T., Yokoyama, T., Sato, Y., Lindemann, T., Gronin, S., Gardner, G. C., Nakosai, S., Tanaka, Y., Manfra, M. J., et al. (2023). Phase-dependent Andreev molecules and superconducting gap closing in coherently-coupled Josephson junctions. *Nature Communications*, *14*(1), 8271. <https://doi.org/10.1038/s41467-023-44111-3>
- [58] Rasmussen, S. E., Christensen, K. S., Pedersen, S. P., Kristensen, L. B., Bækkegaard, T., Loft, N. J. S., & Zinner, N. T. (2021). Superconducting circuit companion introduction with worked examples. *PRX Quantum*, *2*(4), 040204. <https://doi.org/10.1103/PRXQuantum.2.040204>
- [59] Persson, E., Wilson, C., Sandberg, M., & Delsing, P. (2010). Fast readout of a single Cooper-pair box using its quantum capacitance. *Physical Review B*, *82*(13), 134533. <https://doi.org/10.1103/PhysRevB.82.134533>
- [60] Gonzalez-Zalba, M., Barraud, S., Ferguson, A., & Betz, A. (2015). Probing the limits of gate-based charge sensing. *Nature communications*, *6*(1), 1–8. <https://doi.org/10.1038/ncomms7084>
- [61] Schoelkopf, R., Wahlgren, P., Kozhevnikov, A., Delsing, P., & Prober, D. (1998). The radio-frequency single-electron transistor (RF-SET): A fast and ultrasensitive electrometer. *science*, *280*(5367), 1238–1242. <https://doi.org/10.1126/science.280.5367.1238>
- [62] Reilly, D., Marcus, C., Hanson, M., & Gossard, A. (2007). Fast single-charge sensing with a rf quantum point contact. *Applied Physics Letters*, *91*(16). <https://doi.org/10.1063/1.2794995>
- [63] Razmadze, D., Sabonis, D., Malinowski, F. K., Ménard, G. C., Pauka, S., Nguyen, H., van Zanten, D. M., Eoin, C., Suter, J., Krogstrup, P., et al. (2019). Radio-frequency methods for Majorana-based quantum devices: Fast charge sensing and phase-diagram mapping. *Physical Review Applied*, *11*(6), 064011. <https://doi.org/10.1103/PhysRevApplied.11.064011>

- [64] Hornibrook, J., Colless, J., Mahoney, A., Croot, X., Blanvillain, S., Lu, H., Gossard, A., & Reilly, D. (2014). Frequency multiplexing for readout of spin qubits. *Applied Physics Letters*, 104(10). <https://doi.org/10.1063/1.4868107>
- [65] Thomas, C., Diaz, R. E., Dycus, J. H., Salmon, M. E., Daniel, R. E., Wang, T., Gardner, G. C., & Manfra, M. J. (2019). Toward durable Al-InSb hybrid heterostructures via epitaxy of 2ML interfacial InAs screening layers. *Physical Review Materials*, 3(12), 124202. <https://doi.org/10.1103/PhysRevMaterials.3.124202>
- [66] Lesovik, G. B., Martin, T., & Blatter, G. (2001). Electronic entanglement in the vicinity of a superconductor. *The European Physical Journal B-Condensed Matter and Complex Systems*, 24, 287–290. <https://doi.org/10.1007/s10051-001-8675-4>
- [67] Recher, P., Sukhorukov, E. V., & Loss, D. (2001). Andreev tunneling, Coulomb blockade, and resonant transport of nonlocal spin-entangled electrons. *Physical Review B*, 63(16), 165314. <https://doi.org/10.1103/PhysRevB.63.165314>
- [68] Chtchelkatchev, N. M., Blatter, G., Lesovik, G. B., & Martin, T. (2002). Bell inequalities and entanglement in solid-state devices. *Physical Review B*, 66(16), 161320. <https://doi.org/10.1103/PhysRevB.66.161320>
- [69] Hofstetter, L., Csonka, S., Nygård, J., & Schönberger, C. (2009). Cooper pair splitter realized in a two-quantum-dot Y-junction. *Nature*, 461(7266), 960–963. <https://doi.org/10.1038/nature08432>
- [70] Herrmann, L., Portier, F., Roche, P., Yeyati, A. L., Kontos, T., & Strunk, C. (2010). Carbon nanotubes as cooper-pair beam splitters. *Physical review letters*, 104(2), 026801. <https://doi.org/10.1103/PhysRevLett.104.026801>
- [71] Hofstetter, L., Csonka, S., Baumgartner, A., Fülöp, G., dHollosoy, S., Nygård, J., & Schönberger, C. (2011). Finite-bias Cooper pair splitting. *Physical review letters*, 107(13), 136801. <https://doi.org/10.1103/PhysRevLett.107.136801>
- [72] Schindele, J., Baumgartner, A., & Schönberger, C. (2012). Near-unity Cooper pair splitting efficiency. *Physical review letters*, 109(15), 157002. <https://doi.org/10.1103/PhysRevLett.109.157002>
- [73] Borzenets, I., Shimazaki, Y., Jones, G., Craciun, M. F., Russo, S., Yamamoto, M., & Tarucha, S. (2016). High efficiency CVD graphene-lead (Pb) Cooper pair splitter. *Scientific reports*, 6(1), 23051. <https://doi.org/10.1038/srep23051>
- [74] Wang, G., Dvir, T., Mazur, G. P., Liu, C.-X., van Loo, N., Ten Haaf, S. L., Bordin, A., Gazibegovic, S., Badawy, G., Bakkers, E. P., et al. (2022). Singlet and triplet Cooper pair splitting in hybrid superconducting nanowires. *Nature*, 612(7940), 448–453. <https://doi.org/10.1038/s41586-022-05352-2>
- [75] Nichele, F., Portolés, E., Fornieri, A., Whiticar, A. M., Drachmann, A. C., Gronin, S., Wang, T., Gardner, G., Thomas, C., Hatke, A., et al. (2020). Relating Andreev bound states and supercurrents in hybrid Josephson junctions. *Physical review letters*, 124(22), 226801. <https://doi.org/10.1103/PhysRevLett.124.226801>
- [76] Danon, J., Hellenes, A. B., Hansen, E. B., Casparis, L., Higginbotham, A. P., & Flensberg, K. (2020). Nonlocal conductance spectroscopy of Andreev bound states: symmetry relations and BCS charges. *Physical Review Letters*, 124(3), 036801. <https://doi.org/10.1103/PhysRevLett.124.036801>
- [77] Ménard, G., Anselmetti, G., Martinez, E., Puglia, D., Malinowski, F., Lee, J., Choi, S., Pendharkar, M., Palmstrøm, C., Flensberg, K., et al. (2020). Conductance-

- matrix symmetries of a three-terminal hybrid device. *Physical Review Letters*, 124(3), 036802. <https://doi.org/10.1103/PhysRevLett.124.036802>
- [78] Wang, G., Dvir, T., Van Loo, N., Mazur, G. P., Gazibegovic, S., Badawy, G., Bakkers, E. P., Kouwenhoven, L. P., & De Lange, G. (2022). Nonlocal measurement of quasi-particle charge and energy relaxation in proximitized semiconductor nanowires using quantum dots. *Physical Review B*, 106(6), 064503. <https://doi.org/10.1103/PhysRevB.106.064503>
- [79] Van der Wiel, W. G., De Franceschi, S., Elzerman, J. M., Fujisawa, T., Tarucha, S., & Kouwenhoven, L. P. (2002). Electron transport through double quantum dots. *Reviews of modern physics*, 75(1), 1. <https://doi.org/10.1103/RevModPhys.75.1>
- [80] Danon, J., & Nazarov, Y. V. (2009). Pauli spin blockade in the presence of strong spin-orbit coupling. *Physical Review B*, 80(4), 041301. <https://doi.org/10.1103/PhysRevB.81.201305>
- [81] Nadj-Perge, S., Frolov, S., Van Tilburg, J., Danon, J., Nazarov, Y. V., Algra, R., Bakkers, E., & Kouwenhoven, L. (2010). Disentangling the effects of spin-orbit and hyperfine interactions on spin blockade. *Physical Review B*, 81(20), 201305. <https://doi.org/10.1103/PhysRevB.80.041301>
- [82] Dvir, T., Wang, G., van Loo, N., Liu, C.-X., Mazur, G. P., Bordin, A., Ten Haaf, S. L., Wang, J.-Y., van Driel, D., Zatelli, F., et al. (2023). Realization of a minimal Kitaev chain in coupled quantum dots. *Nature*, 614(7948), 445–450. <https://doi.org/10.1038/s41586-022-05585-1>
- [83] van Driel, D., Wang, G., Bordin, A., van Loo, N., Zatelli, F., Mazur, G. P., Xu, D., Gazibegovic, S., Badawy, G., Bakkers, E. P., et al. (2023). Spin-filtered measurements of Andreev bound states in semiconductor-superconductor nanowire devices. *Nature Communications*, 14(1), 6880. <https://doi.org/10.1038/s41467-023-42026-7>
- [84] Yokoyama, T., Eto, M., & Nazarov, Y. V. (2014). Anomalous Josephson effect induced by spin-orbit interaction and Zeeman effect in semiconductor nanowires. *Physical Review B*, 89(19), 195407. <https://doi.org/10.1103/PhysRevB.89.195407>
- [85] Van Heck, B., Väyrynen, J., & Glazman, L. (2017). Zeeman and spin-orbit effects in the Andreev spectra of nanowire junctions. *Physical Review B*, 96(7), 075404. <https://doi.org/10.1103/PhysRevB.96.075404>
- [86] Tosi, L., Metzger, C., Goffman, M., Urbina, C., Pothier, H., Park, S., Yeyati, A. L., Nygård, J., & Krogstrup, P. (2019). Spin-orbit splitting of Andreev states revealed by microwave spectroscopy. *Physical Review X*, 9(1), 011010. <https://doi.org/10.1103/PhysRevX.9.011010>
- [87] Samuelsson, P., Sukhorukov, E., & Büttiker, M. (2003). Orbital entanglement and violation of Bell inequalities in mesoscopic conductors. *Physical review letters*, 91(15), 157002. <https://doi.org/10.1103/PhysRevLett.91.157002>
- [88] Busz, P., Tomaszewski, D., & Martinek, J. (2017). Spin correlation and entanglement detection in Cooper pair splitters by current measurements using magnetic detectors. *Physical Review B*, 96(6), 064520. <https://doi.org/10.1103/PhysRevB.96.064520>

- [89] Brange, F, Malkoc, O., & Samuelsson, P. (2017). Minimal entanglement witness from electrical current correlations. *Physical Review Letters*, 118(3), 036804. <https://doi.org/10.1103/PhysRevLett.118.036804>
- [90] Spethmann, M., Bosco, S., Hofmann, A., Klinovaja, J., & Loss, D. (2024). High-fidelity two-qubit gates of hybrid superconducting-semiconducting singlet-triplet qubits. *Physical Review B*, 109(8), 085303. <https://doi.org/10.1103/PhysRevB.109.085303>
- [91] Liu, C.-X., Pan, H., Setiawan, F., Wimmer, M., & Sau, J. D. (2023). Fusion protocol for Majorana modes in coupled quantum dots. *Physical Review B*, 108(8), 085437. <https://doi.org/10.1103/PhysRevB.108.085437>
- [92] Tsintzis, A., Souto, R. S., Flensberg, K., Danon, J., & Leijnse, M. (2024). Majorana Qubits and Non-Abelian Physics in Quantum Dot–Based Minimal Kitaev Chains. *PRX Quantum*, 5(1), 010323. <https://doi.org/10.1103/PRXQuantum.5.010323>
- [93] Liu, Z.-H., Zeng, C., & Xu, H. (2024). Coupling of quantum-dot states via elastic-cotunneling and crossed Andreev reflection in a minimal Kitaev chain. *arXiv preprint arXiv:2403.08636*. <https://doi.org/10.48550/arXiv.2403.08636>
- [94] Jung, M., Schroer, M., Petersson, K., & Petta, J. R. (2012). Radio frequency charge sensing in InAs nanowire double quantum dots. *Applied Physics Letters*, 100(25). <https://doi.org/10.1063/1.4729469>
- [95] Meng, T., Florens, S., & Simon, P. (2009). Self-consistent description of Andreev bound states in Josephson quantum dot devices. *Physical Review B*, 79(22), 224521. <https://doi.org/10.1103/PhysRevB.79.224521>
- [96] Grove-Rasmussen, K., Jørgensen, H. I., Andersen, B. M., Paaske, J., Jespersen, T. S., Nygård, J., Flensberg, K., & Lindelof, P. E. (2009). Superconductivity-enhanced bias spectroscopy in carbon nanotube quantum dots. *Physical Review B*, 79(13), 134518. <https://doi.org/10.1103/PhysRevB.79.134518>
- [97] Deacon, R., Tanaka, Y., Oiwa, A., Sakano, R., Yoshida, K., Shibata, K., Hirakawa, K., & Tarucha, S. (2010). Tunneling spectroscopy of Andreev energy levels in a quantum dot coupled to a superconductor. *Physical review letters*, 104(7), 076805. <https://doi.org/10.1103/PhysRevLett.104.076805>
- [98] Lee, E. J., Jiang, X., Houzet, M., Aguado, R., Lieber, C. M., & De Franceschi, S. (2014). Spin-resolved Andreev levels and parity crossings in hybrid superconductor–semiconductor nanostructures. *Nature nanotechnology*, 9(1), 79–84. <https://doi.org/10.1038/nnano.2013.267>
- [99] Jellinggaard, A., Grove-Rasmussen, K., Madsen, M. H., & Nygård, J. (2016). Tuning Yu-Shiba-Rusinov states in a quantum dot. *Physical Review B*, 94(6), 064520. <https://doi.org/10.1103/PhysRevB.94.064520>
- [100] Ahmed, I., & Gonzalez-Zalba, M. F. (2020). Radio-frequency capacitive gate-based charge sensing for semiconductor quantum dots. *Micro and Nano Machined Electrometers*, 83–128. [https://doi.org/10.1007/978-981-13-3247-0\\_3](https://doi.org/10.1007/978-981-13-3247-0_3)
- [101] de Jong, D. (2021). Gate-based readout of hybrid quantum dot systems. <https://doi.org/10.4233/uuid:9cd36947-5e27-4436-9bbb-d7fc5daa6047>
- [102] Büttiker, M., Thomas, H., & Prêtre, A. (1993). Mesoscopic capacitors. *Physics Letters A*, 180(4-5), 364–369. [https://doi.org/10.1016/0375-9601\(93\)91193-9](https://doi.org/10.1016/0375-9601(93)91193-9)

- [103] Persson, F, Wilson, C., Sandberg, M., Johansson, G., & Delsing, P. (2010). Excess dissipation in a single-electron box: The Sisyphus resistance. *Nano letters*, *10*(3), 953–957. <https://doi.org/10.1021/nl903887x>
- [104] Aumentado, J., Keller, M. W., Martinis, J. M., & Devoret, M. H. (2004). Nonequilibrium quasiparticles and  $2e$  periodicity in single-cooper-pair transistors. *Physical review letters*, *92*(6), 066802. <https://doi.org/10.1103/PhysRevLett.92.066802>
- [105] Ristè, D., Bultink, C., Tiggelman, M. J., Schouten, R. N., Lehnert, K. W., & DiCarlo, L. (2013). Millisecond charge-parity fluctuations and induced decoherence in a superconducting transmon qubit. *Nature communications*, *4*(1), 1913. <https://doi.org/10.1038/ncomms2936>
- [106] Olivares, D., Yeyati, A. L., Bretheau, L., Girit, Ç., Pothier, H., & Urbina, C. (2014). Dynamics of quasiparticle trapping in Andreev levels. *Physical Review B*, *89*(10), 104504. <https://doi.org/10.1103/PhysRevB.89.104504>
- [107] Wesdorp, J., Gruenhaupt, L., Vaartjes, A., Pita-Vidal, M., Bargerbos, A., Splitthoff, L. J., Krogstrup, P., van Heck, B., & De Lange, G. (2023). Dynamical polarization of the fermion parity in a nanowire Josephson junction. *Physical review letters*, *131*(11), 117001. <https://doi.org/10.1103/PhysRevLett.131.117001>
- [108] Van Woerkom, D. J., Proutski, A., Van Heck, B., Bouman, D., Väyrynen, J. I., Glazman, L. I., Krogstrup, P., Nygård, J., Kouwenhoven, L. P., & Geresdi, A. (2017). Microwave spectroscopy of spinful Andreev bound states in ballistic semiconductor Josephson junctions. *Nature Physics*, *13*(9), 876–881. <https://doi.org/10.1038/nphys4150>
- [109] Hays, M., De Lange, G., Serniak, K., Van Woerkom, D., Bouman, D., Krogstrup, P., Nygård, J., Geresdi, A., & Devoret, M. (2018). Direct microwave measurement of andreev-bound-state dynamics in a semiconductor-nanowire josephson junction. *Physical review letters*, *121*(4), 047001. <https://doi.org/10.1103/PhysRevLett.121.047001>
- [110] Aassime, A., Johansson, G., Wendin, G., Schoelkopf, R., & Delsing, P. (2001). Radio-frequency single-electron transistor as readout device for qubits: Charge sensitivity and backaction. *Physical Review Letters*, *86*(15), 3376. <https://doi.org/10.1103/PhysRevLett.86.3376>
- [111] Barthel, C., Kjærgaard, M., Medford, J., Stopa, M., Marcus, C. M., Hanson, M., & Gossard, A. C. (2010). Fast sensing of double-dot charge arrangement and spin state with a radio-frequency sensor quantum dot. *Physical Review B*, *81*(16), 161308. <https://doi.org/10.1103/PhysRevB.81.161308>
- [112] Petersson, K., Smith, C., Anderson, D., Atkinson, P., Jones, G., & Ritchie, D. (2010). Charge and spin state readout of a double quantum dot coupled to a resonator. *Nano letters*, *10*(8), 2789–2793. <https://doi.org/10.1021/nl100663w>
- [113] Van Driel, D., Roovers, B., Zatelli, F., Bordin, A., Wang, G., Van Loo, N., Wolff, J. C., Mazur, G. P., Gazibegovic, S., Badawy, G., et al. (2024). Charge sensing the parity of an andreev molecule. *PRX Quantum*, *5*(2), 020301. <https://doi.org/10.1103/PRXQuantum.5.020301>
- [114] Barends, R., Wenner, J., Lenander, M., Chen, Y., Bialczak, R. C., Kelly, J., Lucero, E., OMalley, P., Mariantoni, M., Sank, D., et al. (2011). Minimizing quasiparticle gen-

- eration from stray infrared light in superconducting quantum circuits. *Applied Physics Letters*, 99(11). <https://doi.org/10.1063/1.3638063>
- [115] Diamond, S., Fatemi, V., Hays, M., Nho, H., Kurilovich, P. D., Connolly, T., Joshi, V. R., Serniak, K., Frunzio, L., Glazman, L. I., et al. (2022). Distinguishing parity-switching mechanisms in a superconducting qubit. *PRX Quantum*, 3(4), 040304. <https://doi.org/10.1103/PRXQuantum.3.040304>
- [116] Aghaee, M., Ramirez, A. A., Alam, Z., Ali, R., Andrzejczuk, M., Antipov, A., Astafev, M., Barzegar, A., Bauer, B., Becker, J., et al. (2024). Interferometric single-shot parity measurement in an InAs-Al hybrid device. *arXiv preprint arXiv:2401.09549*. <https://doi.org/10.48550/arXiv.2401.09549>
- [117] Krogstrup, P., Ziino, N., Chang, W., Albrecht, S., Madsen, M., Johnson, E., Nygård, J., Marcus, C. M., & Jespersen, T. (2015). Epitaxy of semiconductor-superconductor nanowires. *Nature materials*, 14(4), 400–406. <https://doi.org/10.1038/nmat4176>
- [118] Zehnder, A., Lerch, P., Zhao, S., Nussbaumer, T., Kirk, E., & Ott, H. (1999). Proximity effects in Nb/Al-AlO<sub>x</sub>-Al/Nb superconducting tunneling junctions. *Physical Review B*, 59(13), 8875. <https://doi.org/10.1103/PhysRevB.59.8875>
- [119] Blonder, G., Tinkham, M., & Klapwijk, T. (1982). Transition from metallic to tunneling regimes in superconducting microconstrictions: Excess current, charge imbalance, and supercurrent conversion. *Physical Review B*, 25(7), 4515. <https://doi.org/10.1103/PhysRevB.25.4515>
- [120] Kjærgaard, M., Suominen, H. J., Nowak, M., Akhmerov, A., Shabani, J., Palmstrøm, C., Nichele, F., & Marcus, C. M. (2017). Transparent semiconductor-superconductor interface and induced gap in an epitaxial heterostructure Josephson junction. *Physical Review Applied*, 7(3), 034029. <https://doi.org/10.1103/PhysRevApplied.7.034029>
- [121] Heedt, S., Quintero-Pérez, M., Borsoi, F., Fursina, A., van Loo, N., Mazur, G. P., Nowak, M. P., Ammerlaan, M., Li, K., Korneychuk, S., et al. (2021). Shadow-wall lithography of ballistic superconductor-semiconductor quantum devices. *Nature Communications*, 12(1), 4914. <https://doi.org/10.1038/s41467-021-25100-w>
- [122] Kjærgaard, M., Nichele, F., Suominen, H., Nowak, M., Wimmer, M., Akhmerov, A., Folk, J., Flensberg, K., Shabani, J., Palmstrøm, W. C., et al. (2016). Quantized conductance doubling and hard gap in a two-dimensional semiconductor-superconductor heterostructure. *Nature communications*, 7(1), 12841. <https://doi.org/10.1038/ncomms12841>
- [123] Shabani, J., Kjærgaard, M., Suominen, H. J., Kim, Y., Nichele, F., Pakrouski, K., Stankevic, T., Lutchyn, R. M., Krogstrup, P., Feidenhans'l, R., et al. (2016). Two-dimensional epitaxial superconductor-semiconductor heterostructures: A platform for topological superconducting networks. *Physical Review B*, 93(15), 155402. <https://doi.org/10.1103/PhysRevB.93.155402>
- [124] Mittag, C., Karalic, M., Mueller, S., Tschirky, T., Wegscheider, W., Nazarenko, O., Kovalenko, M. V., Ihn, T., & Ensslin, K. (2017). Passivation of edge states in etched InAs sidewalls. *Applied Physics Letters*, 111(8). <https://doi.org/10.1063/1.4986614>

- [125] Mueller, S., Mittag, C., Tschirky, T., Charpentier, C., Wegscheider, W., Ensslin, K., & Ihn, T. (2017). Edge transport in InAs and InAs/GaSb quantum wells. *Physical Review B*, 96(7), 075406. <https://doi.org/10.1103/PhysRevB.96.075406>



# ACKNOWLEDGMENTS

A PhD journey can often be challenging, and I was lucky to have friends and colleagues to help me along the way and make the experience more enjoyable. **Srijit**, thank you for creating a friendly group atmosphere, being on top of the experiments running, and always questioning the results and explanations. To all current and former members of the 2D Topo group – **Fokko, Ting, Michael, Christian, Prasanna, Qing, Saurabh, Nikos, Bas, Yining, Sebas, Rebecca, DJ, Wietze** – it was a pleasure to work with you, have fun discussions (including, but not limited to, the scientific ones), and darts competitions. Big thanks to the QuTech staff, including those providing administrative support – **Jenny, Csilla**, and those helping with engineering aspects – **Jason, Olaf, Raymond, Erik**. It would have been impossible to make the devices without the people of **Kavli Nanolab Delft**. Your hard work is keeping the machines running despite all the abuse from us, the users.

I'm glad that during my master's and PhD years, I had my friends to spend time with. And even though we can't spend as much time together now, I'm glad we keep in contact with each other. **Boris**, it was always fun to discuss politics with you while in the gym. **Hélène**, thanks for the coffee breaks and all the movie evenings. **Christian**, I will always cherish our late-night adventures around Delft. **Marta**, you were a great neighbor during the tough corona times. **Hugo**, thanks for your positive vibes. **Kostas**, thanks for the long conversations on many technology-related (and not) topics. **Айрат, Альбина**, хотя природы здесь маловато, походы на Амеланд (и не только) были замечательные.

**Мама**, спасибо за все усилия и поддержку. **Алина**, ты всегда рядом и больше всех поддерживаешь моё душевное и физическое состояние. Я уверен, что без тебя я не только не смог бы закончить этот диплом, но и не приехал бы в Делфт и не испытал бы всего, о чём здесь написано.







# LIST OF PUBLICATIONS

7. *Gate sensing of a two-site Kitaev chain*  
Yining Zhang, **Ivan Kulesh**, Sebastiaan L. D. ten Haaf, Tijn Degroote, Christian G. Prosko, Di Xiao, Candice Thomas, Michael J. Manfra and Srijit Goswami  
In preparation.
6. *A flux-controlled two-site Kitaev chain*  
**Ivan Kulesh**, Sebastiaan L. D. ten Haaf, Qingzhen Wang, Vincent P. M. Sietses, Yining Zhang, Sebastiaan R. Roelofs, Christian G. Prosko, Di Xiao, Candice Thomas, Michael J. Manfra and Srijit Goswami  
In review, [arXiv.2501.15912](https://arxiv.org/abs/2501.15912).
5. *Flux-tunable Josephson effect in a four-terminal junction*  
Christian G. Prosko, Wietze D. Huisman, **Ivan Kulesh**, Di Xiao, Candice Thomas, Michael J. Manfra, and Srijit Goswami  
[Physical Review B \*\*110\*\*, 064518 \(2024\)](https://doi.org/10.1103/PhysRevB.110.064518).
4. *Flux-tunable hybridization in a double quantum dot interferometer*  
Christian G. Prosko, **Ivan Kulesh**, Michael Chan, Lin Han, Di Xiao, Candice Thomas, Michael Manfra, Srijit Goswami, and Filip K. Malinowski  
[SciPost Physics \*\*17\*\*, 074 \(2024\)](https://doi.org/10.1103/SciPostPhysics.17.074).
3. *A two-site Kitaev chain in a two-dimensional electron gas*  
Sebastiaan L.D. ten Haaf, Qingzhen Wang, A. Mert Bozkurt, Chun-Xiao Liu, **Ivan Kulesh**, Philip Kim, Di Xiao, Candice Thomas, Michael J. Manfra, Tom Dvir, Michael Wimmer and Srijit Goswami  
[Nature \*\*630\*\*, 8016 \(2024\)](https://doi.org/10.1038/s41586-024-04016-1).
2. *Triplet correlations in Cooper pair splitters realized in a two-dimensional electron gas.*  
Qingzhen Wang, Sebastiaan LD Ten Haaf, **Ivan Kulesh**, Di Xiao, Candice Thomas, Michael J. Manfra, and Srijit Goswami  
[Nature Communications \*\*14\*\*, 4876 \(2023\)](https://doi.org/10.1038/s41586-023-04876-1).
1. *Quantum Dots in an InSb Two-Dimensional Electron Gas*  
**Ivan Kulesh**, Chung Ting Ke, Candice Thomas, Saurabh Karwal, Christian M. Moehle, Sara Metti, Ray Kallaher, Geoffrey C. Gardner, Michael J. Manfra, and Srijit Goswami  
[Physical Review Applied \*\*13\*\*, 041003 \(2020\)](https://doi.org/10.1103/PhysRevApplied.13.041003).

